Aalto University
School of Engineering

Riikka Häsä

Numerical simulations on ice-structure interaction in shallow water

School of Engineering

Thesis submitted for examination for the degree of Master of Science in Technology.

Espoo September 10, 2015

Thesis supervisor and advisor:

Assistant Prof. Arttu Polojärvi

AALTO UNIVERSITY
SCHOOL OF ENGINEERING

ABSTRACT OF THE
MASTER'S THESIS

Author: Riikka Häsä

Title: Numerical simulations on ice-structure interaction in shallow water

Date: September 10, 2015 Language: English Number of pages: 5+77

Department of Applied Mechanics

Professorship: Technical mechanics Code: Kul-49

Supervisor and instructor: Assistant Prof. Arttu Polojärvi

Moving sea ice causes high loads on Arctic offshore structures when it breaks against them. Many of these structures are built in relatively shallow water, which affects the loading process. The ice breaking process in shallow water involves complex interactions between the intact ice sheet, the ice blocks formed in the process, the structure and the seabed.

In this thesis, ice-structure interaction on a wide sloping structure in shallow water is studied using a 2D combined finite-discrete element method (FEM-DEM). The intact ice is modelled as a nonlinear Timoshenko beam and its fracture into smaller pieces is modelled using the cohesive crack model. The discrete element method is used for contact force calculation between the ice blocks, the structure and the seabed. In the work reported here, the inclination angle of the structure, the ice thickness and the water depth are varied to study how these parameters affect the ice rubble grounding and the ice loading process.

The simulation results suggest that grounded rubble leads to higher loads on the structure than non-grounded rubble. The loads on the structure increase with thicker ice and decreasing water depth. In addition, a larger inclination angle induces higher loads on the structure throughout the simulation. The load events on the structure are related to simultaneous ride-up events of the rubble and the loads are transmitted to the structure along so-called force chains. Furthermore, the probability of overtopping increases in shallow water.

The load increase and the increased probability of overtopping in shallow water are caused by the supporting effect of the seabed. Sudden load drops on the structure are related to buckling of the force chains. When the rubble is grounded, the force chains are supported from below by the seabed and form above by the rubble above. Thus they sustain more loads than force chains in non-grounded rubble.

Keywords: Ice mechanics, ice-structure interaction, ice loads, grounding, Arctic offshore structures, shallow water, numerical modelling, combined finite-discrete element method, FEM-DEM

AALTO-YLIOPISTO
INSINÖÖRITIETEIDEN KORKEAKOULU

DIPLOMITYÖN
TIIVISTELMÄ

Tekijä: Riikka Häsä

Työn nimi: Jää-rakenne-vuorovaikutuksen numeerinen mallinnus matalassa vedessä

Päivämäärä: September 10, 2015 Kieli: Englanti Sivumäärä: 5+77

Sovelletun mekaniikan laitos

Professuuri: Teknillinen mekaniikka Koodi: Kul-49

Valvoja ja ohjaaja: Apulaisprof. Arttu Polojärvi

Liikkuva jää aiheuttaa suuria kuormia arktisille merirakenteille jään murtuessa rakennetta vasten. Monet näistä rakenteista ovat rakennettu matalaan veteen, mikä vaikuttaa kuormitusprosessiin. Murtumisprosessi matalassa vedessä sisältää monimutkaisia vuorovaikutuksia jäälautan, prosessissa syntyneiden jäälohkareiden, rakenteen sekä merenpohjan välillä.

Tässä työssä tutkitaan jää-rakenne-vuorovaikutusta leveää kaltevaseinäistä matalan veden rakennetta vasten käyttäen kaksiulotteista yhdistettyä diskreetti- ja elementtimenetelmää (FEM-DEM). Menetelmässä ehjä jäälautta mallinnetaan epälineaarisena Timoshenko-palkkina ja sen murtuminen pienempiin osiin mallinnetaan koheesiomurtumamallia käyttäen. Kontaktivoimat jäälohkareiden, rakenteen ja merenpohjan välillä lasketaan diskreettielementtimenetelmällä. Tämän työn simulaatioissa varioidaan rakenteen kallistuskulmaa, jään paksuutta ja veden syvyyttä, jotta niiden vaikutusta jäävallin pohjautumiseen ja jään kuormitusprosessiin voitaisiin tutkia.

Simulaatioiden tulokset osoittavat, että jäävallin pohjautuminen aiheuttaa suurempia kuormia rakenteella kuin kelluva jäävalli. Kuorma rakenteella kasvaa jään paksutessa ja veden syvyyden kasvaessa. Sen lisäksi suurempi rakenteen kallistuskulma johtaa suurempiin kuormiin rakenteella koko simulaation ajan. Kuormitustapahtumat rakenteella liittyvät jään ylösajotilanteisiin ja voima rakenteelle välittyy niin sanottua voimaketjua pitkin. Myös jään ajautuminen rakenteen päälle on todennäköisempää matalassa vedessä.

Kuormien sekä jää yliajautumisen todennäköisyyden kasvaminen matalassa vedessä johtuu merenpohjan tuesta. Äkilliset kuormanpudotukset rakenteella johtuvat voimaketjun nurjahtamisesta. Kun jäävalli on pohjautunut, merenpohja tukee voimaketjua alapuolelta ja jäävalli voimaketjun päällä tukee sitä yläpuolelta.

Avainsanat: Jäämekaniikka, jää-rakenne-vuorovaikutus, jääkuormat, jään pohjautuminen, arktiset merirakenteet, matala vesi, numeerinen mallinnus, yhdistetty diskreetti- ja elementtimenetelmä

Preface

I would like to express my deepest gratitude to my supervisor, Assistant Professor Arttu Polojärvi, who has guided me through this project. His comments and ideas regarding this work have been invaluable. I would also like to express my appreciation to Professor Jukka Tuhkuri for his mentoring and for giving me the opportunity to work with his group. Furthermore, the financial support from the Department of Applied Mechanics at Aalto University is gratefully acknowledged.

I wish to thank the whole ice mechanics research group. It has been a pleasure working with you. My officemate, Professor John Dempsey, deserves a special thank you for the information passed on during the countless discussions regarding scientific work and life in general. I would also like to thank my friend Heikki Kahila for the countless coffee breaks at work. The discussions over a cup of coffee provided a welcomed break and helped me rearrange my ideas.

Finally, I would like to extend my gratitude to my family and friends who have supported and encouraged me in my endeavours during these years. My appreciation towards you is beyond words.

Espoo, September 10, 2015

Riikka Häsä

Contents

1 Introduction

Understanding ice mechanics and defining ice loads is essential when designing structures for seas where freezing and permanent sea ice occur. Typical structures built in such areas, including lighthouses, bridges and oil platforms, are subject to ice loads when the ice interacts with the structures, as seen in Figure 1. Moreover, in recent years, the demand for opening new Arctic shipping routes and building new ports and wind farms in the Arctic areas has further emphasised the importance of understanding ice mechanics. Designing an Arctic offshore structure is a challenging task which requires understanding the complex phenomena involved in the interactions between the ice and the structure. In this work, numerical simulations are performed to gain understanding on the ice-structure interaction process in shallow water.

1.1 Background

Ice mechanics is a fairly new branch of science. According to Sanderson (1988), the systematic international research on ice-structure interaction began in the 1960s when natural resources lying in the seabed of Arctic areas aroused great economic interest. As a consequence, funding was provided to study ice and its properties in order to access the oil and gas reserves in the crust of the earth beneath the frozen sea (Sanderson, 1988). Since then, numerous attempts have been made to model ice and

Figure 1: Arctic offshore structures are subject to ice loads when the ice interacts with the structure. A large ice rubble pile has formed in front of Kemi I lighthouse as the advancing ice has failed against the it. The image shows the sail of the pile while the rest of the rubble is under water. (Image by the courtesy of Mauri Määttänen.)

understand its mechanical behaviour. This task has, however, proven challenging due to the complexity of the material. Sea ice is an inhomogeneous material that can undergo both ductile and brittle failure depending on the sample size and the details of the loading process. Furthermore, the mechanical properties depend on various factors, such as the temperature, strain rate, salinity and grain size and orientation (Kolari *et al.*, 2009). In addition, different phenomena can be examined depending on the scale of observation that ranges from geophysical to engineering and microstructural scales (Dempsey, 2000). In this work, ice mechanics is studied on the engineering scale.

When moving ice pushes against an Arctic offshore structure due to prevailing wind conditions and ocean currents (Weeks, 2010), the ice breaks into smaller pieces called ice rubble. The rubble may pile up in front of the structure, as seen in Figure 1 showing the sail of the rubble pile while the most of the rubble is under water. This ice breaking process, called rubbling, exerts high loads on the structure. Therefore, the structures have to be designed so that they promote ice failure and are strong enough to withstand the loads required to break the ice.

High ice loads may move Arctic offshore structures from their foundation, destroy the structure walls or cause local damage. Therefore, the ice load is a governing factor when designing offshore structures in Arctic areas. The ice loads largely depend on the failure mode of the ice, which is often at least partly defined by the geometry of the structure wall. The prevailing failure mode against a vertical wall is crushing, which exposes the structure to significant ice loads (Palmer and Croasdale, 2012), whereas failure against a sloping wall alters the fragmentation process so that the ice breaks by bending. Bending failure requires less force than crushing and thus the Arctic offshore structures often have inclined walls.

Some of the Arctic offshore structures are built in relatively shallow water or on an artificially elevated seabed called a berm. In shallow water, the rubble pile forming in the ice loading process may grow so large that it starts interacting with

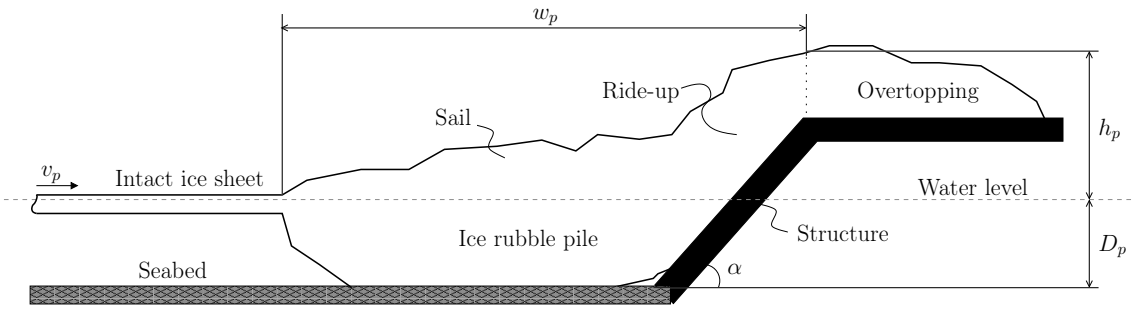

Figure 2: The ice is pushed against a wide sloping structure from the left at a velocity v_p. Some grounded rubble has formed in front of the structure and ice has been pushed on top of the structure as a result of overtopping. The structure has an inclination angle α and the rubble geometry is given as follows: w_p is the rubble pile width, h_p is the pile height measured from the water level and D_p is the pile depth measured from the water level.

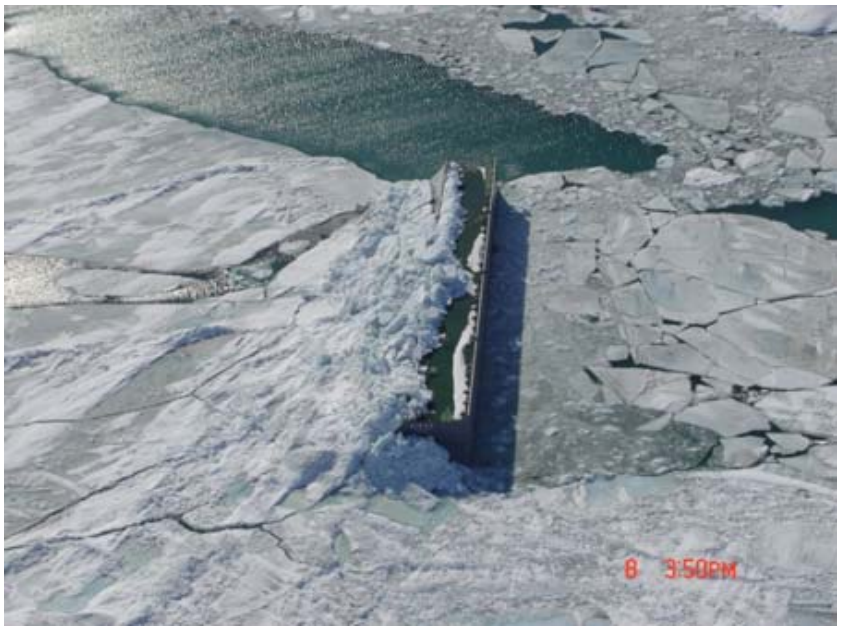

Figure 3: Ice barriers are wide structures that are often built in shallow water to protect offshore structures and ports from moving ice. The ice is pushed against the structure from the left and a large amount of rubble has formed in front of the structure. Furthermore, there has been overtopping as some ice has ridden on top of the ice barrier (Croasdale *et al.*, 2011).

the seabed. This interaction between the rubble and seabed is called grounding and, if it occurs, it affects the loading process. A schematic view of an ice loading process in shallow water is illustrated in Figure 2. The ice moves towards the wide inclined structure from the left at a velocity v_p and the rubble formed in the process is grounded. Some of the ice has been pushed on top of the structure as a result of the rubble riding up the structure wall. This type of process is further illustrated in Figure 3 which shows an ice barrier in shallow water subject to ice rubbling against it in the Caspian Sea. Ice barriers are wide structures with inclined walls and their purpose is to protect, for example, ports and oil platforms from moving sea ice. In Figure 3, the ice has pushed against the structure from the left and a large rubble pile has formed in front of it.

From an engineering point of view, estimating the maximum ice loads and understanding their causes are the most interesting aspects of designing an Arctic offshore structure. The depth of the water in front of the structure may be an important factor affecting the ice loads and the so-called overtopping which occurs when moving ice rides up the structure and accumulates on top of it or sometimes even moves over it.

According to current knowledge, grounded rubble decreases the load on the structure as a part of the load is transmitted to the seabed (Sudom and Timco, 2009; Timco and Wright, 1999; Croasdale, 2012). This, together with lower construction

costs, has encouraged engineers to build Arctic offshore structures in shallow waters or on elevated berms. Furthermore, some researchers believe grounded rubble may form a buffer that protects the structure from overtopping (Timco and Wright, 1999), while others believe overtopping is more likely to occur in shallow water (Palmer and Croasdale, 2012). Intense overtopping is unfavourable because it causes extra loading on the structure and poses a safety threat when the encroaching rubble on top of the structure may damage the operational devices. Moreover, ice riding over a protective ice barrier may impede navigation to the ports and offshore platforms, and damage the structures the ice barrier is protecting.

Although many Arctic offshore structures are built in shallow water, the effect of rubble grounding has not been widely studied. Previous research on rubble grounding has been carried out, for example, by Marshall *et al.* (1989), Timco and Wright (1999), Sudom and Timco (2009), Karulin *et al.* (2007), and Goldstein *et al.* (2013). Understanding the complex interactions related to grounding is valuable in itself, but it can also be directly applied to design offshore structures. Studying ice-structure interaction in shallow water is expected to shed some light on the partly controversial prevailing notions and provide factual data to support engineers in their design work.

There are several factors affecting ice loads on offshore structures that still remain unknown as the interactions involved in the process are very complex. The intact ice sheet first breaks into individual ice blocks which then interact with each other, with the structure and with the seabed. The process details affect the further process and thus it is necessary to study the formation of the ice blocks and follow their trajectories. For this purpose, numerical models, especially discrete element method (DEM) based techniques are very suitable, as they treat the rubble as an assembly of discrete blocks and allow the process to be scrutinised in detail.

1.2 Objectives and Scope

The main objective of this study is to examine how rubble grounding in shallow water affects the magnitude of the ice loads and their distribution between the seabed and the structure wall. This study focuses on numerical modelling of ice rubbling process against an inclined structure in shallow water (see Figure 2). The ice-structure-seabed interaction is studied using a two-dimensional combined finite-discrete element method (FEM-DEM). The interaction process is examined with two ice thicknesses and wall inclination angles as a function of the water depth. The goal is to acquire information on how the seabed affects the rubbling process compared with rubbling against structures in deep water.

Another objective is to study how the load is transmitted to the structure in the rubble during peak load events and what phenomena cause these peak loads. The load transmission is studied by investigating the average velocities in the rubble during load events and by studying the so-called force chains which illustrate the load transmission between individual ice blocks.

Finally, the effect of grounding on overtopping and other rubble features, such as the pile geometry, are studied. The aim is to make observations on the water

depths at which grounding occurs, as well as study how the simulation variables affect these phenomena.

This study is confined to a fixed wide structure with upward sloping walls in shallow water. For this purpose, the 2D model is sufficient because it is able to capture all the relevant phenomena related to wide structures. The rubble behaves differently in interaction with wide and narrow structures and thus, for instance, the so-called clearing is not modelled. Clearing occurs when the rubble moves downstream from a narrow structure by pushing around the sides of the structure. This study concentrates on structures with sloping walls because they are the most common offshore structures found in Arctic areas.

1.3 Thesis structure

This thesis first introduces different approaches used in ice mechanics research. These approaches include field measurements, model scale experiments and mathematical modelling. After this, the combined finite-element method is described and an overview of the simulations and the simulation parameters in this work are given. Then, the results of the simulations are presented, followed by a discussion on the observations and their significance. Finally, the thesis concludes with a summary of the thesis and the main results, and with suggestions for future work.

2 Previous Research on Ice-Structure Interaction

This chapter introduces previous research on ice-structure interaction. For this purpose, the research methods have been divided into three different approaches which include field measurements, model scale testing and mathematical modelling. The techniques are often combined in ice mechanics research to analyse the phenomena occurring during the interaction process in detail. Field data and model scale tests are often used to validate mathematical models, whereas mathematical models are often used for predictions and for design purposes, or like here, to gain comprehensive understanding of the physical phenomena behind ice loads. This chapter describes the typical characteristic of each approach and focuses on their application to study ice rubble and to evaluate forces on wide structures in shallow water.

2.1 Field observations

The first data collected in the field experiments was qualitative and it was based on visual observations. Sustained efforts to collect full-scale data on ice-structure interaction have been made since the 1960s when the petroleum companies started investing in ice research, and the first structures that were instrumented for ice load measurements were narrow constructions such as bridge piers and lighthouses (Sanderson, 1988). The amount of the available data has, however, remained limited since the instrumentation of offshore structures and the data collection have proven difficult and costly. Further, the data from many experimental campaigns has been classified confidential because the measurement programmes are often carried out by industrial operators. Nonetheless, a reasonable amount of full-scale data has been acquired, most notably in the 1980s. The data of the best-documented reference cases is collected from offshore platforms and so-called drilling caissons in the Canadian Beaufort Sea. Caissons are sand-filled artificial islands that have a concrete or steel outer ring that supports the structure and protects the sand from erosion (see Figure 4). A comprehensive overview of the data collection methods and the most important experimental campaigns is given by Sanderson (1988), Palmer and Croasdale (2012), and Timco and Weeks (2010). The description here is mainly based on these sources.

The techniques used for measuring ice loads on structures can be divided into four conceptual categories. These approaches include measuring the structural response, estimating the forces from ice deceleration, in situ measurements of the surrounding ice, and the direct measurement technique where the interface between the structure and the ice is equipped with load cells and panels. Furthermore, photography and video recordings are important techniques that provide qualitative data to support the quantitative measurements.

The structural response is monitored using strain gauges, extensometers, accelerometers or tiltmeters. A typical instrumentation set-up using strain gauges and extensometers to study the structural response of a drilling caisson is illustrated in Figure 5. Furthtermore, the foundation response can be monitored using piezometers, inclinometers, pressure cells or tiltmeters. Measuring the foundation

Figure 4: The Molikpaq is an octagonal mobile caisson that was used for oil exploration in the Canadian Beaufort Sea. The data collected from it has been widely used in ice mechanics research (Sudom and Timco, 2009).

response is, however, subject to error because the structures are founded in soil with often unknown material properties and internal damping that hinders the load transfer.

The strain gauges provide a well-established and inexpensive method for estimating the forces exerted on the structure. They measure the strains directly on the structural members, which makes them a reliable measurement technique. Strain gauging requires calibration between strain and stress, which is performed analytically or empirically. Analytical calibration can readily be carried out using finite element analysis but empirical calibration requires applying known static loads on the structure, which may be costly and difficult to realise. The major disadvantage of strain gauging when measuring ice loads is its susceptibility to respond to vibrations caused by structural resonance under cyclic loading. When the structure is resonating, the strain gauges give information on the true stress state in the structure. However, these stresses do not give information on the actual applied ice load which can be significantly lower than the measured load. Furthermore, proper installation of strain gauges often requires a substantial amount of labour. Similarly to strain gauging, extensometers measure the strain or deflection of a structural member. Therefore, their implementation faces similar difficulties to strain gauging.

The operating principle of accelerometers and tiltmeters is based on acceleration. Accelerometers measure the acceleration which yields the force after integration. They are applicable if the structure can be idealised as a mass-spring system. Obtaining reliable results, however, requires knowing the structural properties of the structure, including the damping and stiffness coefficients, which makes the technique cumbersome and subject to errors. Tiltmeters can be used to measure global

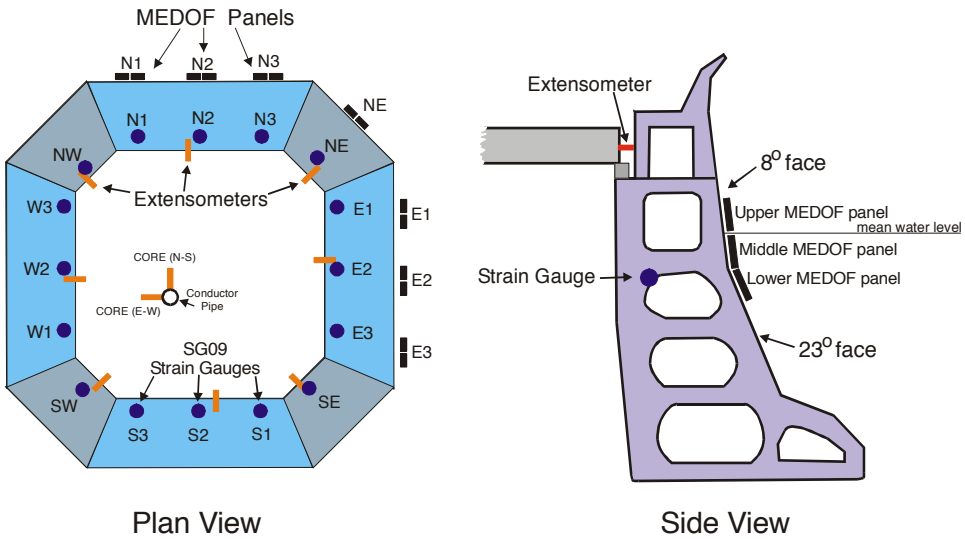

Figure 5: The Molikpaq (also in Figure 4) is instrumented with strain gauges and extensometers to study the structural response, and with so-called fluid-filled Medof load panels to measure loads at the interface of the sea and the structure (Timco and Wright, 2005).

tilt or relative tilt between two reference points. The global load can be derived from the global tilt and thus the point of application of the load should be known from other sources. Tiltmeters give the most accurate results on tall, narrow structures such as bridge piers.

Ice sheet deceleration is a fairly simple method to determine ice loads on structures. It is based on measuring the ice sheet deceleration during its interaction with a structure. The force can be obtained by multiplying the deceleration with the estimated mass of the ice sheet. The deceleration is estimated using an accelerometer attached to the ice sheet or using time-lapse photography and the mass of the ice sheet is obtained volumetrically based on the area, the thickness and the density of the ice sheet. The method was used to measure forces on the natural Hans Island in the 1980s. The method, however, does not take into account the hydrodynamic interaction between the ice sheet and the water, which has a more pronounced effect in shallow water. Furthermore, the technique treats the ice as a rigid body and omits its elastic behaviour, which may lead to overestimation of the forces.

Another technique for deriving the ice forces on the structure is instrumenting the ice surrounding the structure. The stress in the ice can be monitored using flat or cylindrical sensors or strainmeters. The flat sensors are often installed in rosette formation to measure biaxial stress-state. However, the stiffness difference between the ice and the sensor has to be taken into account. This can be avoided by using strainmeters that measure the strain of the ice between two anchored endpoints. Unlike flat and cylindrical sensors that are installed inside the ice, strainmeters can be implemented without causing disturbance to the ice sheet. When the strain in the ice is known, an estimate for the global load on the structure can be derived from

elastic analysis. Strainmeters are, however, better suited for obtaining information about the ice deformation process than estimating the ice stress. When strainmeters are used, the ice stress can only be derived from the strain under certain restrictive conditions, including loading events of long duration and negligible bending.

In the interfacial method, load panels and cells are installed in the waterline at the interface between the ice and the structure as shown in Figure 5. The interfacial method directly measures the ice load applied to the structure and it is thus immune to structural resonance. This is its major advantage compared with the other techniques. Load panels consist of two parallel steel plates with internal stiffening elements between them, and they measure forces by deforming under compression when the distance between the adjacent plates changes. The widely used Medof panel is fluid-filled and measures the applied force by fluid displacement. As the volume of the panel changes due to compression, the liquid is pushed into a vertical measuring tube that indicates the pressure applied on the panel. Other possible load panel constructions include attaching strain gauges to the steel plates of the load panel or using optical methods. When load panels are used, the point of application of the force is at least roughly known and the loads of adjacent panels can be superposed to obtain global loads. The resolution of a panel is the size of the panel, typically 1 to 2 m by 1 to 2 m.

One of the most important data collection initiatives is the Molikpaq, a mobile artificial island used for oil exploration in the Canadian Beaufort Sea (see Figure 4). The Molikpaq was first launched in 1984 and it was deployed in four locations in 11 m to 32 m deep water until it was moved to Russia in 1998 (Sudom and Timco, 2009; Palmer and Croasdale, 2012). Over its deployment period, it has provided a vast amount of information on ice loads in shallow and deep water. The Molikpaq is an octagonal steel caisson that has four 60 m long sides and four 22 m long sides so that its diameter is 90 m. The inclination angle of its walls is 82° at the water level and 67° below the mean water level. As shown in Figure 5, it is instrumented with Medof panels, strain gauges, extensometers and soil instruments. Thus the data collected from various sensors can be compared, and validated, against each other. This enhances the reliability of the load estimates measured at the Molikpaq. The caisson was deployed at each of the four deployment locations over one winter period. At the first two locations, Tarsiut P-45 and Amauligak I-65, the setdown depth was fairly deep (19.5 m) and no permanently grounded rubble formed. However, the two last deployments, Amauligak F-24 and Isserk I-15, were in shallower setdown depths (15.8 m and 13.4 m, respectively) and large grounded rubble piles developed and remained firmly grounded throughout the deployment period.

Other notable initiatives that have provided data on ice loads in shallow water include the Tarsiut N-44 Caisson Retained Island and ESSO's Caisson Retained Island (CRI) at Kaubvik, both in the Beaufort Sea. Tarsiut Island was constructed in 1981, being the first caisson-type artificial island. It had an octagonal shape with 100 m diameter and vertical walls. The island was deployed in 22 m water on a large berm that was six metres under the water surface. In the winter 1982-3, it was used to study the load transmission through grounded rubble. The caisson was instrumented with Medof load panels, strain gauges and soil instruments, and the

ice sheet surrounding the structure was instrumented with strainmeters. Visual observations were also made based on time-lapse photography. A detailed description of the observations made at Tarsiut Island is given by Timco and Wright (1999).

ESSO's Caisson Retained Island at Kaubvik was used in the winter 1986-7 to study ice rubble characteristics and load transmission as described in Marshall *et al.* (1989). The caisson island was installed on a berm in 18 m deep water. It had an octagonal shape with 112 m diameter and steeply sloping walls. Comprehensive instrumentation was carried out, including pressure sensors and geotechnical sensors on the caisson, pressure panels and thermocouple arrays in the rubble, and pressure sensor rosettes in the intact ice. However, the measurements at Kaubvik faced various technical difficulties that resulted in significant data losses. In addition to these examples, Sayed (1989) gives an overview of the typical features of grounded rubble piles observed at various locations.

2.2 Model Scale Testing

Model scale testing is a commonly used method in the research on ice-structure interaction and in designing Arctic offshore structures. Model scale testing began in the 1970s and its purpose is to simulate full-scale processes in a miniature scale in a laboratory. The dimensions of the model scale structures typically vary from a few tens of centimetres (Timco, 1984a) to a few metres (Saarinen, 2000; Gürtner, 2009). The thickness of the ice is in the range of a few centimetres (Saarinen, 2000; Timco, 1984a) up to a few tens of centimetres (Gürtner, 2009). The tests are conducted in special facilities, ice tanks, shown in Figure 6. Ice tanks are large model basins where the temperature can be controlled and set below zero to simulate Arctic conditions.

Model scale experiments allow a testing environment where the majority of the uncertainties and the potential wide scatter of the full-scale measurements due to

Figure 6: Model scale experiments are conducted in special facilities called model ice basins. The Aalto Ice Tank is a large model basin where Arctic ice conditions can be simulated. (Image by the courtesy of Aalto University.)

ambiguity in parameterisation can be overcome at least to some extent. In a model scale experiment, the parameters, such as the ice thickness, the velocity of the ice sheet and the structure geometry, can be carefully controlled. Furthermore, the results can be monitored more reliably and the experiments are easier to reproduce than in full scale. However, due to the requirement for special facilities, the model scale experiments are somewhat difficult and expensive to realise, yet often cheaper than their full-scale counterparts. Furthermore, issues related to scaling may lead to misinterpretations when extrapolating the model scale results to full scale.

The results obtained in the laboratory have to be scaled according to so-called scaling laws which maintain the ratio of chosen characteristic parameters in order to make the results applicable in full scale. The majority of the model scale experiments are designed so that the so-called Froude and Cauchy numbers are kept constant when scaling from full scale to model scale. Another scaling method is to use a linear elastic fracture mechanics approach where the ice number At is kept constant (Palmer and Dempsey, 2009).

Froude scaling aims at maintaining the ratio between the inertia forces and the gravitational forces (Palmer and Croasdale, 2012). However, it omits the elastic behaviour of ice (Schwarz, 1977) and its use in many ice-structure interactions has been criticised by Palmer and Dempsey (2009). According to Palmer and Dempsey (2009), it is useless due to negligible inertial and gravitational forces induced by small velocities. Cauchy scaling aims at maintaining the ratio between the strength-related forces and the inertial forces when transferring between the scales. Thus it takes into account the material properties of the ice which are important parameters in ice failure (Schwarz, 1977). The ice number connects the forces associated with inertia to forces associated with fracture (Palmer and Croasdale, 2012). Scaling using the ice number has been criticised because it assumes a negligible fracture process zone, which does not hold for ice. To overcome the issues related to the traditional scaling methods, Palmer and Dempsey (2009) have suggested that the ratio of the length, the elastic modulus and the weakening rate of the ice should maintain a correct ratio. As a consequence, they conclude that sea ice is best modelled using sea ice.

The requirement for scaling has led to the development of so-called model ice that has been weakened with dopants in order to reach mechanical properties that are scalable with real sea ice (Palmer and Croasdale, 2012). A recent review of the most used model ice types is given by Lau *et al.* (2007). The microstructure of full-scale ice is often a composition of granular and columnar structures with varying grain size (Timco and Weeks, 2010), whereas the structure of model ice is homogeneous with either granular or columnar microstructure. Columnar model ice generally uses contaminants such as urea, ethylene glycol, detergents or sugar, whereas granular model ice uses salt, ethanol or urea. Granular ice is generally tougher than columnar ice, and it suffers from low compressive strength.

Model ice is grown under controlled conditions, as described in a review given by Timco (1984b). The dopants reduce the freezing temperature of water and the ice is thus grown under temperatures significantly below zero. A mist of water droplets is sprayed over a pre-cooled solution of the dopant and water. The droplets freeze in the subzero temperature and fall over the solution surface, nucleating the

growth of the ice. During freezing, the dopants are trapped within the growing ice sheet. When the desired ice thickness is reached, the temperature is raised so that internal melting is initiated by the dopant. As a result, liquid inclusions form in the ice and the amount of solid ice decreases. The desired mechanical properties of model ice are obtained by the choice of the type and concentration of the dopant and by controlling the air and the solution temperature at different phases of the ice formation process. In general, model ice tends to be more ductile compared with real sea ice, which may lead to over-predicted loads in model scale experiments (Palmer and Croasdale, 2012).

The loads in laboratory experiments are often measured similarly to full-sale experiments. The structures are typically instrumented with load cells (Evers and Weihrauch, 2004; Timco, 1984a; Lu *et al.*, 2014; Timco *et al.*, 1989), dynamometers (Karulin *et al.*, 2007; Timco *et al.*, 1989) or tactile sensors (Lu *et al.*, 2014). The tactile sensors are compromised of a set of sensing cells that convert the pressure into voltage recorded by a computer (Lu, 2014). Video recordings are also used to monitor the process and ice rubble accumulation as done, for instance, by Karulin *et al.* (2007) and Timco *et al.* (1989).

In the model scale experiments, either the structure can be moved while the ice remains stationary, or the ice can be moved while the structure stays fixed in place (Karulin *et al.*, 2007). The method where the structure is pushed against an immobile ice sheet is called the reverse-motion mode, whereas the method where ice is pushed against an immobile structure is called the direct-motion mode. The model scale experiments are often carried out in reverse-motion mode, as illustrated in Figure 7, which shows a typical test set-up of ice-structure interaction against an inclined wall (Lu *et al.*, 2013). The box with transparent walls is pushed into the intact ice from the left and sensors are attached to the model to measure the loads on the wall shown in dark brown.

Model scale experiments have been carried out to study various sea ice related problems. Examples of typical research problems include investigating vessel performance in ice (Zhou *et al.*, 2013), estimating ice encroachment along coastlines (Li *et al.*, 2009; Hopkins, 1997), researching the mechanical properties of ice (Liferov and Bonnemaire, 2005) and studying ice loads on static offshore structures. Määttänen *et al.* (2011) and Sodhi (2011) conducted experiments on ice crushing against a structure, whereas Määttänen *et al.* (2012) studied ice induced vibrations on structures. Ice-structure interaction against a wide upward sloping wall has been studied, for example, by Saarinen (2000) and Timco (1984a), whereas Lu *et al.* (2014) conducted experiments on a wide downward sloping wall.

Only a few reported model scale experiments have been conducted to study ice-structure interaction on wide inclined structures in shallow water. Timco *et al.* (1989) have studied load transmission through grounded rubble when the ice interacts with a vertical wall. The other reported tests are, in general, model scale studies on existing structures or conceptual studies on new possible designs rather than basic research on the effect of different parameters on ice-structure interaction in shallow water. Evers and Weihrauch (2004) and Gürtner (2009) have studied the possible designs of ice barriers to protect offshore structures, and Karulin *et al.*

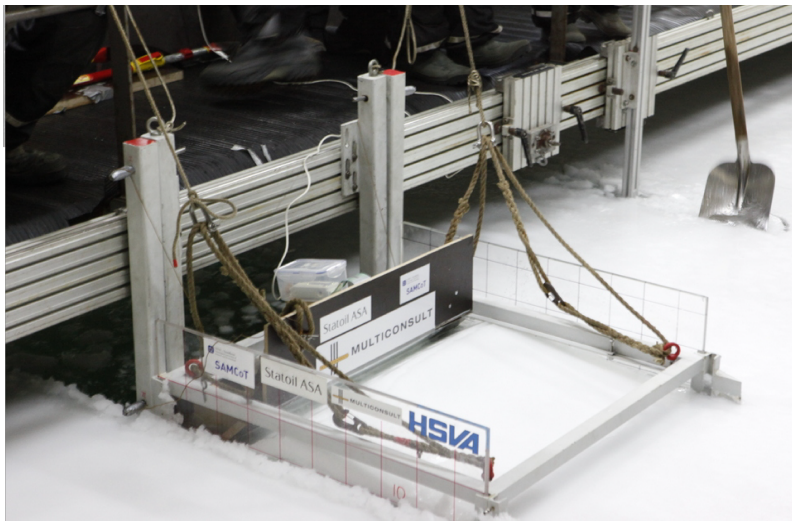

Figure 7: The model is pushed into the intact ice from the left in an experiment carried out in reverse-motion mode. (Image by courtesy of Wenjun Lu.)

(2007) have run model scale tests to study forces on an ice-resistant platform in the North Caspian Sea. In all these studies, the seabed has been modelled using plywood or a steel grid attached to a plywood plate.

2.3 Mathematical modelling

Mathematical ice load prediction techniques rely on analytical, empirical or semi-empirical equations, or numerical methods. Before sufficient knowledge on ice mechanics, especially fracture initiation, was obtained, the models used for ice load prediction for design purposes were empirical and based on full-scale data and probabilistic analysis (Sanderson, 1988).

As described by Sanderson (1988), the earliest theoretical studies on ice mechanics distinguished between the elastic and fracture behaviour of ice. An intact ice sheet exhibits elastic behaviour but as it fails, the fracture behaviour governs the process. The flexural fracture behaviour of ice was used as a basis of the first models estimating ice forces on sloping structures (see Figure 8). The models accounted for the force required to break the ice and an additional force to push the broken pieces of ice up the structure wall. A detailed description of such model is given in Sanderson (1988).

A similar, and one of the most well known analytical models for ice loads was developed by Croasdale *et al.* (1994). In addition to the force required to break the ice and the force to push the ice blocks up the structure wall, it includes components that account for rubble effects, such as the force to push ice through a rubble pile and the force to lift the rubble pile on top of the advancing ice before breaking it. Forces related to turning the ice blocks at the top of the slope are also included. With the careful choice of its many parameters, the model is able to produce reasonable predictions for ice loads on sloping structures. Furthermore, the force components

of the Croasdale model can be adjusted to suit specific situations, such as loading the structure with very thick ice or loading wide structures in shallow water. The model has been incorporated into the ISO Standard for Arctic Structures which sets standardised guidelines for the design and safe operation of Arctic offshore structures (International Organization for Standardization, 2008).

Related to the structures in shallow water studied here, Croasdale (2011) suggests that applying the ISO code in situations with grounded rubble requires modifications. In shallow water, the ISO standard is applicable at the initial stage of the ice-structure interaction. However, as more rubble forms and becomes grounded, the interaction is assumed to switch from flexural failure to rubbling mode. The advancing ice cannot penetrate the rubble accumulated in front of the structure and the ice begins to fail at the rubble edge. The model assumes that the ice loads become a function of ice rubbling against ice rubble and should therefore be treated similarly to ridge-building loads (Croasdale, 2012). To account for this, Palmer and Croasdale (2012) suggest an adjustment to the rubbling load given in the ISO standard. If this adjusted rubbling load is greater than the load predicted by the Croasdale model, it governs the design of an offshore structure. When the ice fails against an inclined structure, the adjusted rubbling load is likely to control. At later stages of the ice-structure interaction, the grounding resistance increases and the grounded rubble is assumed to protect the structure from loads.

The simplest method to estimate grounding resistance is to use a rigid body assumption, a widely used method in the early assessments of forces on the seabed (Sayed, 1989). It states that the horizontal force on the ice rubble-seabed interface is equal to the normal force acting on the seabed multiplied by the friction coefficient. However, several studies show that the interactions are more complex than that of a rigid body, and that the rigid body assumption tends to overestimate the grounding resistance, consequently underestimating the ice load on structure (Sayed, 1989; Timco *et al.*, 1989). Marshall et al. (1991) suggested a lumped element model which models the grounded rubble deformations as springs, dashpots and slider elements

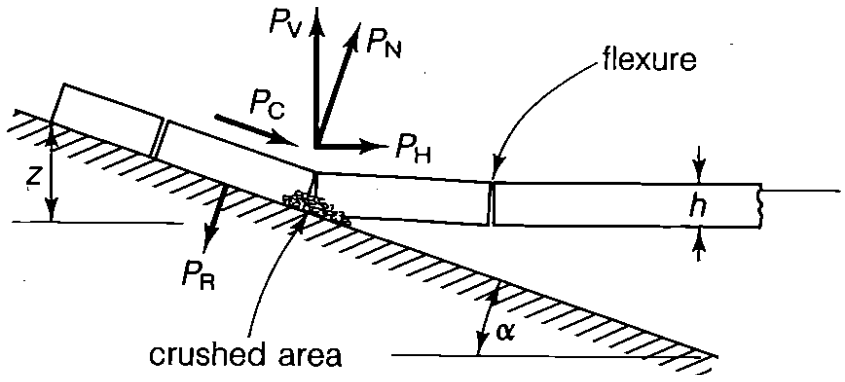

Figure 8: The first analytical models for ice forces on sloping structures were based on the flexural failure of ice. The models included the force to break the ice and a force to push ice blocks up along the structure wall (Sanderson, 1988).

as shown in Figure 9. The model takes into account the elastic, viscous and friction properties of consolidated and loose rubble, and includes the elastic and creep behaviour of the rubble. Marshall et al. (1991) used the lumped element model as an input in finite element analysis to make the calculation of the ice loads in the case of grounding computationally more straightforward.

Although the simplicity of analytical models may seem attractive, there are several features which make them poorly suited for thorough analysis. Firstly, all analytical models, including the Croasdale model and models introduced by Ralston (1977) and Nevel (1992), are based on strong idealisations of the mechanical behaviour of ice. Secondly, the determination of the total ice load is difficult. The effects of different events occurring during the ice-structure interaction process can be obtained through simple analysis but the coupling of these events is not straightforward. The analytical models do not take into account the simultaneity and interaction of different events. Furthermore, the analytical models can only be used to predict global loads and thus do not provide information on the local load distribution in the rubble pile (Paavilainen, 2013). In addition, the models cannot present all phenomena occurring in nature. An example of such phenomena omitted by the analytical models is the large-scale bending failure of ice caused by large sail piles (Paavilainen, 2013). Finally, the analytical equations do not yield information on the rubbling process, which would explain the fundamental reasons causing the peak loads.

To tackle the aforementioned issues with analytical equations, a number of sophisticated numerical models have been developed as the computational power has increased in recent decades. The models introduced here are divided into so-called continuum and discrete models (see Figure 10). The first numerical models for calculating ice loads were based on the finite element method (FEM). FEM based methods are still widely used and they treat the ice rubble forming in the interaction process as a continuum. This approach, however, smooths out the details of the

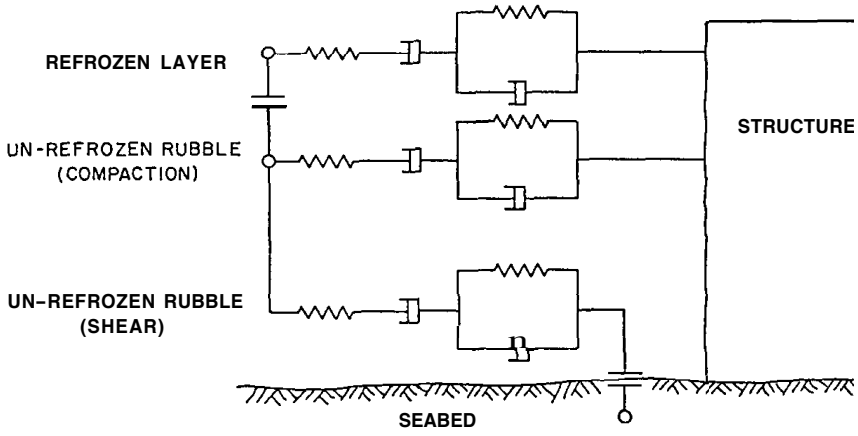

Figure 9: The lumped element model idealises the deformations of grounded rubble as a system of springs, dashpots and slider elements (Marshall et al., 1991).

load distribution in rubble (Heinonen, 2004). The continuum approach is computationally relatively light when compared with the discrete approach that treats the rubble as an assembly of individual particles. The difference between the continuum and discrete approaches is illustrated in Figure 10. Eulerian-Lagrangian formulation in the finite element framework has been used, for example, by Ranta *et al.* (2010) to model ice-structure interaction (see Figure 10a) and by Serré (2011) in ridge keel modelling. They modelled the rubble pile as a continuum deformable body using an Eulerian-Lagrangian formulation which allows for large displacements. The technique uses adaptive meshing to account for the deforming geometry of the rubble pile. In the works of Ranta *et al.* (2010) and Serré (2011), softening cohesive behaviour was implemented to account for the failure of the deforming rubble.

Modelling ice rubble behaviour is an essential part of studying ice-structure interaction. Therefore, various rubble models have been developed and implemented

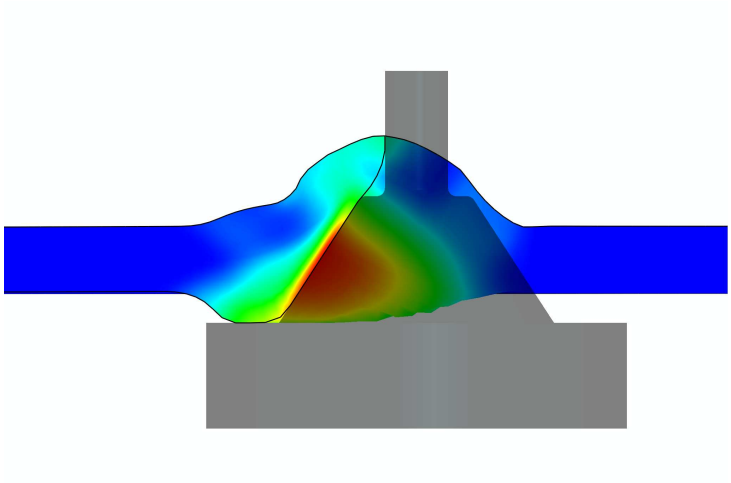

(a)

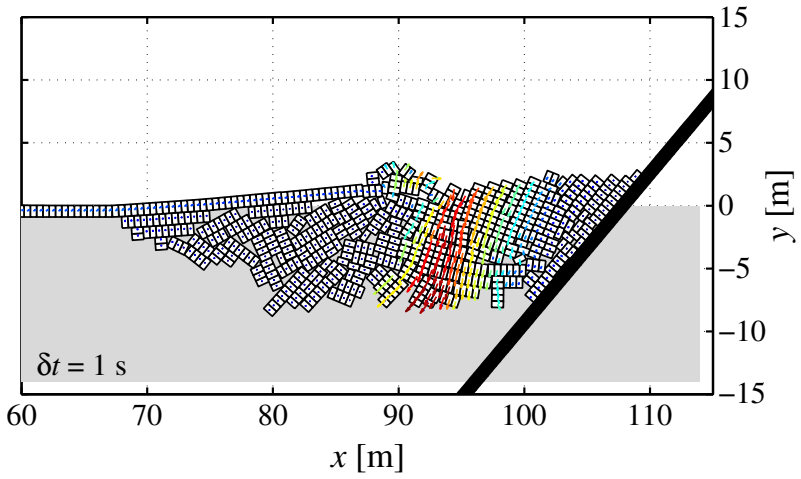

(b)

Figure 10: The ice rubble can be modelled (a) as a continuum (Ranta *et al.*, 2010) or (b) as an assembly of discrete blocks (Paavilainen *et al.*, 2011).

into commercial FEM software. The models assume that plastic deformation in the rubble occurs when some yield criterion is met. Therefore, the choice of the yield function is crucial in order to predict correct rubble behaviour. Heinonen (2004) has investigated different yield criteria to model rubble in ice ridge keels, including the Mohr-Coulomb model, the Drucker-Prager model and the yield cap surface model. The Mohr-Coulomb model is one of the most common yield criteria because it connects the material parameters to the shear strength in a straightforward manner. However, its implementation into an FEM solver requires modifications because the gradient of the yield surface is not continuous. The Drucker-Prager model is a widely used model in ice mechanics, and it is similar to the Mohr-Coulomb model. It can, in fact, be regarded as a smooth approximation of the Mohr-Coulomb model with a more suitable mathematical formulation for explicit finite element analysis (Serré, 2011). Both the models are cohesive-frictional models that are dependent on the hydrostatic pressure. These models do not, however, model the dilatation of the material correctly. Thus a cap yield surface can be added to the shear criterion in order to bound the yield surface in compression. The rubble will either become loose in shear or harden in compression when the failure criterion is met. Recently, however, Kulyathkin and Høyland (2015) critisised the Mohr-Coulomb model for its inconsistency with some shear strength measurements of ice rubble. Furthermore, choosing correct material parameters for the rubble may sometimes be ambiguous and challenging.

Liferov (2005) has used a pseudo-discrete continuum model to study rubble behaviour. In the model, a block generator tool produces an assembly of ice blocks that are used as an input in a finite element analysis. The individual blocks are modelled using an elastic-perfectly plastic Mohr-Coulomb material model and the voids between the blocks are modelled as an elastic material with negligibly low stiffness. The model is able to capture contacts between the individual blocks and their local failure.

The conventional numerical methods to model material separation upon fracture of ice are based either on element deletion of failed elements or on a discrete cracking model that requires a predefined crack path. In addition, the simulation is usually terminated after the material has fully failed. To tackle these inconveniences, Kolari (2007) developed a continuum damage mechanics model that has been used by Kolari *et al.* (2009) to model continuous ice failure against an inclined structure. The material model developed by Kolari (2007) assumes an anisotropic material and a brittle failure mode. It gives information on the direction of the crack growth, and a special model update technique is applied to propagate the crack. The technique appears to be suitable for modelling the transition from continuous to discontinuous material but its implementation into commercial FEM software is complicated.

The so-called cohesive element method has been used to model various ice-structure interaction problems. The method is based on implementing cohesive elements into the finite element framework to account for the cohesive fracture model (see Figure 11). The method is applicable for simulating dynamic ice-structure interaction with interacting particles. Konuk *et al.* (2009) used the method to model ice forces on a cylindrical structure, whereas Lu (2014) studied interactions between

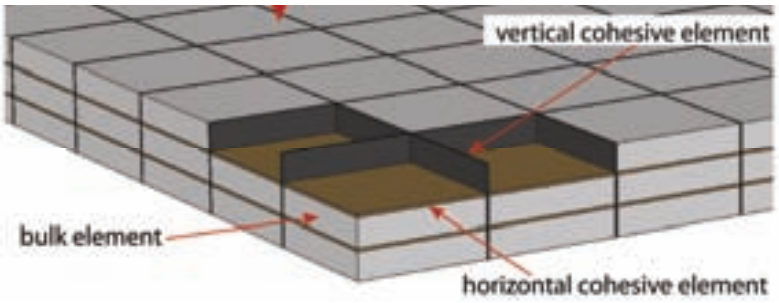

Figure 11: The so-called cohesive element method accounts for cohesive fracture model by incorporating cohesive elements in the finite element framework (Gürtner, 2009).

ice floes and wide downward sloping structures and cones with this method. Gürtner (2009) has simulated ice barriers with inclined walls in shallow water using a computational cohesive element model. Even if the model has been used to study the aforementioned processes, the use of the cohesive element method is hampered by convergence issues (Lu, 2014).

Barker and Croasdale (2004) and Barker and Timco (2007) have used a particle-in-cell (PIC) model to study rubble accumulation in front of structures in shallow water. In the PIC approach, the ice cover is discretised into individual particles. Each particle is assigned a fixed volume, area and thickness. The governing equations are solved in a fixed grid using an implicit finite difference method, whereas advection and continuity are solved in a Lagrangian manner. The solutions of these two sets of equations are mapped between the grid and the individual particles to obtain the updated velocities and stresses on the ice. The PIC approach has been criticised for its possible inability to actually fulfil the governing continuum conservation laws (Gürtner, 2009).

As already mentioned above, the conventional approach to model the rubble as a continuum cannot reproduce the interactions between the individual ice blocks. Therefore, the recent developments in ice mechanics have focused on the discrete element method (DEM) or the combined finite-discrete element method (FEM-DEM) illustrated in Figure 10b. DEM treats the ice blocks as rigid particles, whereas FEM-DEM accounts for the elastic behaviour of the blocks. Compared with the continuum approach, DEM has the advantage that the material parameters for the ice rubble are not required, but they ideally emerge from the ensemble behaviour of the individual blocks in the simulations. 2D DEM approach was used by Hopkins (1997) to study ice pile-up on shorelines. Furthermore, the method has been used to study ice ridge building, for example, by Hopkins *et al.* (1991), Hopkins (1994) and Hopkins *et al.* (1999). The early models treated the rubble as an assembly of disc-shaped elements (see Figure 12a) but later rectangular elements have been widely used in the DEM simulations (see Figure 12b). Hopkins and Hibler (1991) used DEM to simulate shear box test on ice rubble. A shear box test is a widely used method to determine the shear strength of a granular material, such as ice rubble. 2D DEM simulations on ice rubble shear box tests have recently been con-

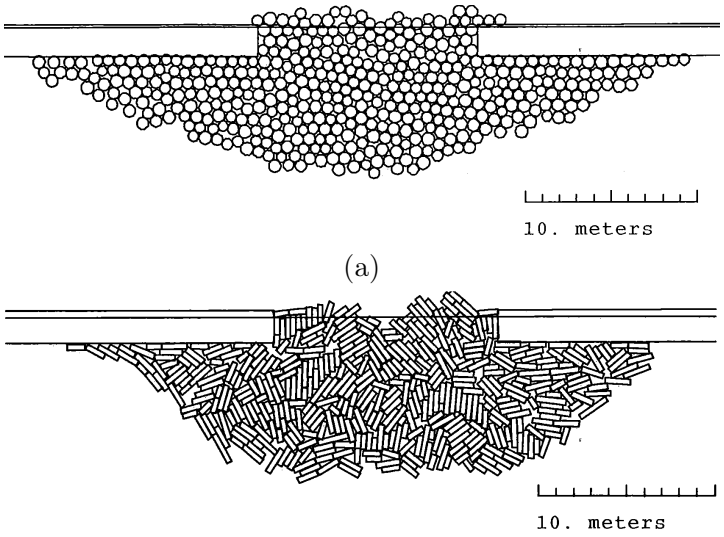

(a)

(b)

Figure 12: The 2D discrete element method has been used to model ridge building. The rubble in the simulations (a) was first modelled as an assembly of circular discs but (a) later rectangular elements have been widely used (Hopkins *et al.*, 1991).

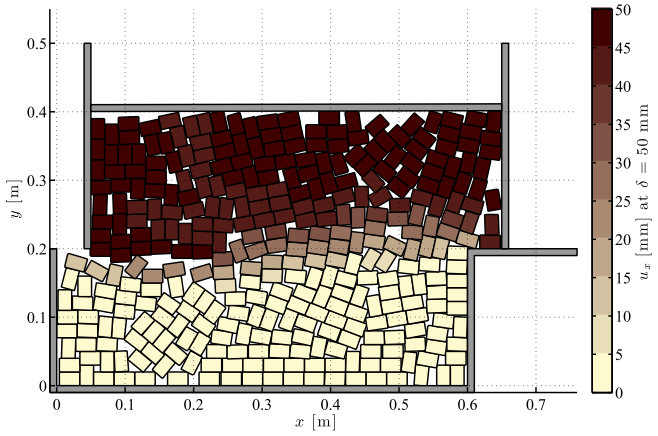

Figure 13: DEM has recently been used, for example, to simulate shear box tests on ice rubble (Polojärvi *et al.*, 2015).

ducted by Polojärvi *et al.* (2015) to study the load transmission and peak loads in shear box tests (see Figure 13). Goldstein *et al.* (2013) studied rubble grounding in shallow water using a DEM approach and proposed modifications to the analytical Croasdale model based on the simulation results. In addition, the discrete approach has been used to study ridge keel punch through tests (Polojärvi and Tuhkuri, 2009, 2013) and ice-structure interaction against an inclined wall (Paavilainen *et al.*, 2010, 2011; Paavilainen and Tuhkuri, 2012, 2013). The FEM-DEM approach is described in detail in the next chapter.

3 FEM-DEM Simulations

This section presents the mechanics of the combined finite-discrete element method (FEM-DEM) simulations of the ice structure-interaction process, and describes the different cases that were simulated in order to investigate the phenomena related to the rubbling process.

The rubbling process of the ice sheet and the interaction between the ice, the structure and the seabed are modelled using two-dimensional combined finite-discrete element method simulations developed at Aalto University and validated by Paavilainen *et al.* (2009, 2011). The ice sheet and its failure into smaller ice blocks are modelled using the finite element method whereas the discrete element method is used to account for the contact detection and the contact force calculation of the interacting ice blocks. The method is able to capture the deformation of the continuous ice sheet and its fracture into smaller ice blocks that can interact with each other and further break into smaller pieces.

The discrete element method is a technique that was developed in the 1970s to model the nonlinear dynamics of granular media (Cundall and Strack, 1979). It is used to model particle interactions, and the common applications of FEM-DEM outside the field of ice mechanics include geomechanics, civil engineering and process engineering. It has been used, for example, by Morris *et al.* (2006), Oñate and Rojek (2004) Ibrahimbegovic and Delaplace (2003), Owen *et al.* (2004) and Munjiza (2004).

The purpose of the FEM-DEM is to solve the equations of motion of a system of interacting particles by contact detection and contact force calculation algorithms. Figure 14 illustrates a system of particles that are interacting with each other and subject to internal and external loads. The equations of motion of the system in Figure 14 are

$$\mathbf{M}\ddot{\mathbf{x}} = \mathbf{f}_{int} + \mathbf{f}_{con} + \mathbf{f}_{ext}, \tag{1}$$

where $\mathbf{M}$ is a diagonal mass matrix which contains the masses and the moments of inertia of the discrete elements and $\ddot{\mathbf{x}}$ is the second time derivative of the position vector $\mathbf{x}$, corresponding to the translational and angular acceleration of the elements. The vectors $\mathbf{f}_{int}$, $\mathbf{f}_{con}$ and $\mathbf{f}_{ext}$ contain the internal forces and moments, contact forces and moments and external forces and moments acting on the elements of the system. The force components also contain dissipative forces from damping, friction and water drag. The acceleration $\ddot{\mathbf{x}}$ is solved explicitly according to Newton's laws of motion. The internal forces are obtained using the finite element method and the contact forces are solved using the discrete element method.

The position vector $\mathbf{x}$ contains the positions x_i, y_i, rotations θ_i and orientations of each discrete element. It is written as

$$\mathbf{x} = [x_1 \quad y_1 \quad \theta_1 \quad \dots \quad x_N \quad y_N \quad \theta_N]^T, \tag{2}$$

where N is the number of discrete elements in the system. The point of application of the torque of each discrete element is added accordingly.

The solution of Equation (1) for one discrete element is written as

$$\ddot{x}_i = \frac{f_{int,i} + f_{col,i} + f_{ext,i}}{M_i}, \tag{3}$$

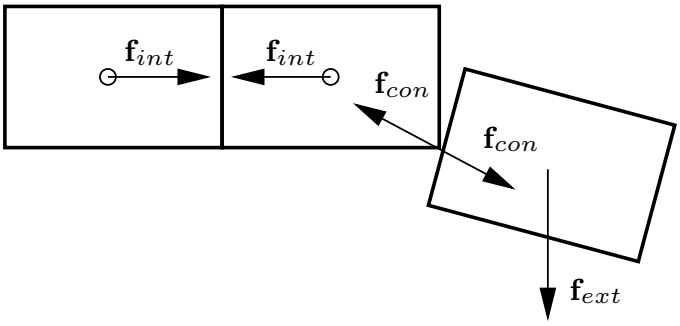

Figure 14: Interacting particles are subject to internal forces $\mathbf{f}_{int}$ due to beam elasticity, contact forces $\mathbf{f}_{con}$ from colliding particles and external forces $\mathbf{f}_{ext}$ due to, for example, gravity or drag.

which is a function of time. Thus, to obtain the solution, the equations are discretised with respect to time. As described in Paavilainen *et al.* (2009), the trajectories of the blocks are solved explicitly at each time step using central difference scheme, which corresponds to the Newmark time integration scheme with parameters $\beta = 0$ and $\gamma = \frac{1}{2}$. According to this scheme, the velocities $\mathbf{v}$ and positions $\mathbf{x}$ are given by

$$\mathbf{x}_{k+1} = \mathbf{x}_k + \Delta t \dot{\mathbf{x}}_k + \frac{\Delta t^2}{2} \ddot{\mathbf{x}}_k \tag{4}$$

$$\mathbf{v}_{k+1} = \dot{\mathbf{x}}_{k+1} = \dot{\mathbf{x}}_k + \frac{\Delta t}{2} \left(\ddot{\mathbf{x}}_k + \ddot{\mathbf{x}}_{k+1} \right), \tag{5}$$

where the subscript k denotes the time step, $\dot{\mathbf{x}}$ is the first time derivative of the position vector and Δt is the time step size.

The forces in Equation (1) are solved for each element during one time step. The following tasks are performed during one time step:

(1) Determination of internal forces and moments in the continuum part of the model,

(2) applying the failure model if failure criterion is met,

(3) contact search of the blocks that are in the vicinity of each other,

(4) determination of the contact forces,

(5) adding the external forces

(6) updating the node positions by solving the equations of motion.

The following chapters describe each of these steps. Step (1) is described in Section 3.1 and Step (2) in Section 3.2. Steps (3) and (4) are explained in Section 3.3 and the external forces in Step (5) are given in Section 3.4. Finally, step (6) is completed based on the solutions of the previous steps and the Equations (1), (4) and (5).

3.1 Continuum Model

The intact ice sheet and the pieces of ice fractured from it are modelled as continuum and the finite element method (FEM) is used to obtain the internal forces $\mathbf{f}_{int}$ acting in the system. FEM is a widely used numerical technique that discretises the problem domain into finite elements. The displacement is approximated over each element by a polynomial and the solution for the whole domain is constructed by connecting the elements. The formulation of the method is rigorous, which makes it feasible to model complicated problems and nonlinearities (Reddy, 2004).

The ice sheet exhibits nonlinear kinematic behaviour, which is included in the model by using C^0 continuous nonlinear Timoshenko beam elements. The nonlinear analysis is required because the ice undergoes large displacements and rotations and fracture. Furthermore, small deformations are assumed in the finite element formulation. The kinematics of a Timoshenko beam is illustrated in Figure 15 and can be expressed as follows: during deformation, the cross sections remain plane and rotate about the neutral axis of the cross section. They do not, however, necessarily remain perpendicular to the deformed longitudinal beam axis due to shear. The plane sections are assumed to be rigid, which means that their dimensions do not change as the beam undergoes deformation. Furthermore, the transverse shear stress is assumed to have a constant value over the plane section (Felippa, 2001). Linear stress–strain relation and a viscous damping model are utilised to account for the Hookean material behaviour and the dynamic nature of the analysis (Paavilainen *et al.*, 2009).

The intact ice sheet is assumed to be a homogeneous, isotropic continuum that exhibits linearly elastic material behaviour up to its failure. The ice sheet consists of N rectangular discrete elements that are joined together with finite beam elements so that the centroid of each discrete element corresponds to a node of a beam element as illustrated in Figure 16. The Timoshenko beam elements used here share the same degrees of freedom as the discrete elements: translation in x- and y- directions and a rotation perpendicular to the xy-plane. Since the element nodes coincide with the centroids of the discrete elements, the internal forces of the beam can be superposed to the discrete elements.

When the ice sheet fails, it breaks into smaller fragments which are also considered discrete Timoshenko beams if they consist of more than one discrete element. Fragments consisting of only one discrete element are treated as rigid bodies. These beam and rigid body fragments formed in the process then interact with each other and with the structure.

The formulation of the model is based on Lagrangian kinematics and it is largely based on work by Felippa (2001). The beam element illustrated in Figure 15 moves from its original position $P_0(X, Y)$ in the reference configuration to the location $P(x, y)$ in the current configuration. The displacement of the point is given by

$$\begin{bmatrix} x \\ y \end{bmatrix} = \begin{bmatrix} x_C - Y\left[\sin\theta + (1-\cos\gamma)\sin\psi\right] \\ y_C + Y\left[\cos\theta + (1-\cos\gamma)\cos\psi\right] \end{bmatrix}, \tag{6}$$

where the subscript C denotes the projection of the point P on the neutral axis

and Y indicates the distance from the neutral axis. The angles θ, γ and ψ are the total rotation of the cross section from the reference to the current configuration, the shear distortion angle and the rotation of the beam axis, respectively.

Assuming that the shear distortion γ is a small quantity, the term $1 - \cos\gamma$ in Equation (6) tends to zero. Furthermore, the coordinates (x_C, y_C) can be expressed as $x_C = X + u_X$ and $y_C = u_Y$. Thus the Equation (6) simplifies to

$$\begin{bmatrix} x \\ y \end{bmatrix} = \begin{bmatrix} X + u_X - Y\sin\theta \\ u_Y + Y\cos\theta \end{bmatrix}, \tag{7}$$

which is a function of X only.

The displacement and rotations at the nodes are used to derive the strains. To that end, a deformation gradient $\mathbf{F}$ is constructed. $\mathbf{F}$ maps an infinitesimal material vector $\mathrm{d}\mathbf{X}$ in the reference configuration into an infinitesimal vector $\mathrm{d}\mathbf{x}$ in the current configuration (Malvern, 1969). The deformation gradient of the kinematic

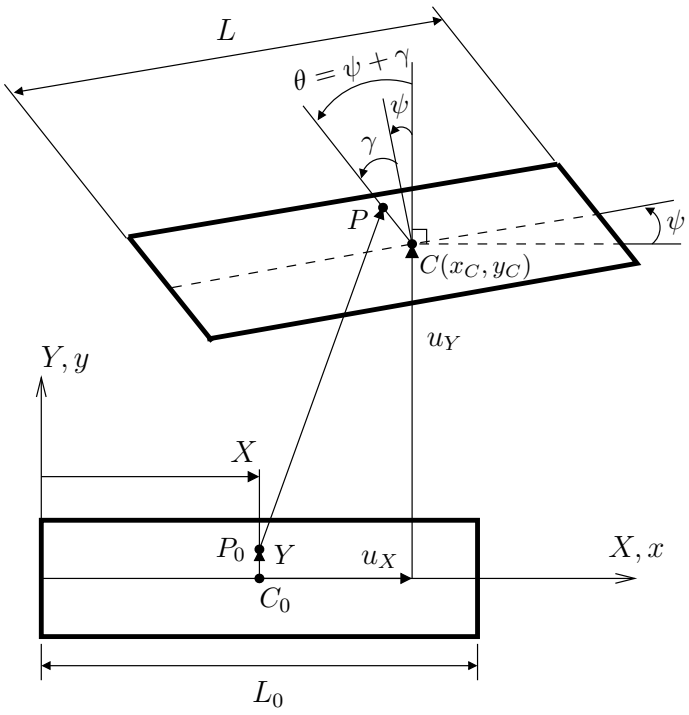

Figure 15: The cross sections of a Timoshenko beam remain plane but not necessarily normal to the neutral axis of the cross section during deformation. A particle $P_0(X, Y)$ of a C^0 Timoshenko beam element in the reference configuration moves to a new location $P(x, y)$ in the current configuration. L_0 is the initial length of the element and L the length in the current configuration. The angles ψ, γ and θ are the rotation of the beam axis, the shear distortion angle and the total rotation of the cross section, respectively.

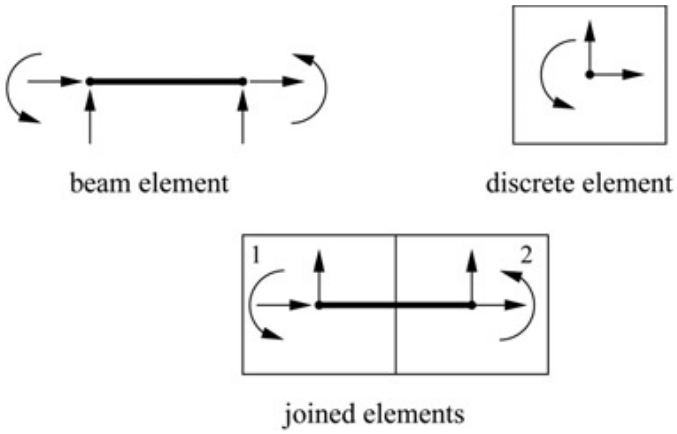

Figure 16: The individual discrete elements are joined together by nonlinear Timoshenko beam elements so that the nodes of the beam elements coincide with the centroids of the discrete elements. The arrows show the degrees of freedom of the elements (Paavilainen *et al.*, 2009).

description (7) is given as

$$\mathbf{F} = \begin{bmatrix} \frac{\partial x}{\partial X} & \frac{\partial x}{\partial Y} \\ \frac{\partial y}{\partial X} & \frac{\partial y}{\partial Y} \end{bmatrix} = \begin{bmatrix} 1 + u'_X - Y\theta' \cos\theta & -\sin\theta \\ u'_Y - Y\theta' \sin\theta & \cos\theta \end{bmatrix}. \tag{8}$$

The deformation gradient $\mathbf{F}$ is needed to construct a Green-Lagrange strain tensor $\mathbf{E}$. The Green-Lagrange strain tensor gives the element strains with respect to the undeformed lengths (Reddy, 2004). It is used because it is independent of rigid body translation and rotation, which makes it suitable for studying strains in a system with large rigid body displacements. It can be expressed in terms of the deformation gradient as

$$\mathbf{E} = \frac{1}{2}\left[\mathbf{F}^T \cdot \mathbf{F} - \mathbf{I}\right], \tag{9}$$

where $\mathbf{I}$ is an identity tensor. According to Reddy (2004), the deformation gradient $\mathbf{F}$ can further be decomposed into an orthogonal rotation tensor $\mathbf{R}$ and a symmetric stretch tensor $\mathbf{U}$ as

$$\mathbf{F} = \mathbf{R} \cdot \mathbf{U}. \tag{10}$$

An orthogonal tensor satisfies the condition $\mathbf{R}^T \cdot \mathbf{R} = \mathbf{I}$. Thus after some manipulation and assuming small strains, the strain tensor (9) gets the following form:

$$\mathbf{E} = \begin{bmatrix} \epsilon_{XX} & \epsilon_{XY} \\ \epsilon_{YX} & \epsilon_{YY} \end{bmatrix} = \frac{1}{2}\left(\mathbf{L} + \mathbf{L}^T\right), \tag{11}$$

where the relation $\mathbf{U} = \mathbf{I} + \mathbf{L}$ is utilised. The tensor $\mathbf{L}$ is first-order linearisation according to Felippa (2001). The manipulation of Equation (9) yields $\epsilon_{YY} = 0$, and

after linearisation described by Felippa (2001), the strain vector can be written as

$$\mathbf{e} = \begin{bmatrix} e_1 \\ e_2 \end{bmatrix} = \begin{bmatrix} \epsilon_{XX} \\ 2\epsilon_{XY} \end{bmatrix} = \begin{bmatrix} (1+u'_X)\cos\theta + u'_Y \sin\theta - Y\theta' - 1 \\ -(1+u'_X)\sin\theta + u'_Y\cos\theta \end{bmatrix} = \begin{bmatrix} \epsilon - Y\kappa \\ \gamma \end{bmatrix}, \quad (12)$$

where the axial strains ϵ, shear strains γ and curvatures $\kappa = \theta'$ can be collected in the generalised strain vector $\mathbf{h} = [\epsilon \quad \gamma \quad \kappa]^T$.

The original length of the beam element L_0 and the current length of the beam element L can be used to determine the relations $1 + u'_X = L\cos\psi/L_0$ and $u'_Y = L\sin\psi/L_0$ from the geometry as shown in Felippa (2001). Substituting these into the strain expression (12) the following computationally more efficient expression for the strain vector is obtained:

$$\mathbf{e} = \begin{bmatrix} e_1 \\ e_2 \end{bmatrix} = \begin{bmatrix} \frac{L}{L_0}(\cos\psi\cos\theta + \sin\psi\sin\theta) - 1 - Y\theta' \\ -\frac{L}{L_0}(\cos\psi\sin\theta - \sin\psi\cos\theta) \end{bmatrix} = \begin{bmatrix} \epsilon - Y\kappa \\ \gamma \end{bmatrix}. \quad (13)$$

The only non-zero stresses are the normal stress σ_x and the shear stress τ due to the assumption of linear elasticity. These stresses can be connected with the strains in Equation (12) using the linear constitutive equation

$$\mathbf{s} = \begin{bmatrix} \sigma_x \\ \tau \end{bmatrix} = \begin{bmatrix} E & 0 \\ 0 & G \end{bmatrix} \begin{bmatrix} e_1 \\ e_2 \end{bmatrix} = \mathbf{C}\mathbf{e}, \quad (14)$$

where E is the elastic modulus, G is the shear modulus and $\mathbf{C}$ is the stiffness matrix.

When the stresses are integrated over the cross section of an element, the following stress resultants are obtained:

$$N = \int_{A_0} \sigma_x \,\mathrm{d}A, \quad Q = \int_{A_0} \tau \,\mathrm{d}A, \quad M = \int_{A_0} \sigma_x Y \,\mathrm{d}A, \quad (15)$$

where A_0 denotes the area of the cross section in the reference configuration. N represents the axial force, Q represents the transverse shear force and M represents the bending moment. The stress resultants are calculated in the current configuration. In addition, viscous forces are introduced to account for material damping. The axial damping N_d, shear damping Q_d and damping moment M_d are defined as

$$N_d = \nu \int_{A_0} (\dot{\epsilon} - Y\dot{\kappa}) \,\mathrm{d}A, \quad Q_d = \nu \int_{A_0} \dot{\gamma} \,\mathrm{d}A, \quad M_d = c_i \int_{A_0} (\dot{\varepsilon} - Y\dot{\kappa}) Y \,\mathrm{d}A, \quad (16)$$

where c_i is an internal damping coefficient and $\dot{\epsilon}$, $\dot{\gamma}$ and $\dot{\kappa}$ are strain rates related to the stains $\mathbf{h}$ introduced above. The damping forces are added to the equivalent stress resultants and collected in a stress resultant vector

$$\mathbf{p} = [N + N_d \quad Q + Q_d \quad M + M_d]^T. \quad (17)$$

The internal forces $\mathbf{f}_{int}$ in the equations of motion in Equation (1) can be obtained from the stress resultant vector $\mathbf{p}$ through variation of the beam strain energy. The

strain energy of the beam corresponds to the internal energy of the beam and can be written as

$$U = \frac{1}{2}\int_{V_b} Ee_1^2 + Ge_2^2 \,\mathrm{d}V, \tag{18}$$

where V_b is the volume of the beam element. Utilising the expressions (14) through (17) and taking the first variation of the strain energy with respect to the nodal displacements $\mathbf{u} = [u_{X1} \quad u_{Y1} \quad \theta_1 \quad u_{X2} \quad u_{Y2} \quad \theta_2]^T$ of the two-node C^0 element, the following expression for the variation of the strain energy is obtained:

$$\delta U = \int_{L_0} \mathbf{p}^T \delta \mathbf{h} \,\mathrm{d}X = \int_{L_0} \mathbf{p}^T \mathbf{B} \delta \mathbf{u} \,\mathrm{d}X = \mathbf{f}_{int}^T \delta \mathbf{u}. \tag{19}$$

The matrix $\mathbf{B}$ is a kinematic matrix that connects the strains and nodal displacements as it contains the partial derivatives of the strains with respect to the nodal displacements (Felippa, 2001). Based on Equation (19) the internal forces are thus

$$\mathbf{f}_{int} = \int_{L_0} \mathbf{B}^T \mathbf{p} \,\mathrm{d}X. \tag{20}$$

The internal forces are evaluated using one-point Gauss integration at the midpoint of the beam element.

3.2 Fracture Model

The ice sheet is subjected to stresses when it interacts with the structure, the seabed or the ice blocks formed in the process. To account for the fracture process of the ice sheet, a cohesive crack model is used. When the stress state in the ice reaches a critical limit, the sheet fails and fractures into smaller ice blocks.

The cohesive crack model was developed by Hillerborg *et al.* (1976). It provides an approach to fracture mechanics which takes into account both the formation and the propagation of the crack. This makes it more suitable for the analysis of the simulations here than other models, such as the stress intensity factor approach and the energy balance approach, as they can only model crack propagation. Furthermore, many fracture models require a dense element mesh in the vicinity of the crack. When the cohesive crack model is used, there is no need for a dense mesh, which makes it applicable to a wide range of complicated problems (Hillerborg *et al.*, 1976).

In the cohesive crack model, the stresses are assumed to act over a narrowly opened crack until a critical crack opening displacement δ_f is reached. The model can be applied on quasi-brittle materials with mixed mode failure to take into account the normal and shear stresses and their coupling (Gálvez *et al.*, 2002). Normally, the crack path has to be predicted as a part of the analysis when the cohesive crack model is used. However, when the model is applied on the ice sheet here, the failure is assumed to occur at the interface of two discrete elements so that the crack propagates straight through the beam. Therefore, the crack path is known and it does not have to be predicted.

As mentioned in Gálvez *et al.* (2002), the cohesive crack model assumes that three distinct process zones can be identified when the material undergoes failure. These zones are illustrated in Figure 17. First, the material is intact and it has not reached its critical strength. Second, in the cohesive crack zone, the material is partially damaged but the remaining ligaments of material transfer stress across the damaged area. However, as the material is partially damaged in the cohesive crack zone, its stress carrying capacity decreases. Finally, in the third phase the material is fully damaged and it is not able to transmit stresses across the crack. This is called the true crack.

According to the cohesive crack model, the stress in the cohesive crack zone is assumed to be a function of the crack opening displacement δ, illustrated in Figure 17, so that $\sigma = \sigma(\delta)$. As the crack opening displacement increases, the stress decreases. This relation is called the softening function and it is regarded as a material property (Gálvez *et al.*, 2002). In the current model, a linear softening function is used for its simplicity and suitability for FEM analysis with quasi-brittle material. A linear softening function describing the failure process under uniaxial loading is illustrated in Figure 18a. It can be related to the specific fracture energy G_f through

$$G_f = \int_0^{\delta_f} \sigma \, \mathrm{d}\delta = \frac{\sigma_{cr}\delta_f}{2}, \tag{21}$$

where G_f is the specific fracture energy corresponding to the area under the curve. It represents the amount of energy needed to first create a cohesive crack and fully break a unit surface area of it (Hillerborg *et al.*, 1976). δ_f is the critical crack opening displacement which indicates the crack length at which the stress has fallen to zero and a true crack has formed. σ_{cr} is the tensile strength which, together with G_f, is amongst the most important parameters associated with the cohesive crack

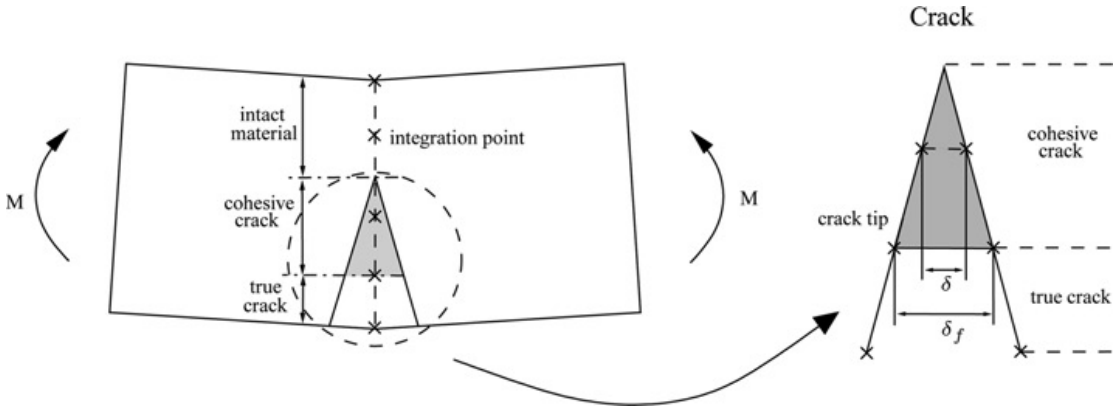

Figure 17: Three zones can be distinguished in an advancing crack: the intact material, the cohesive crack and the true crack. In the figure, M is the bending moment, δ is the crack opening displacement and δ_f is the critical crack opening displacement (Paavilainen *et al.*, 2009).

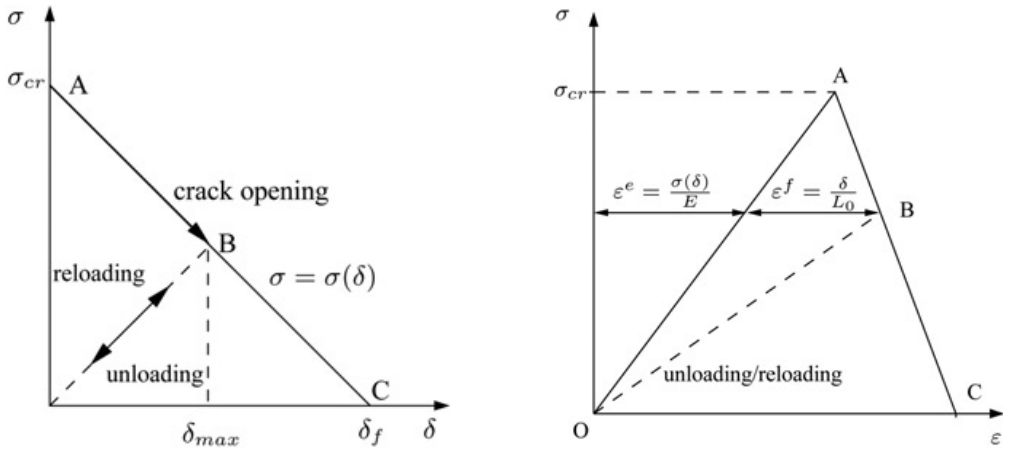

Figure 18: (a) The cohesive stress σ, which is a function of the crack opening displacement δ, is approximated by a linear softening function. σ_{cr} is the tensile strength and δ_f is the critical crack opening displacement. (b) The material is assumed to exhibit linear elastic behaviour up to the crack initiation at the point A. After the crack initiation, the total strain ε is calculated as a sum of the elastic ε^e and inelastic ε^f strains. In the figure, E is the elastic modulus and L_0 is the element length in the reference configuration. The points A, B and C correspond to the same phase of the fracture in (a) and (b) (Paavilainen *et al.*, 2009).

model in Mode I opening (Gálvez *et al.*, 2002). Both these parameters are material parameters that can be obtained from experiments. Dempsey *et al.* (1999) measured G_f values for ice, which makes it a suitable parameter for the current model.

When the stress state exceeds the tensile strength σ_{cr}, a cohesive crack is formed and starts to open. Breaking the material bridges that transmit the stress across the cohesive crack zone requires energy. When the absorbed energy equals G_f, the material bonds break and the crack advances from a cohesive crack to a true crack.

The constitutive relation in Figure 18b illustrates the behaviour of the material. The stress grows linearly with the strain up to point A when the linear elastic stress reaches its critical value σ_{cr} and a crack forms. After the crack has formed, the material behaviour changes and the post-peak strain at point B can be determined as a sum of elastic and inelastic strain as

$$\varepsilon = \varepsilon^e + \varepsilon^f = \frac{\sigma(\delta)}{E} + \frac{\delta}{L_0}, \tag{22}$$

where ε^e and ε^f are the elastic and inelastic strains, respectively, and L_0 is the original length of a beam element in the reference configuration. The material is considered fully damaged at point C when the crack opening displacement reaches its critical value δ_f and the material loses its ability to sustain loads (Paavilainen *et al.*, 2009).

The above holds for a uniaxial stress state. However, the current model assumes that the failure of the ice sheet is caused by tensile and shear stresses. Therefore,

mixed mode failure has to be taken into account in the failure criterion F. After Paavilainen *et al.* (2009), F is here chosen to be

$$F = \frac{\sigma_x}{\sigma_{cr}} + \frac{\tau^2}{\tau_{cr}^2} + \frac{\delta_{max}}{\delta_f} - 1 \leq 0, \tag{23}$$

where σ_x and τ are the normal and shear stresses, respectively, and σ_{cr} and τ_{cr} are the critical stresses corresponding to them. The maximum crack opening displacement δ_{max} is an increasing variable that makes the process irreversible by keeping track of the maximum value of the reached crack opening displacement as shown in Figure 18a. The definition $F \leq 0$ indicates that a stress state at which $F > 0$ is not allowed. When $F < 0$ the failure is not advancing, the material is undamaged or the material is under unloading. A stress state which gives $F = 0$ indicates the initiation of failure (Paavilainen *et al.*, 2009; Schreyer *et al.*, 2006).

An effective stress σ can be used in Equation (23) to account for normal and shear stresses. It is defined as

$$\sigma = \sigma_x + \frac{\sigma_{cr}}{\tau_{cr}^2}\tau^2. \tag{24}$$

When this effective stress is substituted into F in Equation (23), the failure criterion can be expressed as a function of σ and δ_{max} as follows:

$$F(\sigma, \delta_{max}) = \sigma - \sigma_{cr}\left(1 - \frac{\delta_{max}}{\delta_f}\right) \leq 0. \tag{25}$$

The failure progress is studied by computing a trial stress state. The trial stress can be obtained from the post-peak strain in Equation (22) and the failure criterion in Equation (25). It is determined by

$$\delta_{max,k+1}^{\text{trial}} = \delta_{max,k} \tag{26}$$

$$\sigma_{k+1}^{\text{trial}} = E\left(\varepsilon_{k+1} - \frac{\delta_{max,k+1}^{\text{trial}}}{L_0}\right) \tag{27}$$

$$F_{k+1}^{\mathbf{trial}} = \sigma_{k+1}^{\text{trial}} - \sigma_{cr}\left(1 - \frac{\delta_{max,k+1}^{\text{trial}}}{\delta_f}\right), \tag{28}$$

where the subscript k denotes a time increment. According to the failure criterion (25), the crack grows if the trial state gives $F > 0$. In that case, return mapping to the failure surface $F = 0$ according to Paavilainen *et al.* (2009) is required. The new failure surface $F = 0$ can be calculated after determining the values of σ and δ. In the return mapping process illustrated in Figure 19, a point (σ_1, τ_1) is mapped to a point (σ_1^*, τ_1^*) on the failure surface $F(\sigma, \delta_{max} \neq 0) = 0$. The ratio between normal stresses and shear stresses is kept constant in the return mapping so that $\frac{\sigma_1}{\tau 1} = \frac{\sigma_1^*}{\tau_1^*}$.

After the failure initiation, the load-carrying capacity of the material decreases and the stress in the cohesive zone can be expressed as a function of the crack

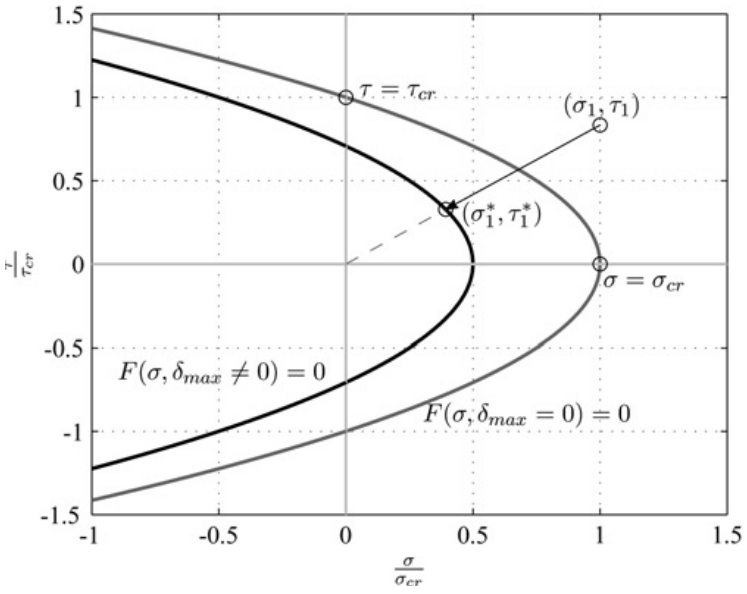

Figure 19: Return mapping is performed to return to the failure surface $F = 0$ given by Equation (23) (Paavilainen *et al.*, 2009).

opening displacement as

$$\sigma = \sigma_{cr} \left(1 - \frac{\delta}{\delta_f} \right). \tag{29}$$

The total strain is known so the new crack opening displacement δ can be determined from the post-peak strain in Equation (22). When the crack is opening, the crack opening displacement automatically corresponds to the maximum crack opening displacement $\delta = \delta_{max}$.

The state $F < 0$ and the stress $\sigma_x \geq 0$ indicates that the material is under unloading or reloading, provided that a crack has formed (see Figures 18a and 18b). When the unloading or reloading case is active, the stress in the cohesive zone is given by

$$\sigma = \sigma_{cr} \left(\frac{\delta}{\delta_{max}} - \frac{\delta}{\delta_f} \right). \tag{30}$$

Since σ here applies for unloading or reloading, the maximum crack opening displacement δ_{max} in the previous equation has a constant value reached in the crack opening phase. The crack opening displacement is calculated from Equation (22) using this constant value. According to Paavilainen *et al.* (2009), when the stress state is such that $F < 0$ and $\sigma_x < 0$, the crack is closing and the material is treated as if it was undamaged. In this case, $\sigma = 0$ and σ_{max} equals a constant obtained in the crack opening phase.

The normal stress in beam bending is linearly dependent on the Y-coordinate, as shown in Equations (13) and (14), so that the stress changes linearly in the direction of the beam thickness. This is taken into account in the failure model through numerical integration of the resultant stresses and viscous forces along the beam

thickness. The resultant stresses and viscous forces are defined in Equations (15) and (16). They are integrated applying the Gauss quadrature in seven designated integration points after crack initiation (see Figure 17). After this, the cohesive crack model is applied on each integration point and the stress in the cohesive zone can be calculated from Equation (29) or (30) depending on the loading case. The true crack advances when the crack opening displacement at an integration point reaches its critical value δ_f and loses its load-carrying capacity. The formation of a crack changes the cross-section of the beam and thus the position of the neutral axis changes as the crack propagates. Therefore, a new position for the neutral axis is calculated (Paavilainen *et al.*, 2009).

3.3 Ice Block Interaction

As described above, the ice sheet consists of discrete elements joined together by Timoshenko beam elements (see Figure 16). As the ice fails, it breaks into smaller fragments that interact with each other and with the structure. The discrete element method (DEM) is used to solve forces due to these interactions.

The forces due to interactions between the ice blocks are solved using contact detection and contact force calculation algorithms. The purpose of a contact detection algorithm is to search for discrete elements close to, and potentially contacting, each other. The algorithm used in the current model is based on the so-called *no binary search* (NBS) algorithm developed by Munjiza and Andrews (1998). The contact detection with NBS is independent of the shape of the interacting particles, which significantly reduces the computational cost. Although the algorithm is used to avoid calculating the exact contact geometry, the operations related to the contact calculations form the single most time-intensive task the model has to perform.

When a contact is detected, the corresponding contact forces are calculated. As a part of the solution of the contact geometry, the normal $\mathbf{n}$ and tangential $\mathbf{t}$ direction vectors for the contact are solved. The total force acting between the interacting elements is then

$$\mathbf{f}_{tot} = \mathbf{f}_n + \mathbf{f}_t, \tag{31}$$

where $\mathbf{f}_n$ and $\mathbf{f}_t$ are the normal and tangential forces of the contact, respectively. The normal force is determined with an elastic-viscous-plastic model and the tangential force with an incremental Mohr-Coulomb model according to (Hopkins, 1992).

The elastic-viscous-plastic normal force model is based on the overlap of interacting elements (see Figure 20). The normal force is given by

$$\mathbf{f}_n = \min\{\mathbf{f}_{ne} + \mathbf{f}_{nv}, \mathbf{f}_p\}, \tag{32}$$

where $\mathbf{f}_{ne}$ is the elastic normal component, $\mathbf{f}_{nv}$ is the viscous normal component and $\mathbf{f}_p$ is the plastic limit force which sets the upper limit for $\mathbf{f}_n$. The elastic component $\mathbf{f}_{ne}$ is proportionate to the overlap area A according to

$$\mathbf{f}_{ne} = k_{ne} A \mathbf{n}, \tag{33}$$

where k_{ne} is the contact normal stiffness. The viscous component $\mathbf{f}_{nv}$ is proportionate to the rate of change of A in time according to

$$\mathbf{f}_{nv} = k_{nv}\dot{A}\mathbf{n}, \tag{34}$$

where $\dot{A}$ is the first time derivative of the overlap area and k_{nv} is the viscous damping coefficient. The plastic limit is defined by

$$\mathbf{f}_p = \sigma_p l_c \mathbf{n}, \tag{35}$$

where σ_p is the plastic limit, l_c is the breadth of the contact surface marked by the distance between the intersection points A and B in Figure 20. The plastic limit introduces inelasticity that accounts for local crushing of the blocks in contact. This means that crushing is only taken into account locally, occurring within the area of the contact geometry, not as a global failure mode. According to Equation (32), the material undergoes plastic failure if the sum of the elastic and viscous components exceeds the plastic limit force.

The elastic tangential force increases due to incremental slip between the contacting elements. It is calculated from

$$\mathbf{f}_{te,k+1} = \mathbf{f}_{te,k} - k_{te}(\mathbf{v}_c \cdot \mathbf{t})_{k+1/2}, \tag{36}$$

where the subscript k denotes the time step, k_{te} is the tangential elastic stiffness and $\mathbf{v}_c$ is the relative velocity of the contacting blocks at the point of contact, which is here defined to be the centroid of the overlap area. Thus the product $\mathbf{v}_c \cdot \mathbf{t}$ extracts the tangential component of the contact velocity. An approximation for the velocity at the half time step $k + 1/2$ is obtained as a part of the solution. The tangential

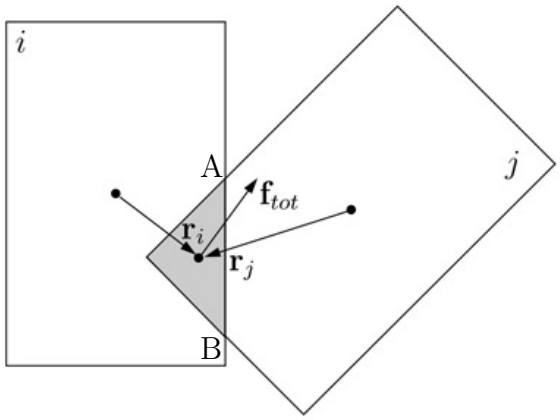

Figure 20: The contact search is based on overlapping elements. The overlapping area of elements i and j is shown in grey. The vectors $\mathbf{r}_i$ and $\mathbf{r}_j$ are direction vectors pointing from the centroid of an element to the centroid of the overlap area. The force vector $\mathbf{f}_{tot}$ is the sum of normal and tangential forces acting between the interacting elements (Paavilainen *et al.*, 2009).

force $\mathbf{f}_t$ is limited by a friction force that is proportional to $\mathbf{f}_n$. Thus the tangential force is determined according to Coulomb friction by

$$\mathbf{f}_t = \min\{\mathbf{f}_{te}, \mu\mathbf{f}_n\}, \tag{37}$$

where μ is the coefficient of friction between the contacting elements.

The moment of the contact force acting on each element is defined as

$$\mathbf{m} = \mathbf{r} \times \mathbf{f}_{tot}, \tag{38}$$

where the moment arm $\mathbf{r}$ is a direction vector pointing form the centroid of an element to the centroid of the area of overlap as illustrated in Figure 20.

3.4 External Forces

The external forces accounted for in the model are gravity, buoyancy and drag. The drag force is

$$\mathbf{f}_d = -\frac{\text{sign}(\mathbf{v})}{|\mathbf{v}|}\frac{1}{2}\rho_w l_p c_d \mathbf{v}^2, \tag{39}$$

where ρ_w is the water density, l_p is the projected length of the block in the direction of velocity, c_d is the drag coefficient and $\mathbf{v}$ is the velocity of an element. The buoyancy is calculated from

$$\mathbf{f}_b = A_{sm}\rho_w \mathbf{g}, \tag{40}$$

where A_{sm} is the submerged area of the element and $\mathbf{g}$ is the gravitational acceleration. The gravity is defined as

$$\mathbf{f}_g = A_b \rho_i \mathbf{g}, \tag{41}$$

where A_b is the area of the block and ρ_i is the density of ice. The total external force is calculated as a sum of the force components

$$\mathbf{f}_{ext} = \mathbf{f}_d + \mathbf{f}_b + \mathbf{f}_g. \tag{42}$$

3.5 Simulations of the Ice-Structure Interaction

As mentioned before, FEM-DEM simulations with the details described above were used to investigate the ice rubbling process against an inclined wall and the forces exerted on the structure during this process. The structure and the simulation set-up are illustrated in Figure 21. The figure shows the structure and the seabed in dark grey, the water in light grey, and the white and light grey rectangular pieces represent the ice sheet and the rubble. The structure extended 5 m above the water level. The top of the structure was a flat surface where the rubble could accumulate when overtopping occurred, as seen in Figure 21. The structure was assumed to be infinitely rigid. The depth of the water, the ice thickness and the inclination angle, were used as variables in the study.

There are some restrictions to the applicability of the FEM-DEM model when applied to the ice-structure interaction problem. First, the current model is two-dimensional and thus it omits certain three-dimensional phenomena such as the so-called clearing around narrow structures. For this reason, the model can only be applied to investigate ice rubbling against wide structures. Furthermore, the use of the model is limited to structures with sloping walls since it only includes a simplified model for ice crushing (Paavilainen *et al.*, 2011), which is a dominant failure mode in ice-structure interactions with vertical walls. According to the simplified model, compressive failure does not create new ice blocks or change their geometry.

A level, floating ice sheet was pushed against the structure at a constant velocity v_p from the left of the calculation domain as shown in Figure 21. The position of the left boundary is a function of the velocity and position of the boundary node, and thus the boundary was set 125 metres from the structure in order to minimise its effect on the solution. Furthermore, a viscous damping boundary condition was applied to approximate an infinitely long ice sheet that was fed to the calculation domain from the left over the duration of the simulation. The boundary condition was reduced from a semi-infinite beam model as explained in Paavilainen *et al.* (2011).

In total, 64 individual simulations were run to investigate the effect of the ice thickness to water depth ratio on the process and its outcome, such as the maximum forces and the pile geometry. The most important parameters of the simulations are listed in Table 1, and they were chosen according to the work of Paavilainen *et al.* (2011) and a review by Timco and Weeks (2010). The ice thickness h varied from 0.5 m to 1.25 m and the water depth D was investigated in a range from 2.5 m to 15 m. The effect of the steepness of the wall was also studied with two values of the inclination angle, $\alpha = 45°$ and $\alpha = 60°$. For simplicity, the friction coefficient between the ice and the structure had the same value as the friction coefficient between the ice and the seabed. The normal contact stiffness k_{ne} was always the same as the effective modulus E and the value of the tangential contact stiffness k_{te} was chosen after the value of the shear modulus G. The initial velocity of the ice

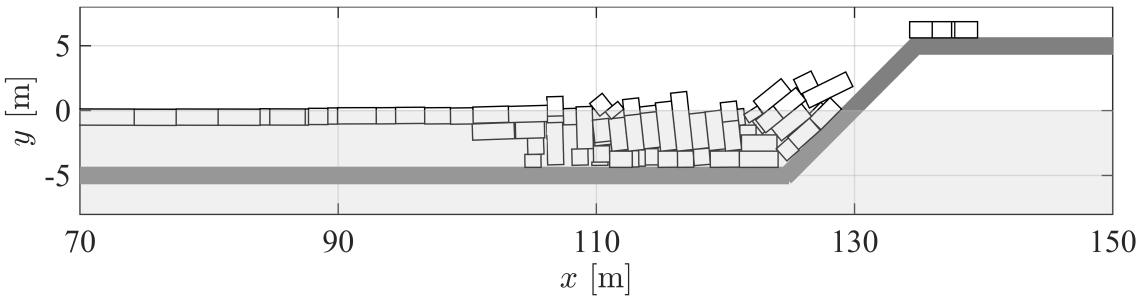

Figure 21: Ice rubbling against a structure was simulated in shallow water. An intact ice sheet is pushed towards the structure from the left and it breaks into blocks of various sizes. The structure and the seabed are shown in dark grey and the water in light grey. The figure does not show the whole simulation domain.

Table 1: The main parameters used in the simulations. The structure height is measured from the waterline.

Parameter	Symbol	Unit	Value
Ice thickness	h	m	$0.5, 1.25$
Effective modulus	E	GPa	3.98...4.02
Poisson's ratio	ν	-	0.3
Ice density	ρ_i	kgm^{-3}	900
Tensile strength	σ_f	kPa	600
Shear strength	τ_f	kPa	600
Fracture energy	G_f	Jm^{-2}	12
Water density	ρ_w	kgm^{-3}	1010
Water depth	D	m	2.5...15
Ice-ice friction coefficient	μ_{ii}	-	0.3
Ice-structure friction coefficient	μ_{is}	-	0.1
Contact normal stiffness	k_{ne}	GPa	3.98...4.02
Plastic limit	σ_p	MPa	2.0
Inclination angle	α	$^\circ$	45, 60
Structure height	h_s	m	5
Time step	Δt	s	$2.0 \cdot 10^{-5}$
Ice sheet velocity	v_p	ms^{-1}	0.05
Element length	L_0	m	0.25
Drag coefficient	d_c	-	2.0

sheet was $v = 0$ m/s and it accelerated linearly to the constant velocity v_p during a time interval $t = [0, 1]$ s. The duration of each simulation was 5000 s corresponding to 250 m of ice being pushed against the structure. Similarly to Paavilainen *et al.* (2011), the element length was chosen to be $L_0 = 0.25$ m and the time step used in the simulations was $\Delta t = 2.0 \cdot 10^{-5}$ s. The value of the internal damping coefficient was proportional to the critical damping of a damped spring-mass system $2\sqrt{mE}$, where m is the mass of a discrete element.

According to Paavilainen *et al.* (2011), the model is sensitive to certain parameters, such as the effective modulus. Thus slightly altering the effective modulus, the solution follows a different path and the process details change. Therefore, the effective modulus was varied according to Table 1 to obtain data sets that could be used to study the general trends of the process. In total, five replicate simulations with ice thickness $h = 1.25$ m and three replicate simulations with ice thickness $h = 0.5$ m were run at each water depth. The data of each simulation was recorded at an output rate 0.08 s. This data included forces on the structure walls and on the seabed and contact data between the individual blocks and the structure.

4 Results and Analysis

This section presents the results of the simulations. The results described here include examining the load response and maximum loads of the simulations, and discussing the effects of grounding on the observed phenomena. Furthermore, the rubble pile geometry and its deformation patterns related to load peaks and overtopping are analysed. Finally, the load distribution in the rubble pile is investigated by studying the so-called force chains.

4.1 Load Response

Figure 22 illustrates the original force record of a simulation in red. In order to remove the peaks due to sudden impacts, the data was filtered using a 3-point median filter as done by Paavilainen *et al.* (2011). For comparison, the filtered data is shown in black in the figure. All the results presented in this chapter are based on the filtered data.

4.1.1 Load Records

Figure 23 gives typical force records of a simulation as a function of the length of ice pushed against the structure L. Figure 23a shows the horizontal force S_H exerted on the structure and Figures 23b and 23c show, respectively, the horizontal and vertical forces, B_H and B_V, acting on the seabed. The figures show the recordings of the simulations with water depth $D = 5$ m and with two ice thicknesses, $h = 1.25$ m ($D/h = 4$) in black and $h = 0.5$ m ($D/h = 10$) in grey. The data is recorded from a simulation with the wall angle $\alpha = 45°$. When the water depth was 10 m or more, the rubble was only occasionally in contact with the seabed or it was not grounded at all. The force records in Figures 23b and 23c represent cases with $D < 10$ m when rubble was grounded.

Figure 23a shows how S_H follows a pattern where the force gradually grows and then abruptly drops repeatedly over the duration of the simulation. In this work, this type of period in the load record between a load increase with an overall growing

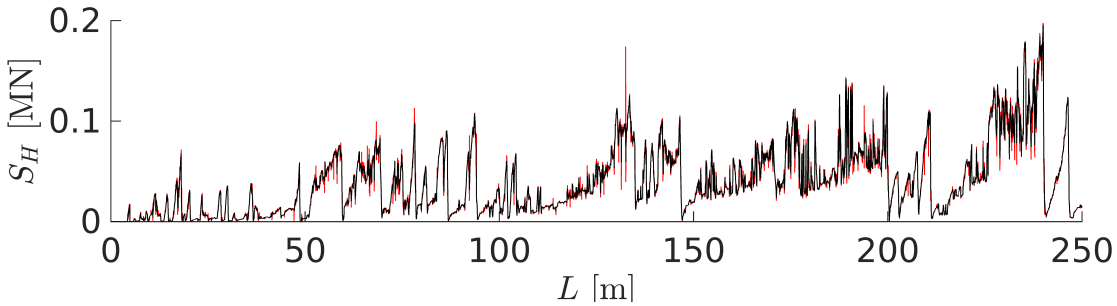

Figure 22: The horizontal force on the structure S_H as a function of the length of ice pushed against the structure L. The data was filtered using a 3-point median filter to remove peaks due to sudden impacts. The raw data is shown in red and the filtered data is shown in black.

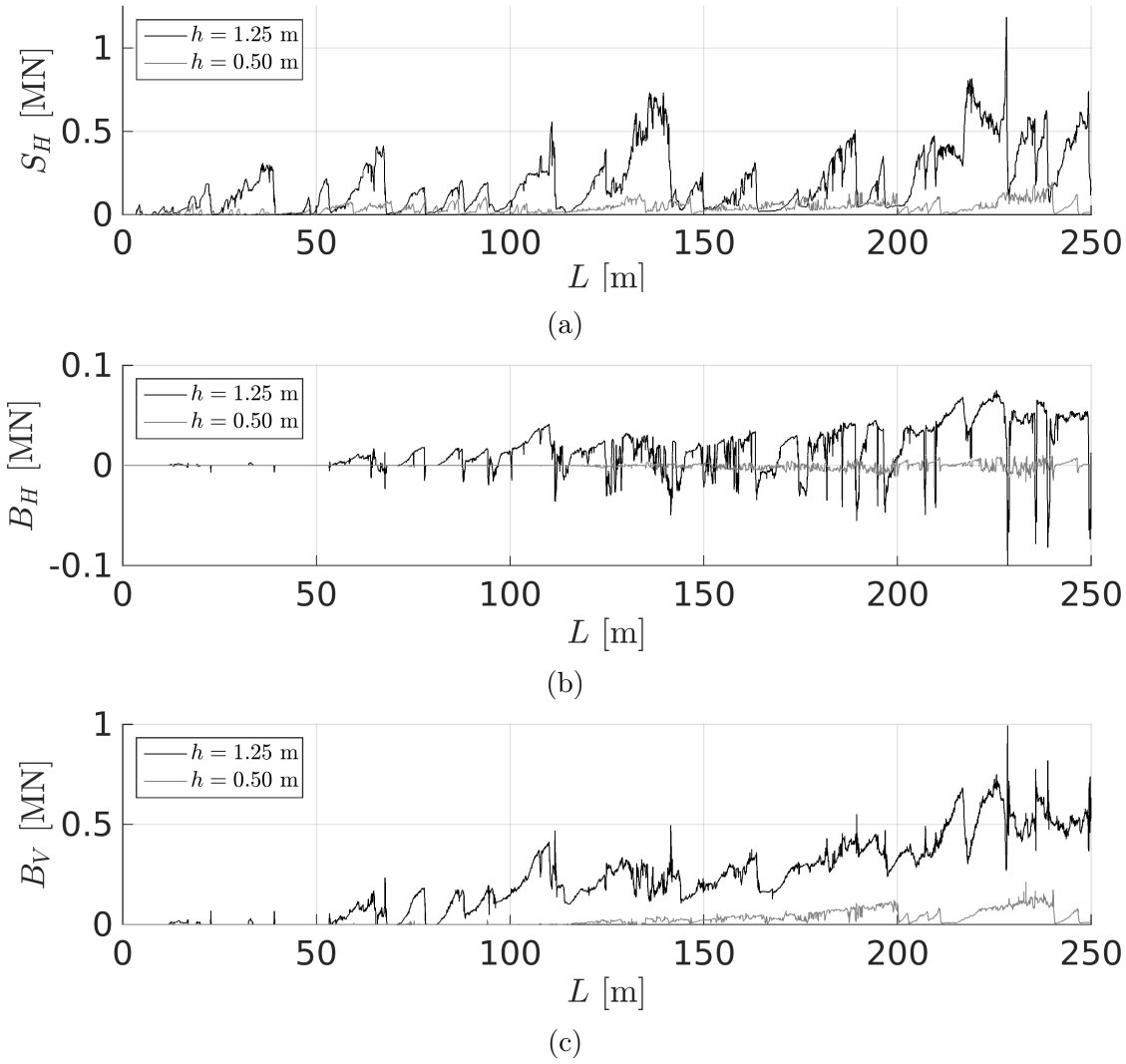

Figure 23: Typical load history of the simulations as a function of the length of ice pushed against the structure L: (a) horizontal force S_H on the inclined part of the structure, (b) horizontal force B_H on the seabed and (c) vertical force B_V on the seabed. The figures show data obtained from simulations with water depth $D = 5$ m, inclination angle $\alpha = 45°$ and ice thicknesses $h = 1.25$ m (in black) and $h = 0.5$ m (in grey). The positive direction of the forces is towards the structure for horizontal forces and downwards for the vertical force.

trend and a major load drop is called a load event. The duration of these so-called peak load events was typically equivalent to 5 to 15 m of ice being pushed against the structure. Comparison of the load records with the two different ice thicknesses in Figure 23a shows that the load levels with the thin $h = 0.5$ m ice were only about one fifth of the average load level exerted on the structure by the thick $h = 1.25$ m ice. However, similar successive load events were observed with both ice thicknesses. To illustrate this further, a re-scaled load record of the simulation with $h = 0.5$ m is given in Figure 24.

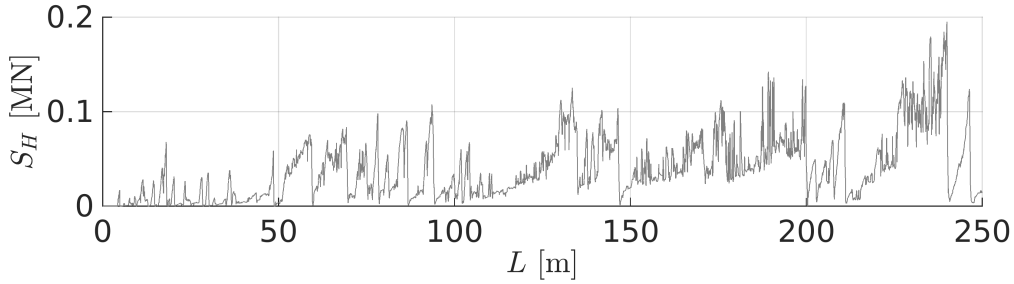

Figure 24: A re-scaled load record of the simulation with the ice thickness $h = 0.5$ m shows that successive peak loads are observed on the structure wall when the thin ice interacts with the structure. S_H is the horizontal force on the structure and L is the length of ice pushed against the structure.

The sign of the horizontal bottom force B_H in Figure 23b is changing due to the changing direction of motion of the ice blocks interacting with the seabed. The values of B_H are, however, predominantly positive, which implies that the ice is moving towards the structure most of the time and the seabed resists this motion. The positive sign of the force acting on the seabed indicates an equivalent frictional force with an opposite sign acting on the ice blocks that are in contact with the seabed.

The magnitude of the load B_H was approximately 10 to 15 % of the loads on the structure S_H at the instants of load peaks, which suggests that the seabed is only carrying a minor portion of the load. Furthermore, comparison between S_H in Figure 23a and B_H in Figure 23b shows that load drops on the structure wall often coincide with load drops on the seabed, which suggests that the load events on the wall correlate with load events on the seabed.

The absolute value of the horizontal bottom force B_H and the vertical bottom force B_V typically had an increasing trend as shown by Figures 23b and 23c. This increase in the magnitude of the seabed force components is caused by the increasing amount of grounded ice rubble in front of the structure as more ice is being pushed against it. The increasing weight of the ice rubble causes an increase in the supporting force of the seabed. This, in turn, is linked to the horizontal force B_H through Coulomb friction and thus the forces B_V and B_H grow simultaneously.

The effects of grounding were more pronounced in the shallowest water, as would be expected. This is shown by Figures 25a and 25b, which illustrate typical load records of the simulations with $D = 2.5$ m at wall angles $\alpha = 60°$ and $\alpha = 45°$, respectively. The ice thickness in these simulations was $h = 1.25$ m and the ratio $D/h = 2$. It can be seen that the load events in the shallowest water are more frequent when compared with the load events of the simulations with $D = 5$ m in Figure 23a. Furthermore, the front slope of various load peaks is now steep and the load drop is more gradual. This is contrary to the gradual load build-up and the abrupt load drops in deeper water. Comparison of Figures 25a and 25b reveals that the load peaks at $\alpha = 60°$ were significantly higher than at $\alpha = 45°$. For all the simulations, the general trend was that the highest load peaks typically occurred

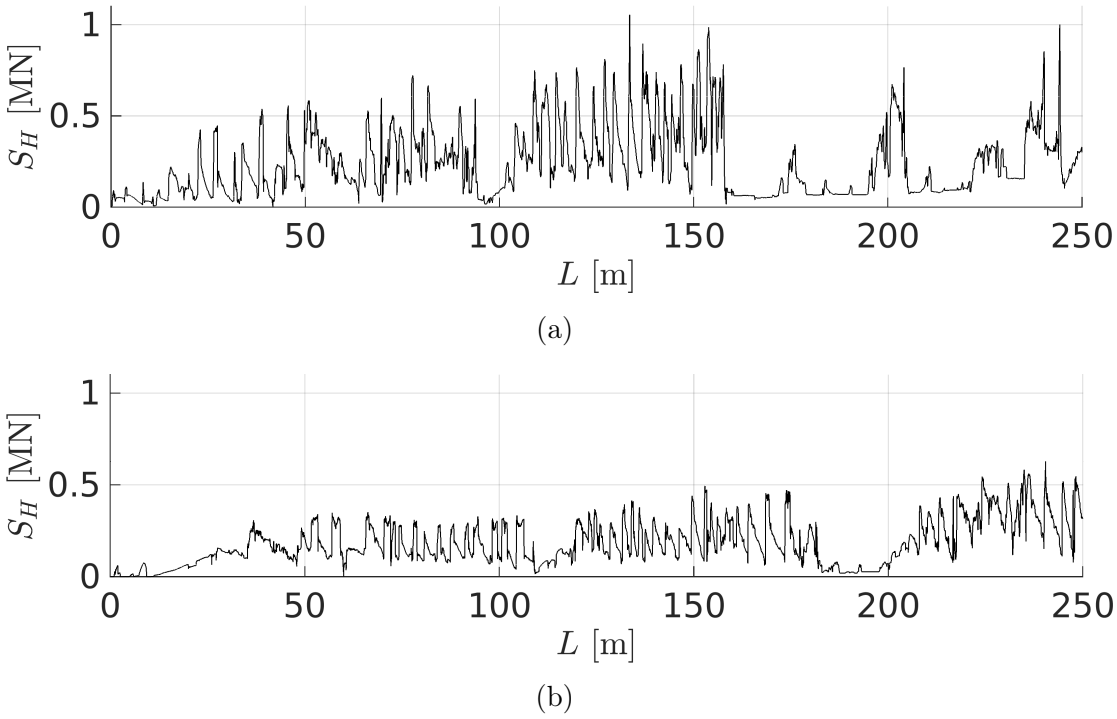

Figure 25: Typical horizontal wall force from a simulation in the shallowest water ($D = 2.5$ m) at two different wall angles (a) $\alpha = 60°$ and (b) $\alpha = 45°$. The force records are obtained with the ice thickness $h = 1.25$ m.

with the 60° wall. The magnitude of the forces on the seabed was similar at both wall angles, except when $D = 2.5$ m and $h = 1.25$ m as the forces B_H and B_V at $\alpha = 60°$ were approximately double the forces at $\alpha = 45°$.

The frequent load peaks with a sudden increase and gradual load drop formed a zigzag-like pattern that was found to be related to intense overtopping. During this zigzagging, several sharp short-term load peaks with approximately the same peak value occur successively. Examples of this are seen in Figure 25a when $L \in$ [110 m, 160 m] and in Figure 25b when $L \in$ [120 m, 183 m]. The duration of the peaks was typically equivalent to 2 m of ice being pushed against the structure. The zigzagging in Figure 25a ends with a sudden load drop at $L = 160$ m, followed by a close-to-constant load with marginal load peaks when $L \in$ [160 m, 195 m]. Similar behaviour can be observed in Figure 25b.

4.1.2 Peak Loads

The design of Arctic offshore structures is usually based on the maximum ice load applied on the structure. Thus the maximum wall forces S_H^m at each wall angle and ice thickness were averaged and plotted as a function of the water depth. The maximum forces were extracted at two stages of the simulation: (1) at the initial stage ($L < 50$ m) when no large rubble pile has formed and the ice is mostly failing against the structure, and (2) at the later stage (150 m $\leq L \leq$250 m) when a large

rubble pile has formed and the ice is likely to fail against it. The maximum force of the whole simulation was also extracted and averaged. The maximum forces and their averages at different stages of the simulation are shown in Figure 26. Figure 26a shows the peak loads from the initial part of the simulations, while Figure 26b gives the peak loads from the final stage of the simulation and Figure 26c from the whole simulation. The relative scatter of the results was rather high and the variation in the peak load values obtained with the thicker ice appeared to be larger than in the values obtained with the thin ice, as suggested also by Paavilainen and Tuhkuri (2012).

The water depth seems to have a strong effect on the magnitude of the maximum loads. As the water depth decreases, the S_H^m values increase as shown by Figure 26. This was most clearly observed with the thicker ice $h = 1.25$ m towards the end of the simulation (see Figure 26b). For instance, if the S_H^m value with $D = 10$ m and $\alpha = 45°$ is chosen as a reference point, the S_H^m value with $D = 5$ m is approximately 20 % higher than that and the S_H^m value with $D = 15$ m 40 % smaller. It should be noted that due to one outlier with the wall angle $\alpha = 60°$ at the water depth $D = 5$ m, the average raises to a higher value than at the water depth $D = 2.5$ m. However, with the thinner $h = 0.5$ m ice the simulations at each water depth resulted in approximately equal peak load values. An exception to this are the simulations with $D = 2.5$ m which led to slightly higher maximum forces (see Figure 26b). Furthermore, Figure 26 shows that the ice thickness h strongly affects S_H^m values, as expected based on the results in Paavilainen and Tuhkuri (2012) and Ranta *et al.* (2014). The simulations with $h = 1.25$ m gave three to four times higher peak loads than the simulations with $h = 0.5$ m.

The results appear to be more affected by the ice thickness h than the ratio D/h since the increase of the S_H^m values in shallow water is more rapid with $h = 1.25$ m than with $h = 0.5$ m. Furthermore, the results obtained with obtained with D/h ratios related to $h = 0.5$ m were predominantly lower than the results obtained with D/h ratios related to $h = 1.25$ m. Thus the maximum loads seem to be determined by the ice thickness h rather than the ratio D/h. Paavilainen and Tuhkuri (2012) and Ranta *et al.* (2014) also found that the ice thickness is the governing variable in the formation of maximum loads.

When the rubble was grounded, the angle α affected the maximum loads throughout the simulations. Comparison of Figures 26a and 26b reveals that the S_H^m values at different wall angles diverge as the simulation proceeds when the rubble is grounded and approach each other when the rubble is not grounded. The effect becomes more pronounced with $h = 1.25$ m when comparing the S_H^m values with $D = 5$ m and $D = 15$ m. The observation suggests that the effect of the inclination angle does not vanish towards the end of the simulation in shallow water but it affects the process throughout the simulation.

4.1.3 Grounding and Its Effects

The maximum depth of the rubble pile in shallow water is limited by the seabed. When the rubble pile reaches the maximum water depth, the rubble interacts with

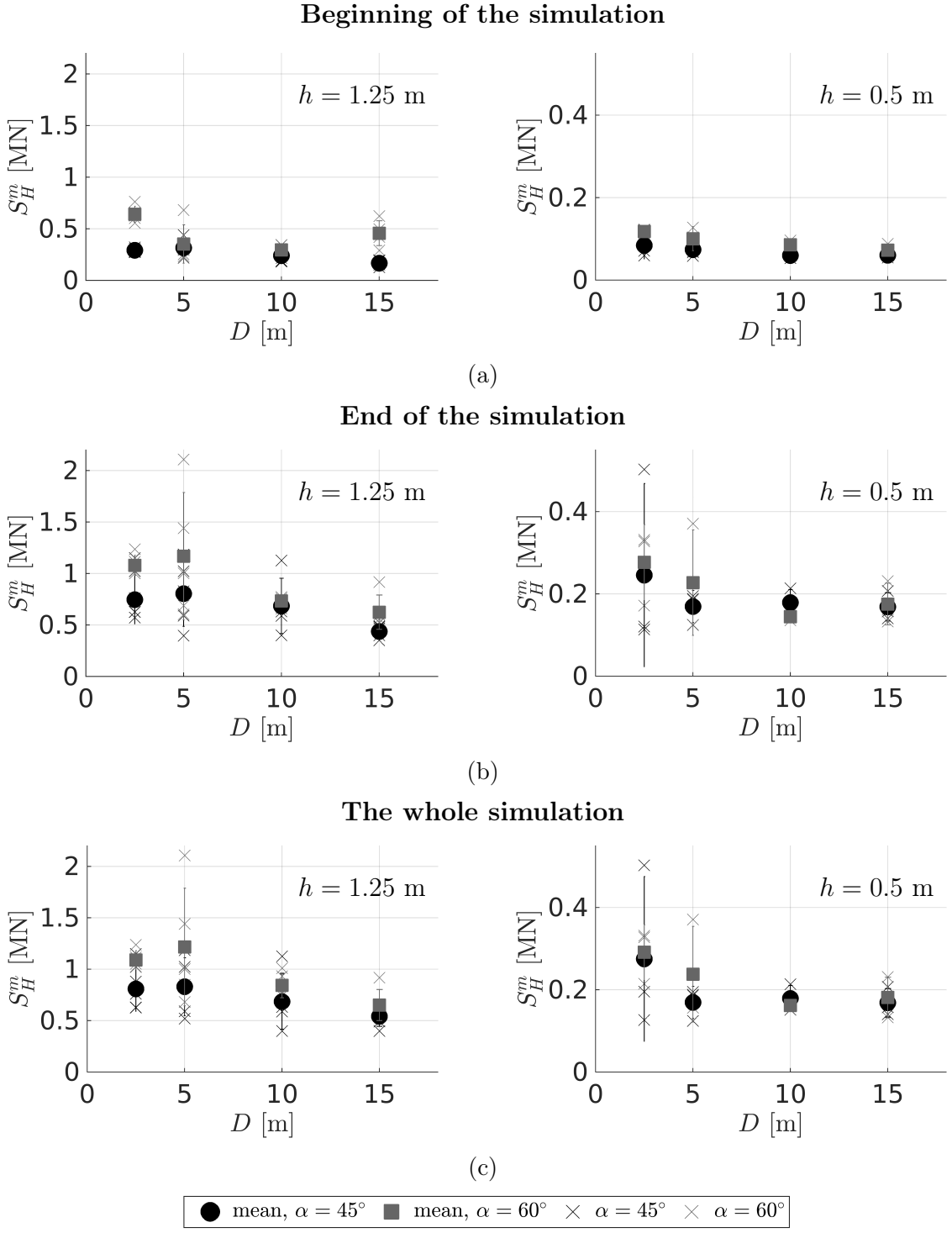

Figure 26: Maximum horizontal load S_H^m values on the inclined part of the structure (a) at the initial stage of the simulation, (b) at the final stage of the simulation and (c) during the whole simulation. The figures show the results of the individual simulations, their average and the standard deviation with different wall angles. The results from the simulations with ice thickness $h = 1.25$ m are on the left and the results with the ice thickness $h = 0.5$ m on the right. It should be noted that the scale of the plots is not constant between the plots on the left and on the right.

the seabed. The effects of rubble grounding in the simulations were first studied examining the force B_V on the seabed as it correlates with the mass of ice in contact with the seabed. As was illustrated by Figure 23c above, the B_V records showed fluctuations and sudden impacts. To eliminate their effect, rubble grounding was estimated calculating the average of the vertical force on the seabed, $\bar{B}_V$, over the duration of the simulation. This was applicable, since B_V showed an increasing trend when grounding had occurred and the rubble stayed in contact with the seabed. Similarly, the average of the absolute value of the horizontal force on the seabed $|\bar{B_H}|$ was calculated to study the effect of grounding. The absolute value of B_H was used because B_H changes its sign during the simulation as described above, and thus averaging it without the absolute value would yield values close to zero.

The results on B_V indicate that the amount of grounded rubble decreased rapidly as the water depth increased. This is shown by Figure 27 which gives B_V values from all the simulations, their average and the standard deviation of the results as a function of water depth D. When $D = 10$ m or more, hardly any or only occasional grounding occurred regardless of the ice thickness. The results with less grounded rubble with each D were from simulations with $h = 0.5$ m, as can be verified by comparing the load records of the two different ice thicknesses in Figure 23c.

The simulation results suggest an increasing trend with a decreasing D/h ratio even if the scatter is quite large. The load on the seabed gets higher values as the force on the wall increases, which further supports the observation that the grounded rubble increases the loads on the wall instead of decreasing them. This is shown by Figure 28a, which gives the S_H^m values plotted against the average vertical force on the seabed $\bar{B}_V$. The results were obtained with the wall angle $\alpha = 60°$ and only D/h ratios with clearly grounded rubble were considered ($D = 2.5$ m and $D = 5$ m). Similar observation can be made from Figure 28b which presents the maximum horizontal force on the structure wall S_H^m plotted against $|\bar{B_H}|$. Therefore, it appears that rubble grounding is related to an increase in S_H^m.

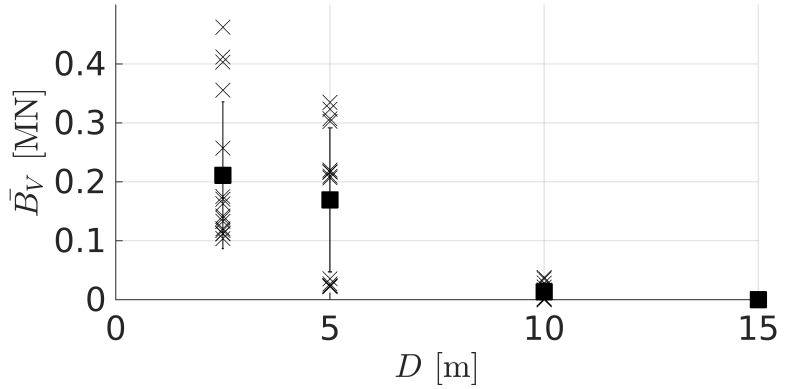

Figure 27: Average vertical force on the seabed $\bar{B}_V$ as a function of water depth D was used as an indicator for rubble grounding. The rubble was grounded at $D < 10$ m regardless of the ice thickness. The data from all the simulations was used to obtain the estimate for ground at each D.

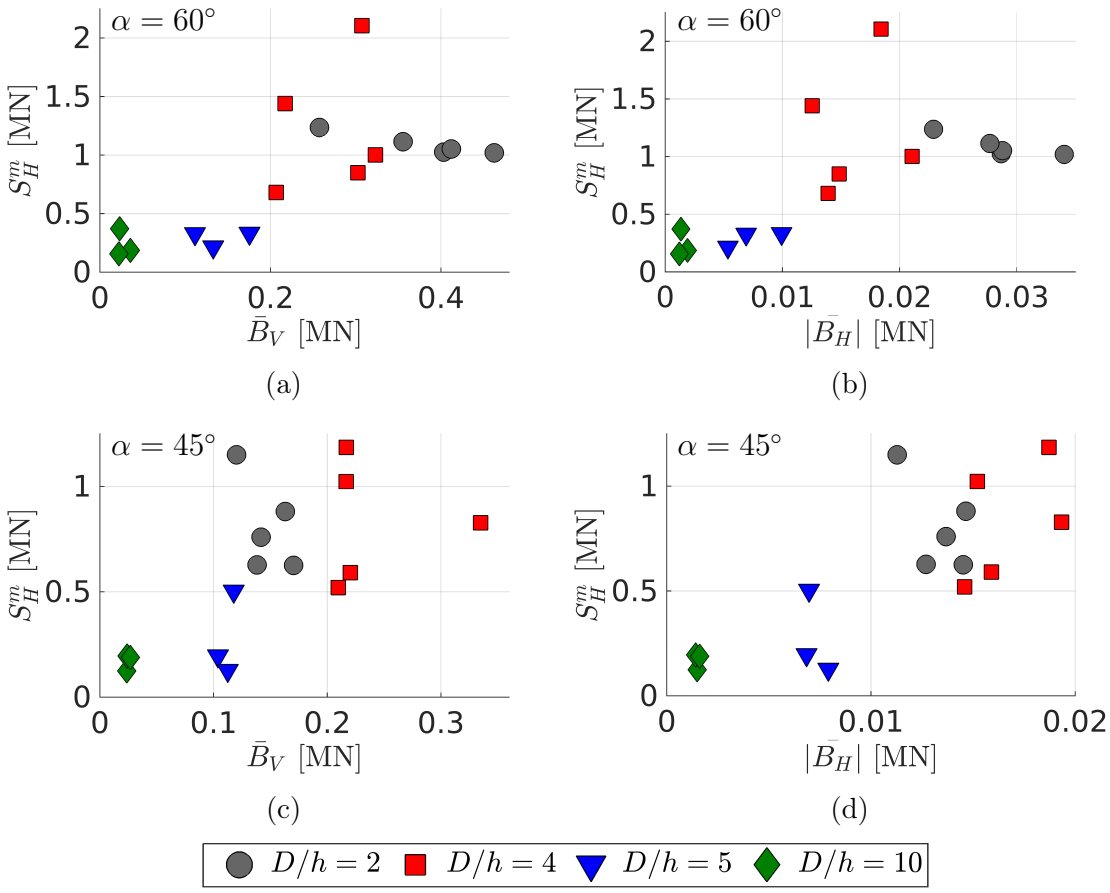

Figure 28: An increasing trend can be observed when the maximum horizontal force on the wall S_H^m is plotted against (a) & (c) the average vertical force on the seabed $\bar{B}_V$ and (b) & (d) the average of the absolute value of the horizontal force on the seabed $|\bar{B}_H|$. The figures (a) and (b) are obtained with the wall angle $\alpha = 60°$ and the figures (c) and (d) with the wall angle $\alpha = 45°$.

The ratio $D/h = 2$ yielded lower forces on the seabed than the ratio $D/h = 4$ when $\alpha = 45°$, which is contrary to the results with $\alpha = 60°$. This is shown by Figures 28c and 28d which represent the S_H^m values plotted against the forces $\bar{B}_V$ and $|\bar{B}_H|$, respectively, with the wall angle $\alpha = 45°$. It is suggested that the low bottom forces at $D/h = 2$ are caused by intense overtopping occurring at that ratio, as will be discussed in Section 4.2.4. The amount of ice in the simulations is constant and thus, when a large volume of ice is pushed on top of the structure, less rubble is grounded reducing the force on the seabed.

4.2 Deformation Patterns and Overtopping

During the simulations, several events occurred that changed the rubble pile configuration. The changes in the pile geometry were often related to concurrent events on the load records, and two main types of deformation patterns related to different

load events were observed: ride-up events and events related to intense overtopping. Furthermore, both these deformation processes were strongly affected by the seabed. This chapter describes how the rubble pile deformed during the ride-up events and overtopping, and how the pile geometry changed over the whole duration of the simulation. Finally, the effect of the simulation variables on the amount of overtopped ice is discussed.

4.2.1 Rubble Pile Deformation in a Ride-Up Event

The load events, such as the one in Figure 23a, were often related to so-called ride-up events where the advancing ice pushes the rubble along the structure until the rubble pile suddenly collapses. The rubble behaviour during a load event is illustrated in Figures 29 and 30. The figures show a close-up of the $S_H - L$ record related to a load event with three marked instants corresponding to different stages of the load event: instant (1) marks the onset of the load event, instant (2) is the peak force during the load event and (3) is an instant immediately after the load drop. Furthermore, the snapshots in the figures show the configuration of the rubble pile at instants (1)-(3) and the average velocities $\bar{v}_x$ and $\bar{v}_y$ between these instants. The average velocity at instant (1) was obtained from an interval equivalent of 0.6 m of ice being pushed against the structure before the onset of the load event. It should be noted that the scale of the plots is not kept constant between the figures due to large variance in the velocity values between the instants.

The main features of the instants (1)-(3) of the ride-up event and the corresponding rubble configurations in Figures 29 and 30 are as follows:

(1) The rubble pile is at rest in front of the structure before the load starts to increase. The largest velocities are at the left edge of the pile where the intact ice is being pushed towards the structure. In addition, the pile extends far from the structure along the seabed and the pile does not rise largely above the water level in the vertical direction.

(2) As more ice is pushed against the structure, the rubble pile starts to move and the force on the structure wall starts to increase. During the gradual increase of the load, all the ice blocks are in motion. The pile moves towards the structure and, upon reaching it, starts to ride up its wall. When the peak of the load event is reached, a large amount of rubble has been pushed against the structure and the left edge of the pile has moved closer to the structure.

(3) After reaching the peak value at (2), the rubble pile abruptly collapses, which is seen as a sudden load drop in the load history. During this load drop, the rubble pile undergoes major changes in its configuration. This is shown by the large negative velocities in the snapshots indicating that the ice blocks close to the structure have rapidly moved down and the whole pile has slid away from the structure along the seabed. Furthermore, overtopping has occurred during the load event, as shown by the increased volume of ice on top of the structure.

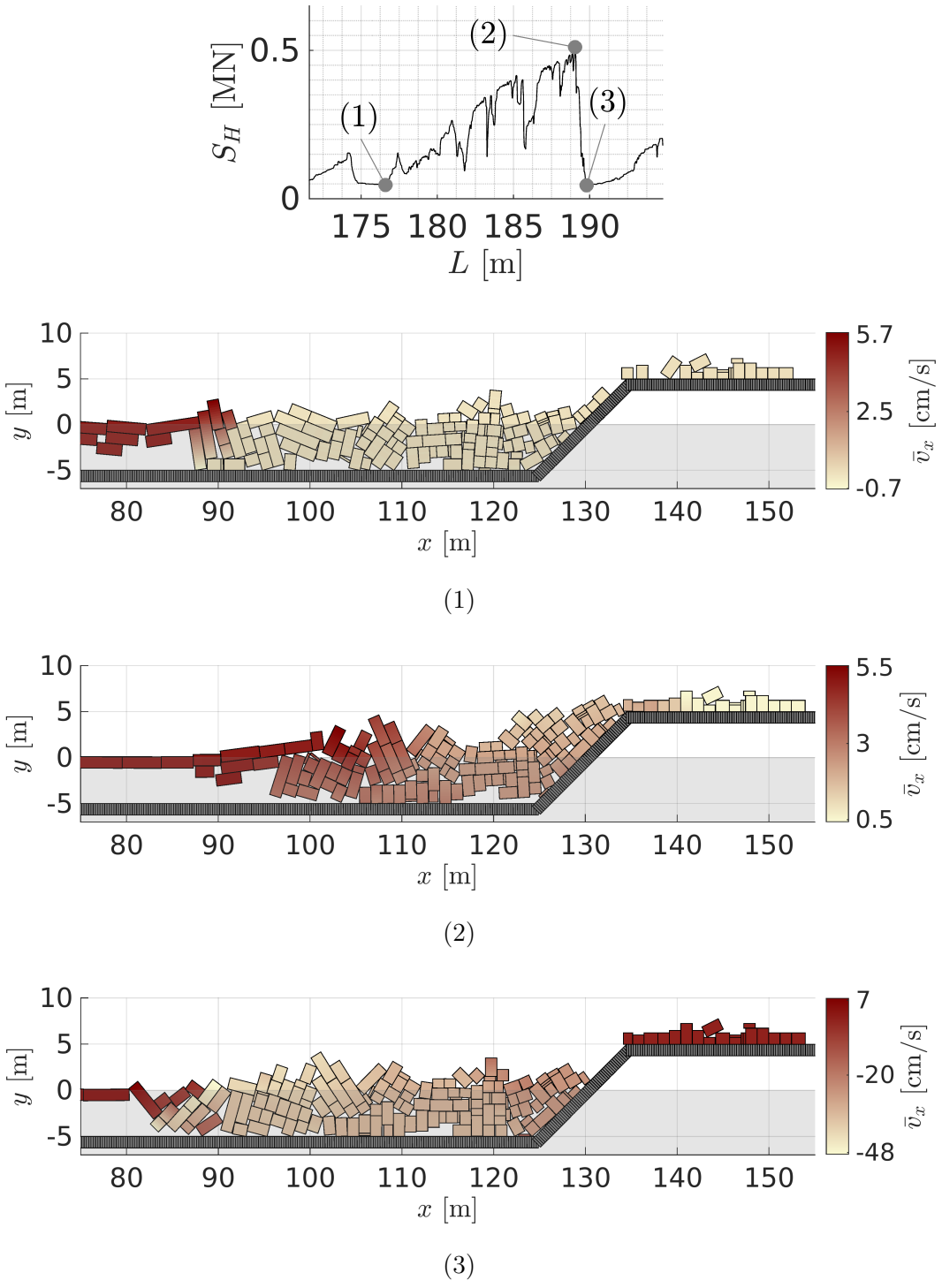

Figure 29: A close-up of a $S_H - L$ record showing a load event and snapshots illustrating the configuration of the rubble pile during the load event: (1) at the onset of the load event, (2) at the peak and (3) after the load drop as illustrated in the load record. The colours illustrate the average horizontal velocities $\bar{v}_x$ between the instants. The velocity in (1) was recorded during an interval equivalent to 0.6 m of ice being pushed against the structure before the onset of the load event.

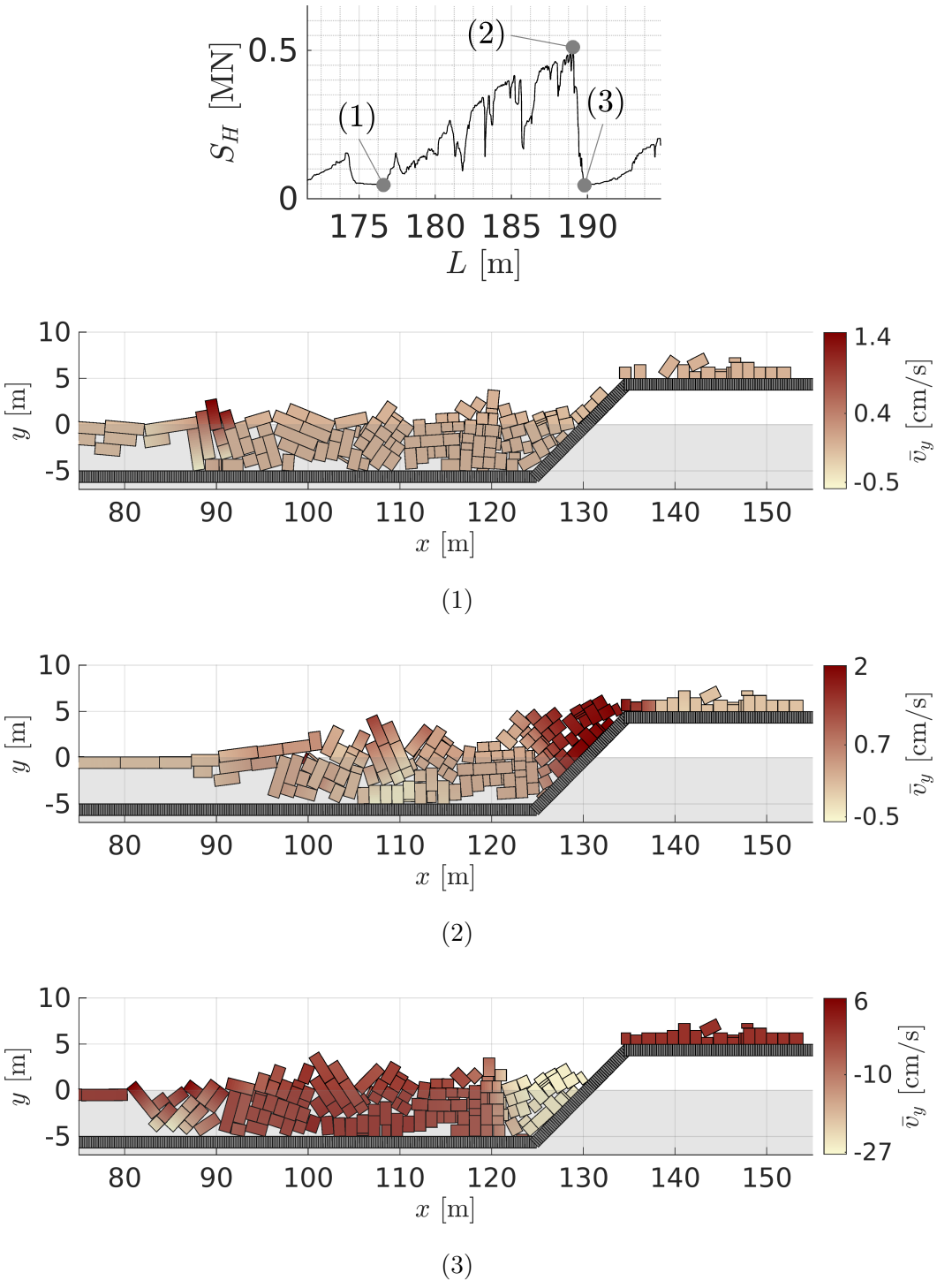

Figure 30: A close-up of a $S_H - L$ record showing a load event and snapshots illustrating the configuration of the rubble pile during the load event: (1) at the onset of the load event, (2) at the peak and (3) after the load drop as illustrated in the load record. The colours illustrate the average horizontal velocities $\bar{v}_y$ between the instants. The velocity in (1) was recorded during an interval equivalent to 0.6 m of ice being pushed against the structure before the onset of the load event.

As seen from the sequence of snapshots in Fugures 29 and 30, the accumulating rubble forms an unstable buffer zone in front of the structure in shallow water. During a ride-up event, the buffer becomes mobilised and reaches its minimum size at the peak of the load event. Thus the buffer does not protect the structure from loads, unlike predicted by Timco and Wright (1999) and the ISO standard (International Organization for Standardization, 2008).

4.2.2 Rubble Pile Deformation During Overtopping

In the shallowest water, the nature of the ice-structure interaction process changed and became characterised by intense overtopping rather than ride-up-events. Intense overtopping in shallow water generally occurred in two alternative ways: either the ice advanced to the structure along the seabed or on top of a grounded rubble pile. As mentioned in Section 4.1.1, the zigzag-like pattern in the load record was observed when intense overtopping occurred with $D = 2.5$ m. During this zigzagging, which consisted of several load events with a sudden load increase and a gradual load drop, the ice advanced to the structure along the seabed.

The rubble behaviour during intense overtopping is illustrated in Figures 31-34. Figure 31 shows a load sequence of a $S_H - L$ record which is divided into six instants: at (1) the load event is yet to start, at (2) the load suddenly increases towards the peak at (3) and then starts gradually decreasing to (4). Instant (5) indicates the peak of the last load event in the sequence and instant (6) indicates the close-to-constant load on the wall some time after the load sequence. Figure 32 shows the rubble pile configurations and average speeds of the ice blocks $\bar{v}_{tot}$ at instants (1)-(4). The average speed at (1) was obtained during an interval equivalent to 0.35 m of ice being pushed against the structure. Figures 33 and 34 show the piles and speeds at instants (5) and (6), respectively. The scale of the plots is not constant between the figures due to large variance in the speeds between the instants.

The main features of the instants (1)-(4) of an overtopping event in Figure 31 and the corresponding rubble configurations in the snapshots in Figure 32 are as follows:

(1) Most of the rubble is at rest and the ice advances to the structure along the seabed. A gap remains between the advancing ice and the structure close to the seabed.

(2) The ice advances to the structure and the rubble is in contact with the structure on the whole length of the wall. The ice has just reached the wall but the force on the wall remains low.

(3) As more ice is pushed against the structure, the ice gets compressed against the wall. The movement of the ice is constrained when it confronts the angle between the structure and the seabed, and a sudden load increase is observed. A small gap has again formed between the rubble and the seabed close to the structure but the rest of the pile has remained immobile.

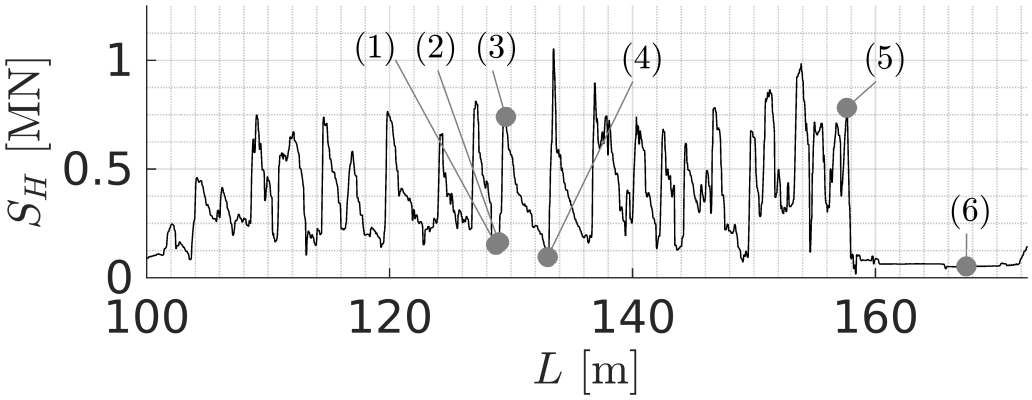

Figure 31: A close-up of the $S_H - L$ record shows a sequence of sharp load peaks with a sudden load increase and a gradual drop. Instant (1) marks the situation before the onset of the peak, instant (2) marks the onset of the peak, instant (3) is the peak of the load event and instant (4) is the end of the load event. Instant (5) is the peak of the last load event of the sequence and instant (6) marks the constant load after the last load drop. The instants (1)-(4) correspond to the snapshots in Figures 32 and the instants (5) and (4) to the snapshots in Figures 33 and 34.

(4) The compression decreases gradually as the ice turns to ride up along the structure. The advancing ice pushes the blocks up along the wall and on top of the structure so that a large gap forms between the wall and the advancing rubble. The ice blocks that are at the corner of the structure and the seabed are just about to touch the wall and a new load event is about to begin.

Grounding clearly affected the deformation patterns of the rubble in the overtopping cases in shallow water. The ice primarily advanced to the structure so that it bent slightly downwards and moved towards the structure pressed against the seabed by the rubble on top of the moving ice, while the rest of the pile remained relatively stationary. When the ice reached the structure, it was forced to turn and move up along the wall forming several small ice blocks. This is shown by Figure 33, which shows $\bar{v}_{tot}$ of the rubble recorded over the whole zigzagging load sequence up to the instant (5) in Figure 31. The ice was constantly pushed on top of the structure during the load sequence and the process took place close to the structure. The left edge of the rubble pile did not extend far from the structure, its height increased and a large amount of rubble accumulated on top of the structure.

After the instant (5) of Figure 31, the pile collapses and a sudden load drop is observed in the load record. On the collapse, the pile extends far from the structure along the seabed and remains stationary as shown by Figure 34 which illustrates the rubble configuration and the average velocities $\bar{v}_x$ and $\bar{v}_y$ at instant (6) of Figure 31. The velocities in the figure are calculated on an interval that is equivalent to 9 m of ice pushed against the structure. The process has shifted from the structure to the left edge of the pile where the largest $\bar{v}_x$ values occur. Here the rubble has formed a protective buffer as the ice fails against the grounded rubble pile and the force

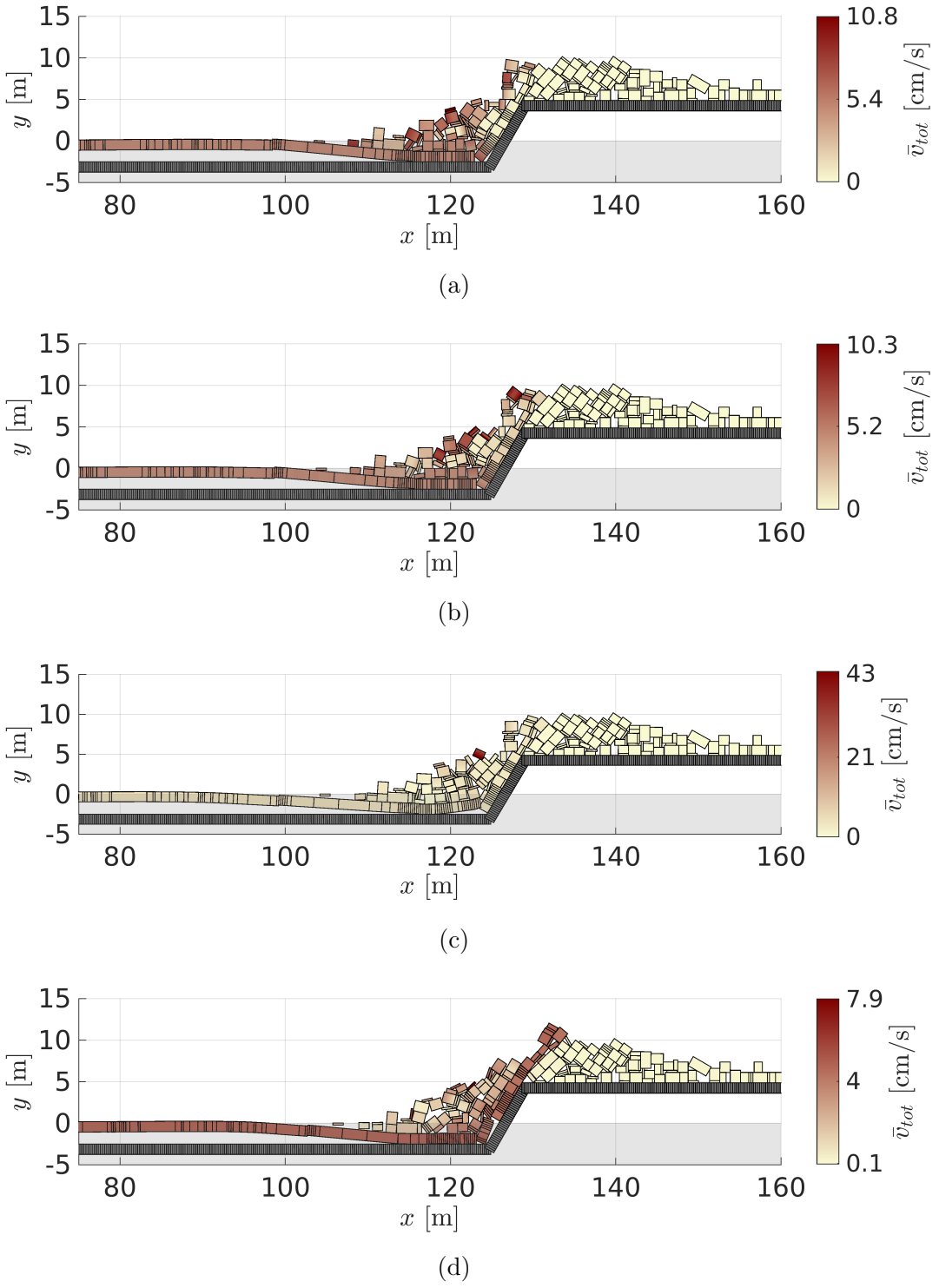

Figure 32: A load event during the zigzag-like pattern and overtopping. The numbers (1)-(4) refer to the instants indicated in Figure 31: at (1) the load event is yet to start, at (2) the load increases towards the peak at (3) and then gradually decreases to (4). The legend indicates the average speed $\bar{v}_{tot}$ between consecutive instants. For the instant (1), the average speed was obtained during an interval equivalent to 0.35 m of ice being pushed against the structure.

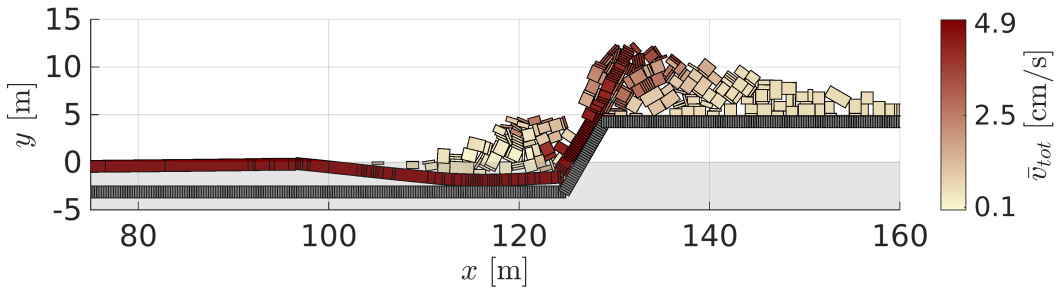

Figure 33: The rubble configuration before the major load drop at instant (5) in Figure 31 shows that the ice primarily advances to the structure and on top of it along the seabed while the rest of the pile remains stationary. The average speed $\bar{v}_{tot}$ is calculated over the duration of the whole load sequence in Figure 31.

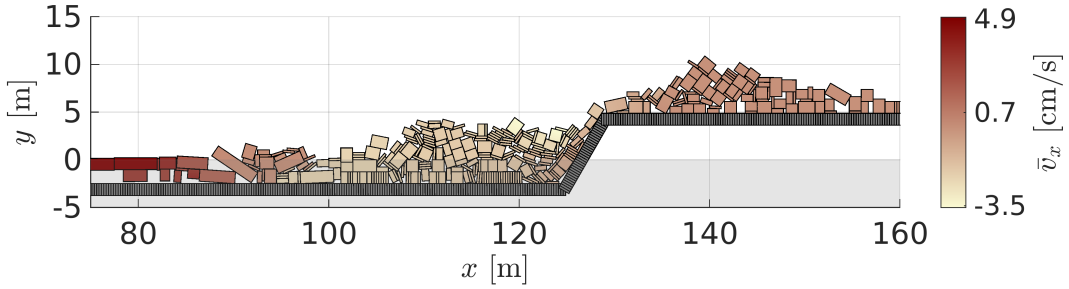

(a)

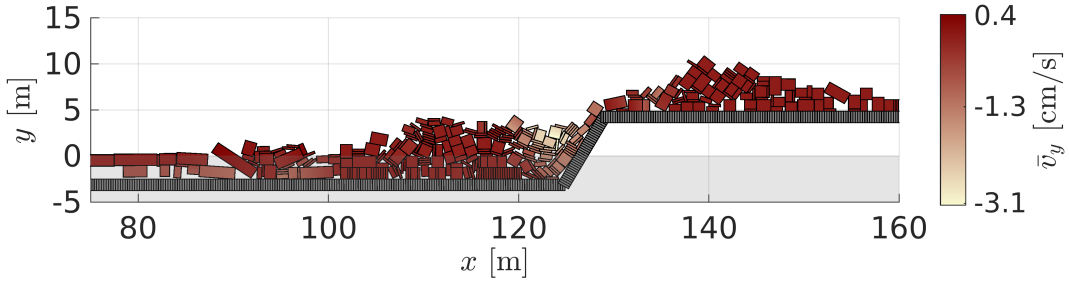

(b)

Figure 34: The rubble pile remains practically immobile and it has extended far from the structure when a constant load is observed in the load record at instant (6) in Figure 31, as seen from the small average velocities (a) $\bar{v}_x$ and (b) $\bar{v}_y$. The average velocities were calculated during an interval equivalent to 9 m of ice being pushed against the structure before the instant (6).

transmitted to the structure is mostly caused by the rubble resting against it. Thus the overall forces on the structure are low and have a constant value. This behaviour was generally observed in the shallowest water towards the end of the simulation when large rubble piles had accumulated in front of the structure. Furthermore, a protective buffer zone occasionally formed in the simulations with the thicker ice and $D = 5$ m.

The simulations suggest that, in some cases, a stationary grounded rubble pile provides support for advancing ice and thus facilitates overtopping. This was observed with $D = 5$ m when the ice sheet slid on top of the rubble pile and advanced to the structure as shown in Figure 35. The average speed of the ice blocks in the figure was recorded over an interval equivalent to 40 m of ice pushed against the structure. The figure clearly shows that grounding affects the process in a way that facilitates overtopping.

4.2.3 Rubble Pile Geometry

According to the ISO standard (International Organization for Standardization, 2008), large grounded rubble piles may form a protecting buffer in front of a structure. Thus the rubble pile formation and overtopping were investigated further by using rubble pile dimensions and volume to study the effect of the buffer provided by the grounded rubble, and to examine how grounding affects the evolution of the rubble pile during the simulation.

The rubble pile dimensions, width w_p, height h_p and depth D_p, were defined as illustrated in Figure 2 in Section 1.1. To distinguish the rubble pile from the overtopped ice, the maximum horizontal coordinate of the pile was defined as the point where the inclined part of the structure ends and the level surface begins. Thus the height of the pile h_p was set as the maximum vertical coordinate of the pile between the left edge of the pile and structure. The depth of the pile D_p was defined as the minimum vertical coordinate in the pile, limited by the seabed in the cases when grounding occurred. The pile height and width were measured from the water level. The left edge of the pile was defined to be the point where the thickness

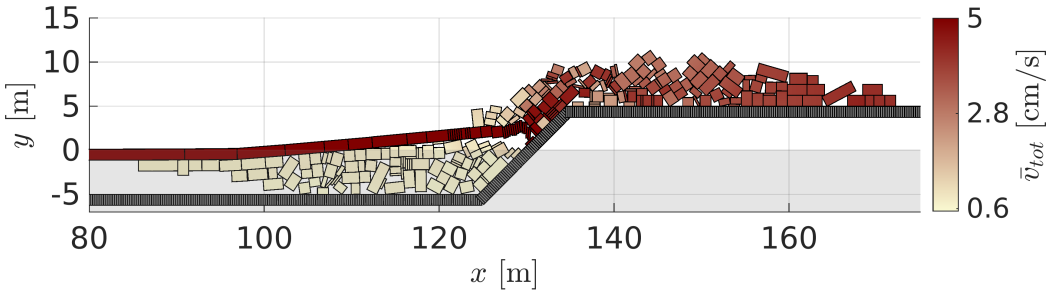

Figure 35: The grounded rubble remains stationary providing support for the ice sliding on top of it and advancing towards the structure. The support provided by the seabed thus facilitates overtopping. The legend shows the average speed $\bar{v}_{tot}$ calculated on an interval equivalent to 40 m of ice pushed against the structure.

of the pile $h_p + D_p < 1.05h$, where h is the ice thickness. The width of the pile w_p was thus defined as the distance between the point where the minimum pile height condition was satisfied and the point where the pile satisfies the condition set by the structure geometry. Further, the ice blocks with their centroid being on the right side of the top of the inclined part of the structure were considered overtopped.

The simulations showed that the changes in the pile height h_p were connected to changes in the pile width w_p when the rubble was grounded: h_p increased simultaneously with decreasing w_p when the rubble was pushed against the structure. This is illustrated by Figure 36, which gives the pile width w_p, height h_p and depth D_p as functions of the length of ice pushed against the structure L during a simulation with grounded rubble. The data is from a simulation with the wall angle $\alpha = 45°$, water depth $D = 5$ m and ice thickness $h = 1.25$ m.

The fluctuations of w_p in Figure 36a were observed throughout the simulation, which indicates that the rubble does not form a stable protecting buffer zone even though the w_p value increases during the whole interaction process. The pile height h_p illustrated in Figure 36b also has an increasing trend. The height undergoes several gradual increases followed by sudden drops. Furthermore, Figure 36c shows that the rubble grounds relatively soon after the beginning of the simulation. Once the rubble grounds, the depth of the pile remains equal to D. This occurred in simulations with $D = 2.5$ m and $D = 5$ m where the rubble grounded.

When the rubble is floating, the correlation between the pile width w_p and height h_p values towards the end of the simulation is not as pronounced as it is with grounded rubble, as shown by Figure 37. The figure illustrates the pile width w_p, height h_p and depth D_p as functions of the length of ice pushed against the structure L during a simulation with floating rubble. The data is from a simulation with wall angle $\alpha = 45°$, water depth $D = 15$ m and ice thickness $h = 1.25$ m. Figure 37a shows that w_p has an increasing trend but the fluctuations in its value are smaller when compared with w_p values of grounded rubble in Figure 36a. Furthermore, similarly to the grounded rubble, h_p of non-grounded rubble repeatedly increases and drops as shown in Figure 37b but the fluctuation decreases towards the end of the simulation and the overall height remains lower than the height of a grounded rubble pile. The depth of the pile, illustrated in Figure 37c, has an increasing trend throughout the simulation, as opposed to the constant value limited by the seabed when the rubble is grounded.

As already mentioned above, the whole rubble pile becomes packed towards the wall and grows in height when the force on the wall increases during a load event. The correlation between the pile geometry and the load on the structure was studied by comparing the normalised pile dimensions with the normalised force during a peak load event. The w_p, h_p and S_H values were normalised so that each quantity was divided by its maximum value during the load event. Figure 38 shows a close-up of the normalised force S_H and the pile dimensions h_p and w_p as functions of the ice pushed against the structure L during one load event. The figure shows a clear correlation between the pile dimensions and the force: When the force on the wall increases, the pile height increases and the pile width gradually decreases. Furthermore, when the load suddenly drops, a drop is observed in the pile height. At

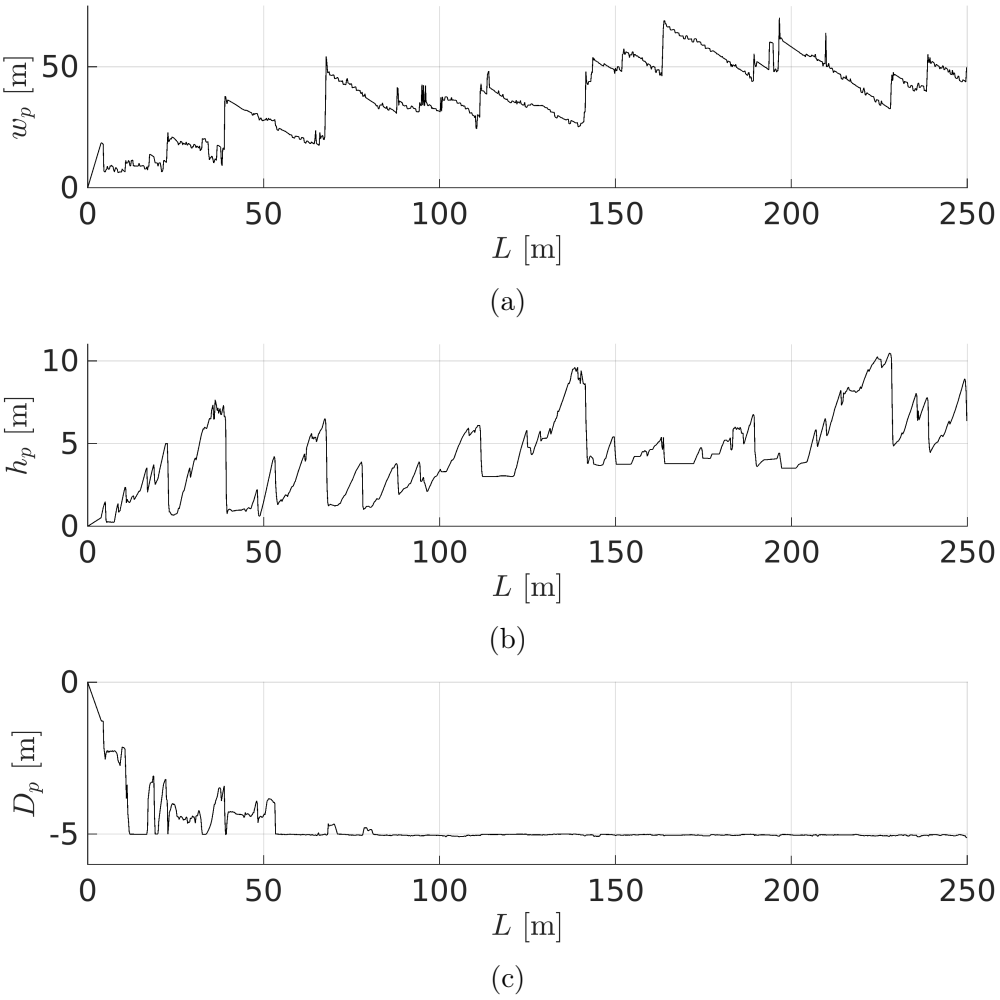

Figure 36: The simulation history of (a) the pile width w_p, (b) the pile height h_p and (c) the pile depth D_p as functions of the length of ice pushed against the structure L. The pile dimensions represent a simulation with grounded rubble.

the same time, the pile width suddenly increases. This correlation of simultaneous changes in the pile dimensions and the wall force supports the observation that the load peaks are related to the ride-up events.

The rubble width at the end of the simulation was investigated to study the effect of the water depth and the ice thickness on the formation of a protective rubble buffer. As Figure 37a showed, the width of the pile as a function of the length of the pushed ice fluctuates and undergoes sudden peaks and changes in its value. Therefore, to eliminate the effect of these fluctuations and sudden peaks, the width of the pile at the end of the simulation $\bar{w}_p$ was estimated by calculating the average value of the pile width from the last 100 m of the simulation. After estimating the pile width at the end of each individual simulation, the average pile width was obtained by calculating the mean end pile width of all the replicate simulations. Figure 39 illustrates the average pile width at the end of the simulation

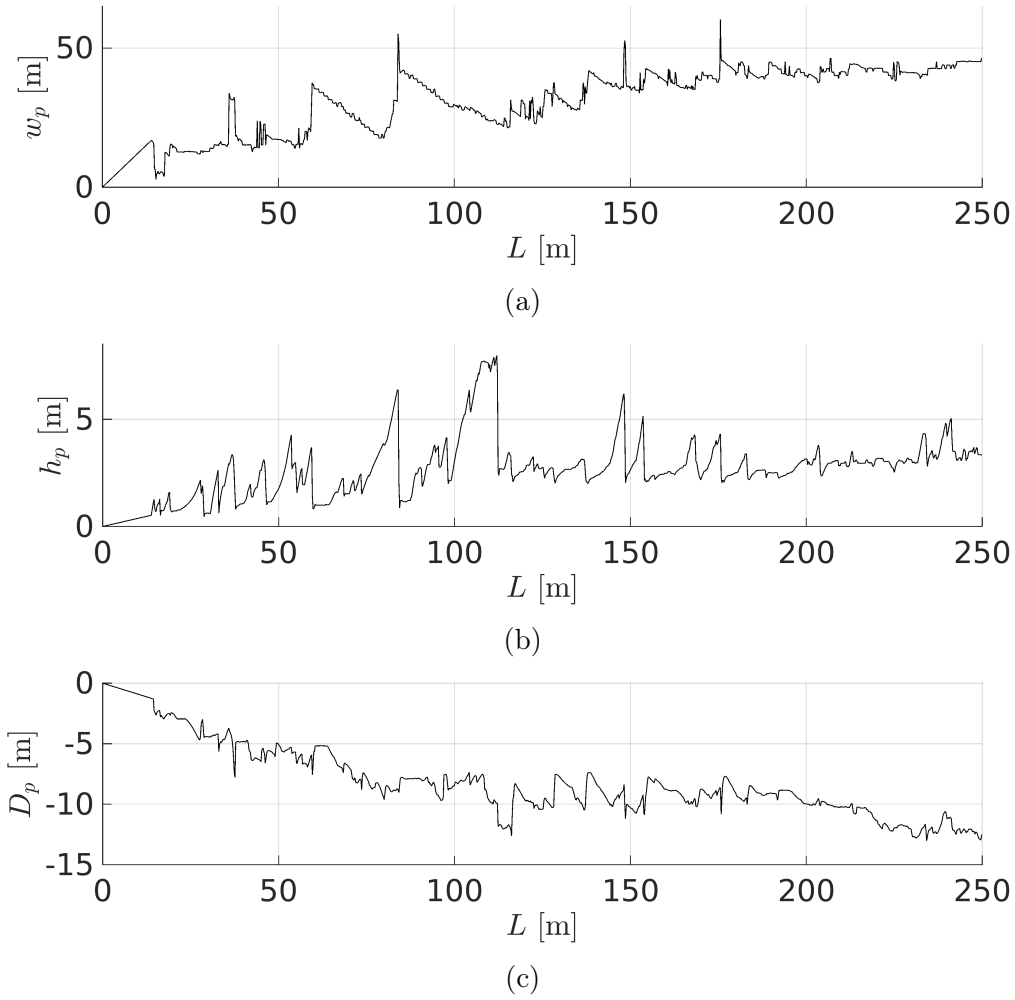

Figure 37: The simulation history of (a) the pile width w_p, (b) the pile height h_p and (c) the pile depth D_p as functions of the length of ice pushed against the structure L. The geometry data represents a simulation without grounded rubble.

at different water depths D and wall angles α. Figure 39a shows the results obtained with the thick ice ($h = 1.25$ m) and Figure 39b shows the results obtained with the thin ice ($h = 0.5$ m). Comparison of Figures 39a and 39b shows that using the thick ice generally results in longer rubble piles than the thin ice, excluding the results with $h = 1.25$ m and $D = 2.5$ m. The longer piles with thicker ice are naturally caused by the larger overall volume of the ice pushed against the structure during one simulation. The thicker ice also leads to larger scatter in the results.

The rubble pile width at the end of the simulation is typically similar with both wall angles. Furthermore, the pile width generally has a decreasing trend as the water depth increases. However, the results obtained with $h = 1.25$ m and $D = 2.5$ m are an exception to this as the pile widths at this water depth are substantially shorter when compared with the pile widths at $D = 5$ m (see Figure 39a). In addition, the simulations with $\alpha = 45°$ in this water depth lead to

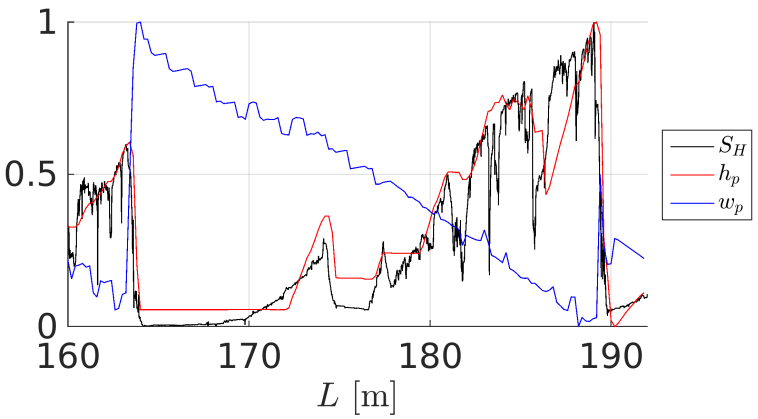

Figure 38: The normalised pile height h_p (in red), width w_p (in blue) and the force on the wall S_H (in black) as functions of the length of ice pushed against the wall L during a peak load event. Each quantity is normalised with respect to its largest value during the load event.

significantly shorter rubble piles than the simulations with $\alpha = 60°$. This is due to the intense overtopping that occurs with the thick ice in the shallowest water, as will be discussed in Section 4.2.4.

The rubble pile tends to grow horizontally when it is grounded at $D \leq 5$ m and vertically when it is not in contact with the seabed. This is seen when the $\bar{w}_p$ values of the grounded rubble are compared with the $\bar{w}_p$ values of the non-grounded rubble. In shallow water, $\bar{w}_p$ has a greater value compared with the results with floating rubble. For instance, the $\bar{w}_p$ values of the simulations with $h = 0.5$ m and $D = 2.5$ m are approximately 42.5 m (see Figure 39b). When the water depth increases to 5 m, $\bar{w}_p$ drops to approximately 30 m. Further decrease in the pile width is observed at $D = 10$ m and $D = 15$ m. When the decreasing trend in $\bar{w}_p$ with increasing D is compared with the typical w_p and h_p records of the simulation in Figures 36 and 37, it can be concluded that the rubble pile grows vertically until the growth is prevented by the seabed. In shallow water, the proximity of the seabed limits the vertical growth of the pile and thus its horizontal growth dominates the evolution of the pile dimensions.

4.2.4 Overtopping

The volume of the overtopped ice V_T at the end of each simulation and their mean value at each D and α were calculated. Figure 40 shows V_T as a function of D at both wall angles and ice thicknesses. The amount of ice on top of the structure is significantly higher with $D = 2.5$ m and $h = 1.25$ m than in the other cases, as seen in Figure 40a. In the simulations with these parameters, the large V_T values are related to low w_p values (see Figure 39a), as the total volume of ice pushed against the structure during the simulations was constant.

Comparison of the results at different wall angles shows that V_T was approx-

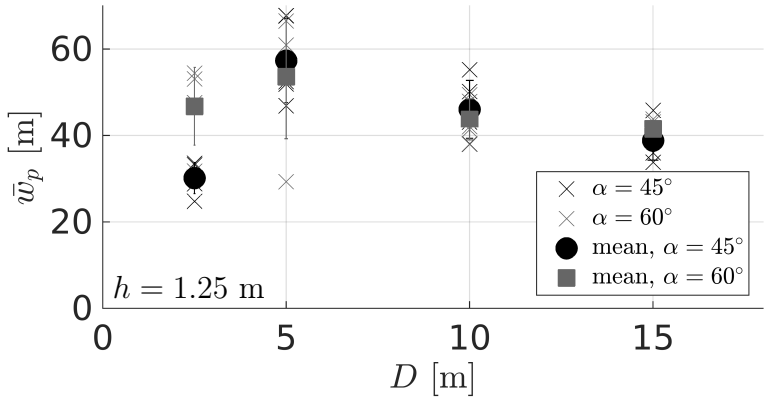

(a)

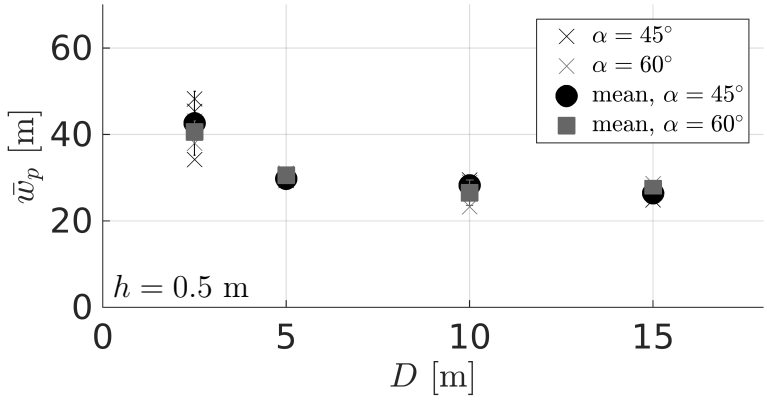

(b)

Figure 39: Average pile width $\bar{w}_p$ during the last 100 metres of the simulations as a function of the water depth D obtained with (a) ice thickness $h = 1.25$ m and (b) ice thickness $h = 0.5$ m.

imately constant with both α. However, the wall angle $\alpha = 45°$ seems to result in more intense overtopping, especially at $D = 2.5$ m and $h = 1.25$ m. This is a natural result of less force being required to push the rubble up along the wall with the smaller slope angle.

Figure 40a shows that overtopping was the most intense when the rubble formed from the thick ice was grounded. On the other hand, grounding did not affect the tendency of overtopping when the ice was thin, as seen in Figure 40b. Overall, the V_T values appear to increase as D decreases, which results in decreased forces on the seabed when the overtopping is intense. This can be seen by comparing Fiugres 28 and 40a: the loads $|\bar{B}_H|$ and $\bar{B}_V$ related to $h = 1.25$ m and $D = 2.5$ m ($D/h = 2$) at $\alpha = 45°$ are lower than the loads in deeper water with less overtopping.

In total, overtopping was observed in approximately 60 % of the 64 simulations. In approximately two thirds of the cases when overtopping occurred, overtopping was found to occur simultaneously with the maximum force on the wall.

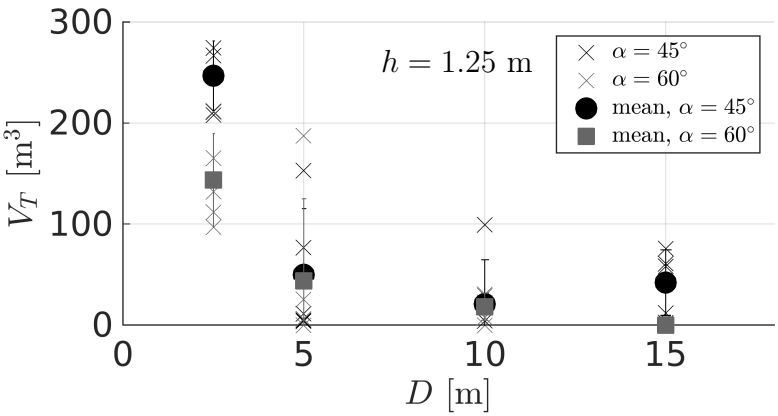

(a)

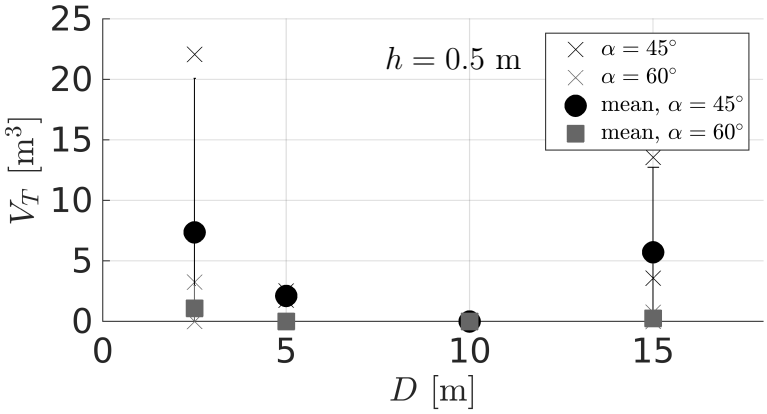

(b)

Figure 40: Volume of the overtopped ice at the end of the simulations as a function of the water depth D obtained with (a) ice thickness $h = 1.25$ m and (b) ice thickness $h = 0.5$ m.

4.3 Force Chains

The normalised block stresses were calculated to study the existence of so-called force chains in the rubble during load events. The block stresses are defined by the sum of the contact forces acting on the block divided by the area of the block (Peters *et al.*, 2005), and they were normalised with respect to the maximum stress at the instant of the peak of the load event. The blocks with higher than the average stress in the rubble form a network of particles called a force chain (Peters *et al.*, 2005), which demonstrates how the forces are distributed in the rubble and how they are transmitted to the structure.

Figure 41 shows the stress distribution in the rubble pile at the onset of a load peak, at the peak and after the peak during a ride-up event illustrated in the figure. The stresses in the figure are normalised with respect to the highest stress at instant (2) of the load event. Snapshot (1) of Figure 41 illustrates the pile at the onset of the load event. At this stage, the rubble pile is loose and free from stress concentrations,

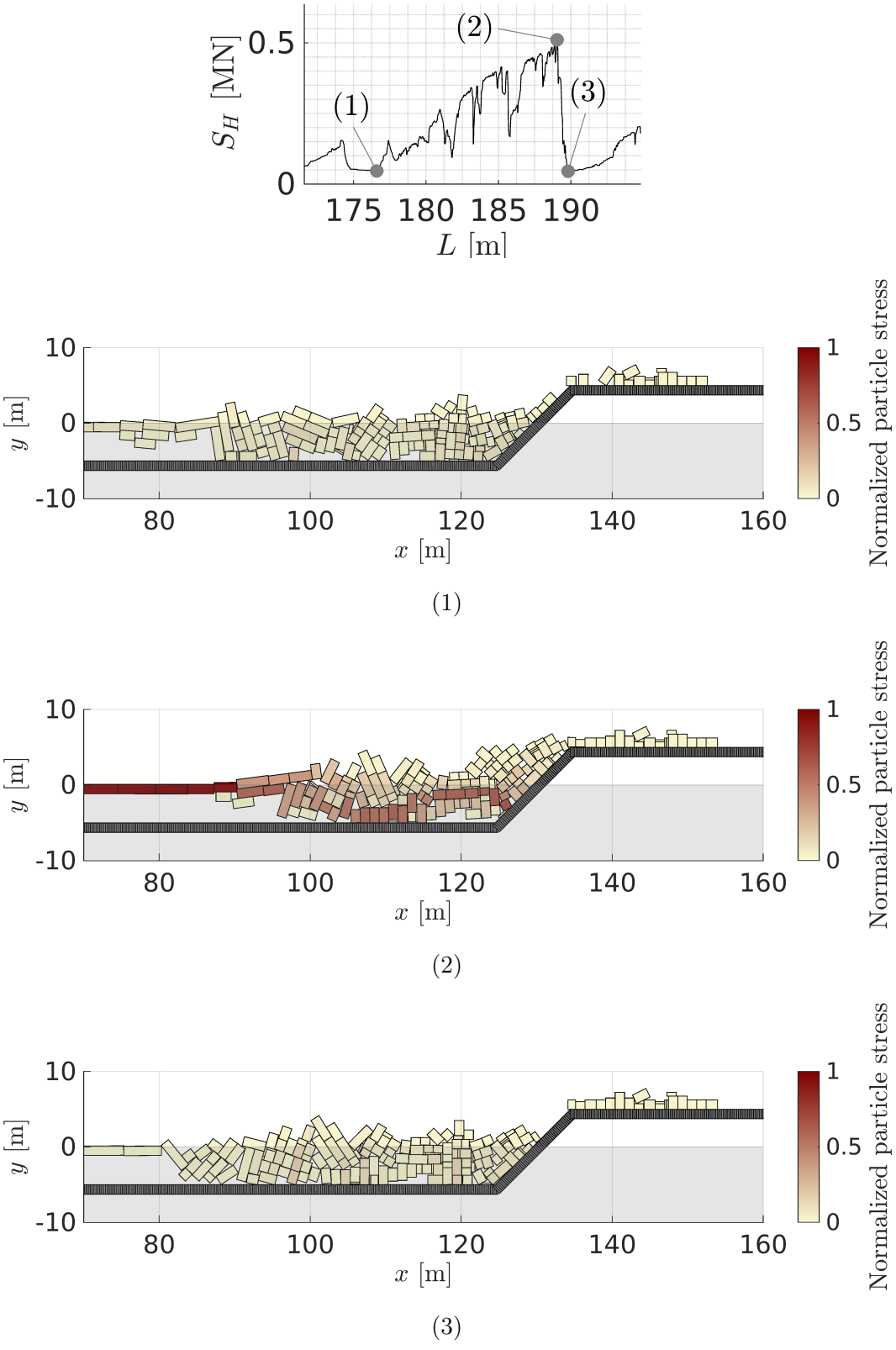

Figure 41: A close-up of a $S_H - L$ record showing a load event and snapshots illustrating the normalised block stress in the rubble during the load event: (1) at the onset of the load event, (2) at the peak and (3) after the load drop as illustrated in the load record. The stresses were normalised with respect to the highest stress at the peak of the load event (2).

in other words, the stresses in the rubble pile are evenly distributed and no force chains are observed. The load on the structure is mostly caused by the rubble at rest against it.

As more ice is pushed against the structure, the pile compresses against the structure and force chains begin to form. The stress distribution at the instant of the peak load is illustrated in Snapshot (2) of Figure 41, which shows a pronounced force chain transmitting the loads to the structure. The largest stresses are in the ice pushing the rubble at the left edge of the pile. As the figure shows, the forces are then transmitted to the structure along a network of ice blocks that passes through the rubble pile below the water line and partly along the seabed.

After the collapse of the rubble pile denoted as instant (3), the stress state in the rubble pile is released as shown in Snapshot (3) of Figure 41. The force chain is no longer observed and there is no compression in the advancing level ice sheet. The rubble pile is more loosely packed and the forces are distributed evenly in the rubble pile.

Similar force chains were found to be characteristic of all ride-up events with grounded rubble. The force chains in floating rubble were generally similar to the force chains in grounded rubble. However, in some cases, slight branching of the force chains was observed. In addition, sometimes the force chain strongly diverted downwards with $D = 10$ m when the rubble was partly in contact with the seabed. An example of a downward diverted force chain with slight branching is given in Figure 42. Furthermore, in the overtopping events where the majority of the rubble remained stationary, such as in the events illustrated in Figures 32 and 35, a force chain was observed in the ice blocks with the highest average speeds.

The sudden collapse of the rubble pile and the load drop related to that were often caused by buckling of the force chain. This is illustrated in Figure 43. Figure 43a shows the stress distribution in the rubble before the load drop and Figure 43b shows the stresses directly as the load starts to drop. The stresses are normalised

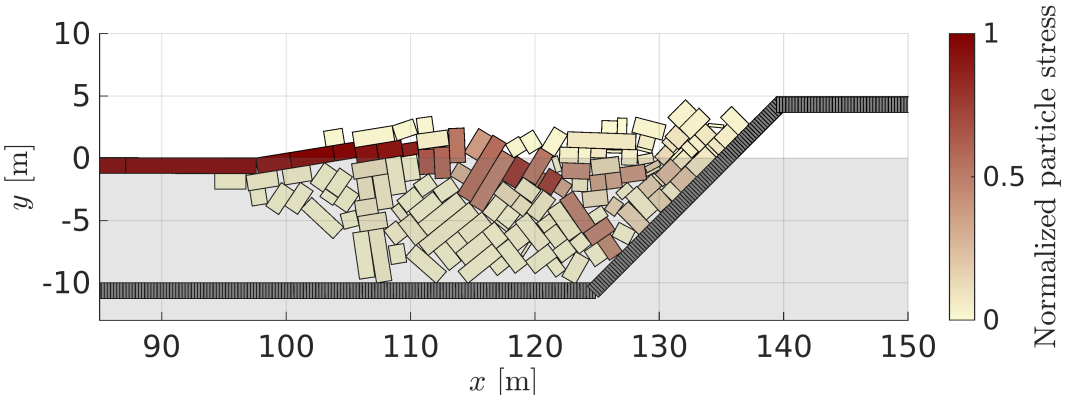

Figure 42: In some cases, the force chains branched and strongly diverted downwards. The diverted force chains were observed especially at $D \geq 10$ m when the rubble was partly in contact with the seabed. The stresses of the ice blocks are normalised with respect to the highest stress in the rubble.

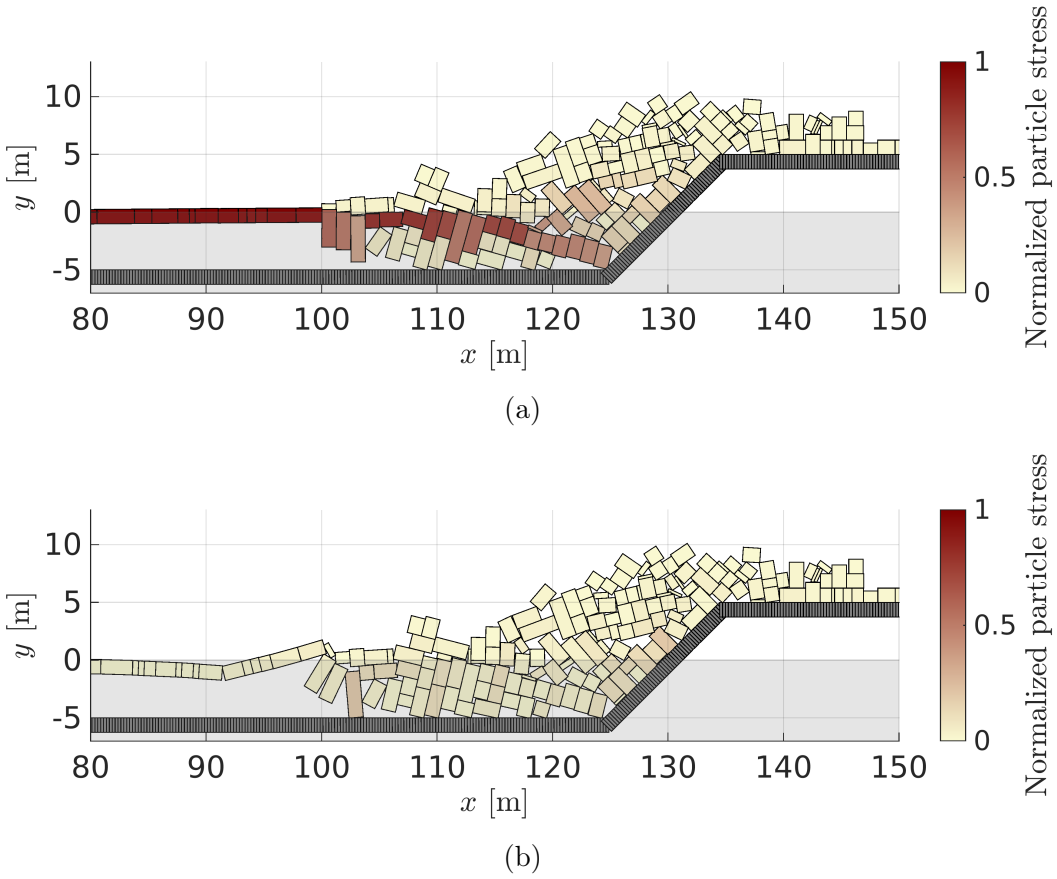

(a)

(b)

Figure 43: The sudden load drops and pile collapses related to ride-up events were often caused by buckling of the force chain. (a) shows the force chain at the peak of a load event and (b) shows how the force chain loses its stress carrying capacity as it buckles at $x \approx 91$ m. The stresses in (a) and (b) are normalised with respect to the highest stress in (a).

with respect to the highest stress during the peak in Figure 43a. At the peak of the load event, the forces are transmitted to the structure along a force chain that diverts slightly downwards. As the advancing ice increases the compression in the rubble, the force chain buckles at $x \approx 91$ m. As a result, the rubble pile collapses and the load on the wall abruptly drops.

5 Discussion

In this section, the simulation results are compared with full-scale observations and laboratory experiments. The loads and the deformation patterns are compared with the available data and the causes of the phenomena observed in the simulations are examined. The effect of the simulation parameters, such as the friction on the seabed and the simulation run time, are discussed and the applicability of the results is evaluated.

5.1 Ice Loads in the Simulations, Laboratory and Full-Scale

Based on the previous work by Timco *et al.* (1989), Sudom and Timco (2009) and Croasdale (2012), the ice load on the structure would be expected to reduce due to grounded rubble. However, the simulations on the ice-structure interaction here produced results that were contrary to the expected outcome as the load on the structure increased when the water depth decreased (see Figure 26). The increase in the peak forces was approximately 33 % and 92 % with the thick ice at 45° and 60°, respectively, when the loads on the structure in the cases with grounding were compared with the loads without grounding. With the thin ice, the corresponding increases were 50 % and 75 %.

Sudom and Timco (2009),Timco and Wright (1999), and Timco and Johnston (2004) report field observations on the load reduction on offshore structures due to grounded rubble. The load reduction through grounded rubble was studied by comparing the loads on the structure with similar events with floating rubble (Sudom and Timco, 2009), or comparing the loads on the structure with the loads measured at various points in the intact ice (Timco and Wright, 1999). The reduction in the peak loads observed at the Molikpaq was in the range of 60 % to 80 % (Sudom and Timco, 2009) and at Tarsiut Island approximately 85 % (Timco and Wright, 1999). The ice thickness reported at the Molikpaq and Tarsiut Island ranged from 0.7 m to 1.9 m, and the field data was collected over a long period of time, including the effects of consolidation and multi-year ice sheets. For instance, Sayed (1989) has reported an approximately 2.5 - 3 m thick consolidated layer of ice in grounded rubble which has a larger stiffness and strength compared with loose rubble. Thus it is likely to provide a more effective protecting buffer around the structure.

The simulations here only include freshly formed, non-consolidated rubble that may behave differently from rubble with refrozen layers and multi-year ice when it interacts with the seabed. Furthermore, the walls of the Molikpaq are inclined 82° from the horizontal plane above the water level and 67° from the horizontal plane below the water level, and the walls of Tarsiut Island are vertical. Vertical or close to vertical walls are known to induce higher loads on the structure, which may affect the proportion of loads transmitted to the seabed and to the structure through grounded rubble. According to the ISO standard (International Organization for Standardization, 2008), the failure mode of the ice in shallow water may change from crushing to bending failure or rubbling when the ice starts to fail against the grounded rubble pile. Thus the buffer effect may be partly caused by the changed

failure mode rather than the ice loads being carried by the seabed.

As expected, the simulations with no grounded rubble yielded maximum forces that are in good agreement with the results obtained in the FEM-DEM simulations on load transmission through the rubble in deep water by Paavilainen and Tuhkuri (2012). The deep water results have been validated against laboratory tests and field data and can therefore be regarded as a good reference. However, the simulation results with no grounded rubble are significantly different from the loads measured in the intact ice at Tarsiut Island by Timco and Wright (1999), even though they should, in theory, be of similar magnitude according to the load balance assumption. The loads measured in the intact ice at Tarsiut Island were in the range of 1.5 MN to 3 MN when divided by the structure width to make them comparable with the 2D loads, whereas the peak loads without grounded rubble in the simulations ranged from 0.16 MN with the thin ice to 0.9 MN with the thick ice. It is not apparent what causes this mismatch. It is suggested that it may be partly due to a measurement technique that is not ideal for calculating loads in the ice. The forces in the ice were estimated with strainmeters that were placed in the intact ice at various locations around the caisson. According to Sanderson (1988), deriving forces from strainmeter data should, however, be considered with caution as strainmeters are better suited for studying ice deformations than forces.

Karulin *et al.* (2007) observed in model scale experiments that grounded rubble may lead to both increased and decreased loads on the structure when compared with deep water results. They found that the load increases at the initial stage of the ice-structure interaction when the process is governed by the friction on the seabed resisting the motion of rubble away from the structure, which increases the load on the structure. The reported increases in the forces on the wall ranged from 20 % to 50 % when the loading through grounded and non-grounded rubble were compared. This is in good agreement with the results obtained in the FEM-DEM simulations with $\alpha = 45°$ (unfortunately, the inclination angle of the model in Karulin *et al.* (2007) was not documented). They also observed that, as the amount of rubble increased, the rubble pile became stationary. As a consequence, the load-increasing effect of the grounded rubble ceased and the ice breaking process shifted to the outer edge of the rubble pile. Similar behaviour was observed in the simulations with $D = 2.5$ m, $h = 1.25$ m and $\alpha = 60°$. After the major load drop in the loading sequence in Figure 31, the process shifted to the outer edge of the pile while the rest of the pile remained immobile. However, in the simulations the pile eventually became mobilised and new load events occurred. The experiments by Karulin *et al.* (2007) may not have been long enough so that this would have been observed. Furthermore, the properties of model ice are different from real sea ice, which may affect the experiment results.

Laboratory experiments on ice-structure interaction against a vertical wall in shallow water conducted by Timco *et al.* (1989) suggest that only small horizontal forces are carried by the seabed. Timco *et al.* (1989) found that the portion of the load carried by the seabed decreased with time as the total horizontal force increased and a larger portion of the load was transmitted to the structure. This is in agreement with the simulation results as the loads on the seabed B_H were only

approximately 10 to 15 % of the loads on the structure S_H.

Timco *et al.* (1989) used the rigid body assumption to estimate the maximum values for the friction ratio B_H/B_V and obtained values ranging from 0.1 to 0.2, which in good agreement with the friction coefficient $\mu_{is} = 0.1$ used in the simulations. Furthermore, the corresponding friction ratio in the simulations varied between -0.1 and 0.1. Therefore, it can be concluded that the force B_H is caused by friction.

Sayed (1989), and Timco and Wright (1999) report rubble piles that remained firmly grounded throughout the winter period. This suggests that the friction coefficient between the seabed and the ice has been relatively high in the field. The friction coefficient used in the FEM-DEM simulations was, however, relatively low ($\mu_{is} = 0.1$). Thus it is likely that the model could not predict the load reduction on the structure due to an underestimated friction coefficient. During the peak loads, the forces were, however, transmitted to the structure partly along the seabed, as discussed in Section 4.3. Therefore, increasing the friction coefficient is expected to increase the portion of the forces transmitted to the seabed.

It was shown in Section 4.1.2 that the wall angle affected the magnitude of the peak loads throughout the simulations when the rubble was grounded. As shown by Figure 26, the wall angle $\alpha = 60°$ induced higher loads on the structure than $\alpha = 45°$ during the whole simulation run. However, in the FEM-DEM simulations in deep water by Ranta *et al.* (2014), the inclination angle affected the loads only at the initial stage of the simulation and lost its importance at later stages when the ice started to fail against the rubble pile. It is suggested that the ice is subjected to higher compression as it encounters the steeper wall, and the grounded rubble provides support for the load transmission as will be discussed in the next section.

5.2 Load Records and Mechanics of the Load Events

The model experiments by Timco *et al.* (1989) and the simulations produce similar load records. In the model experiments, the horizontal force on the wall underwent several load events with gradual build-up and a sudden drop, as observed also in the simulations (see Figure 23a). Similarly to the load records in Figures 23b and 23c, the forces on the seabed in the experiments had an increasing trend, with the horizontal force changing its sign so that a sudden drop in the horizontal force led to a negative value. In addition, careful inspection of the load records shows that the load drops on the seabed in the laboratory experiment occurred simultaneously with load drops measured on the wall, which is in agreement with the load records of the simulations. Sudden load drops after a gradual increase of the load were also seen in the force records of the model tests by Karulin *et al.* (2007).

The observations based on the simulations here suggest the following mechanism leading to increase in the maximum ice load values: when the rubble is grounded, the pile and the force chains are supported from below by the seabed and from above by the rubble above the force chain (see Figure 41). The force chain is thus supported from both sides and is therefore likely to sustain higher loads than a force chain in a non-grounded rubble pile. In the case of non-grounded rubble, the force chains may

more easily buckle downwards since the pile can freely move in the vertical direction and the only vertical forces acting on it are the gravity and the buoyancy.

Furthermore, the average forces on the seabed, $\bar{B}_V$ and $|\bar{B_H}|$, increased as the value of S_H^m increased, as shown in Figure 28. This increase is unexpected and further suggests that the grounded rubble enhances the load build-up on the wall. It appears that the supporting effect of the seabed dominates the load transmission and outweighs the grounding resistance. Timco *et al.* (1989) made a similar observation in laboratory experiments. According to them, the grounding resistance of the seabed is exceeded as the force increases.

The simulations showed that the load events, when the force gradually builds up and suddenly drops, are related to the so-called ride-up events as shown by Figures 29 and 30. In a ride-up event the advancing ice often pushes the rubble pile along the seabed and up the structure wall. This occurs until the pile collapses, which is seen as a sudden drop in the force records. The sudden load drops are related to the buckling of force chains that transmit the forces to the structure, as has already been observed in the simulations by Paavilainen and Tuhkuri (2013). No ride-up events have been reported in field data or model scale tests in shallow water, but in all reported cases the structures have either been vertical or close to vertical, or the intact ice sheet has failed against a firmly grounded rubble pile (Timco and Wright, 1999).

5.3 Pile Geometry and Overtopping

The rubble pile widths reported in the field are generally longer than the $\bar{w}_p$ values at the end of the simulation, which suggests that the load reduction is related to large buffer zones in front of the structure. As shown by Figure 39, the average $\bar{w}_p$ values from the simulations ranged from 41 m to 58 m in the cases without predominant overtopping that occurred with $D = 2.5$ m, $h = 1.25$ m and $\alpha = 45°$, whereas Timco and Wright (1999) reported pile lengths up to 150 m at Tarsiut Island, and Sudom and Timco (2009) reported pile widths up to 50 m, 300 m and 600 m at different locations of the Molikpaq. The loads related to the longest, 300 m and 600 m, piles were 50 MN and 25 MN, respectively, which suggests that a larger buffer zone reduces the loads on the structure more effectively. The rubble in these cases accumulated in front of the structure over a long period of time and remained grounded throughout the winter, and the ice was substantially thicker than the ice used in the simulations. It is thus expected that similar pile widths and load reduction would be observed if more ice was pushed against the structure in the simulations. The geometry of the seabed and consolidation are also likely to affect the rubble accumulation.

Palmer and Croasdale (2012) suggest that grounded rubble may provide support for higher ride-up. Naturally, if the structure height is limited, this will lead to increased overtopping as observed in the simulations (see Figure 40). As the water depth in the simulations decreased, the probability of overtopping increased, and intense overtopping in shallow water occurred by two distinct mechanisms. In the shallowest water, the downward growth of the pile is prohibited by the seabed and

the mechanism of overtopping is such that the ice advances to the structure as a line of moving blocks that are kept aligned and pressed against the seabed by the rubble on top of the advancing ice (see Figure 33).

In some cases, the ice advanced to the structure on top of grounded rubble as shown by Figure 35. Similar behaviour was reported at Esso's Caisson Retained Island by Marshall *et al.* (1989) who reported a rubble building event where new rubble overtopped existing rubble and pile heights up to 5 m were measured. It is suggested that this phenomenon is at least partly enabled by the supporting effect of the seabed. In shallow water, the rubble pile supports itself against the seabed so that the advancing ice can climb on top of the pile. The ice advances to the structure close to the water level and exerts high loads on the structure while the rubble under the advancing ice remains stationary.

5.4 Occurrence of Grounding

When grounding occurred in the simulations, the water depth to ice thickness ratios, D/h, were similar to the ratios measured in the field and in laboratory experiments related to grounded rubble. The water depths D, ice thicknesses h and the ratios D/h of the relevant experiments are collected in Table 2 to compare them with the simulation results. In the simulations, grounding was observed with $D \leq 5$ m and occasional grounding was observed when $h = 1.25$ m at $D = 10$ m, which corresponds to a maximum ratio $D/h = 10$. The table shows that grounding in the simulations here was observed with D/h ratios that are in good agreement with laboratory experiments conducted by Karulin *et al.* (2007). Karulin *et al.* (2007) report grounding in model experiments at water depths corresponding to 7.8 m when converted to full-scale values and no grounding at water depths corresponding to 12.2 m. The ice thickness in the laboratory experiments corresponded to $h = 0.8$ m

Table 2: The D/h ratios of rubble piles in the simulations are in good agreement with most of the ratios observed in laboratory and field experiments related to grounding. D is the water depth and h is the ice thickness.

Experiment	D [m]	h [m]	D/h	Grounded
Simulations, max. D/h	5	0.5	10	Yes
Model scale experiment[a]	7.8	0.8	9.75	Yes
Model scale experiment[a]	12.2	0.8	15.25	No
Tarsiut Island[b,c]	6	1 . . . 2.5	2.4 . . . 6	Yes
The Molikpaq[c]	13.4	1.9	7.1	Yes
The Molikpaq[c]	15.8	1.7	9.3	Yes
The Molikpaq[c]	19.5	1.5 . . . 1.8	10.8 . . . 13	Occasionally
ESSO's CRI[d]	9	0.2	45	Yes

[a] Karulin *et al.* (2007) [b] Timco and Wright (1999) [c] Sudom and Timco (2009)
[d] Marshall *et al.* (1989)

in full scale, yielding D/h ratios 9.75 and 15.25 for the grounded and non-grounded rubble, respectively.

The observations made at Tarsiut Island (Timco and Wright, 1999; Sudom and Timco, 2009) and at the Molikpaq (Sudom and Timco, 2009) are within the range of the maximum D/h ratio for grounding observed in the simulations. When occasional grounding was observed at the Molikpaq, the grounding ratio slightly exceeded the maximum D/h in the simulations but is still in fair agreement with the simulation results. A clear exception are the field observations at ESSO's Caisson Retained Island that yield grounding with $D/h = 45$ (Marshall *et al.*, 1989). Grounding at that high ratios could not be predicted in the simulations.

5.5 Applicability of the Results

It is desirable that in the FEM-DEM simulations, the smallest ice block size would not be limited by the chosen discrete element size. However, with $D = 2.5$ m, some parts of the ice sheet occasionally failed abruptly into a large number of ice blocks with the size of one discrete element, as shown in Figure 32. The majority of them fragment naturally in the rubbling process when the chain of ice blocks bends towards the seabed and then steeply up when forced by the structure geometry. Some of the smallest fragments are, however, occasionally formed by strong stress waves that that propagate in the ice due to sudden impacts. This effect is clearly pronounced in the shallowest water as the blocks hit the seabed instantly after the rubble pile collapses, whereas in deeper water the viscosity of the water slightly dampens the impact. One reason for this phenomenon might be that the dissipation in the ice is not sufficient to attenuate the stress wave and thus the ice breaks into a sequence of blocks that are the size of a discrete element when the wave propagates through the ice sheet. The discrete elements are rigid and as such omit the elastic behaviour of the ice. However, the fragmentation of the ice due to this phenomenon does not largely affect the physical phenomena related to the process.

Unexpectedly, the grounded rubble did not lead to a load reduction in the simulations. Running the simulations with longer duration may reproduce results that capture the load-decreasing effect of rubble grounding. According to a theoretical model introduced by Marshall et al. (1991), the load on the structure is likely to drop to zero over a long time period of ice-structure interaction. Field observations also report negligible stresses on the structure when grounded rubble is present (Sayed, 1989; Marshall *et al.*, 1989). The field observations are made over long periods of time, usually during one winter. Furthermore, Karulin *et al.* (2007) observed that in laboratory experiments the load decreased towards the end of the simulations, which further supports that the simulation run time should be longer.

In addition, the model tests by Karulin *et al.* (2007) showed that the friction coefficient between the ice and the seabed is a governing parameter in the ice-structure-seabed interaction process. This further supports the notion that using a higher friction coefficient in the simulations would produce results better corresponding to the field observations on load reduction due to grounded rubble. Furthermore, the geometry of the seabed in the model was relatively simple, and making it more

complex by inclining it is likely to promote the load-decreasing effect of grounded rubble.

It should be noted that the number of replicate simulations in this study was relatively low. Only five simulations of each case were run with $h = 1.25$ m and three simulations with $h = 0.5$ m. Scatter in the results is large making the results subject to large alteration due to anomalies in individual results. Therefore, the results should be considered with caution and more replicate simulations are needed. Despite the large scatter, the simulation results produce similar physical phenomena than observed in the field and in model scale tests.

6 Conclusions

The main purpose of this study was to investigate ice-structure interaction in shallow water by using 2D FEM-DEM simulations. In the simulations, an intact ice sheet was pushed against an inclined structure. The varied parameters included ice thickness, water depth and the structure inclination angle, while the other model parameters were chosen according to real sea ice properties.

The intact ice sheet was modelled as a sequence of discrete elements that were joined together by nonlinear Timoshenko beam elements. The intact ice sheet behaved as linear elastic material and its fracture into smaller blocks was modelled using the cohesive crack model. The linear elastic behaviour of the ice and its fracture were modelled using the finite element method. The discrete element method was used to calculate the contact forces of the ice blocks when they interacted with each other, with the structure or with the seabed. The force and the contact data of the interacting ice blocks was recorded to study the phenomena related to the process. The investigated phenomena included the mechanics of the rubble deformations leading to maximum loads, the load transmission through the rubble, overtopping and the pile geometry and its deformation.

Contrary to the initial assumption, the loads in the shallow water increased when the rubble was grounded. The load increase ranged from 33 % to 92 % depending on the ice thickness and inclination angle. The thicker ice and the larger wall angle induced the highest loads on the structure (see Figure 26). The simulations could not reproduce the load reduction observed in full-scale measurements but the results were at least partly in agreement with laboratory tests. It is suggested that the load increase here is caused by the support the grounded rubble and the seabed provide for the advancing ice. Furthermore, it is likely that the disagreement between the results is partly caused by the relatively low friction coefficient between the ice and the seabed. The behaviour of the rubble in contact with the seabed is likely to change with a higher friction coefficient.

The typical load records of the simulations yielded a pattern of repeated load events where the force gradually built up and abruptly dropped as shown by Figure 23a. These were due to ride-ups described in Section 4.2.1: when the advancing ice pushed the rubble pile along the seabed and up the structure wall, a gradual increase in the load record was observed. The forces were transmitted to the structure along force chains, which buckled when they reached their maximum load carrying capacity. The buckling was observed as an abrupt load drop in the load record and as a sudden collapse of the rubble pile.

The load pattern related to overtopping had several consecutive sharp load peaks with a sudden load increase and a gradual load drop (see Figure 23a). As described in Section 4.2.2, during this zigzagging load pattern, the ice advanced to the structure pressed against the seabed by the rubble on top of the advancing ice. The sudden increase in the load was caused by the ice sheet being compressed against the structure and being forced to turn to ride up along the structure. As the ice turned to ride up the structure, the compression in the ice was released and an increasing gap formed between the rubble and the lower corner of the structure. This

was seen as a gradual load drop in the load record. The overtopping ceased in a major load drop followed by a close-to-constant force on the wall. At the instant of the major load drop, the rubble pile collapsed and extended far from the structure. After this, it remained stationary in front of the structure, which was seen as the constant force in the load record.

The probability of overtopping increased as the water depth decreased. Furthermore, the ice thickness and wall angle affected overtopping so that the probability of overtopping increased with $\alpha = 45°$ and $h = 1.25$ m (see Figure 40). The thick ice interacting with a 45-degree wall in the shallowest water led to significantly larger amount of overtopped ice than the other simulation cases. The increased probability of overtopping in shallow water is likely to be a consequence of the supporting effect of the seabed. Furthermore, overtopping also occurred when the ice slid to the structure on top of a grounded rubble pile as shown by Figure 35. In this case, the grounded rubble clearly facilitated overtopping by supporting the advancing ice.

Naturally, when intense overtopping occurred, the rubble pile at the end of the simulation was shorter when compared with the cases when rubble was grounded but no overtopping occurred. As the water depth increased, the pile width decreased and the pile grew vertically since the growth of the rubble pile was not constrained by the seabed. The rubble was found to ground at water depths less than 10 m regardless of the ice thickness or the inclination angle (see Figure 27), which is in good agreement with the full-scale measurements.

Based on the results in this thesis, it can be argued that grounded rubble piles in front of structures do not necessarily reduce loads on the structure. The effect of grounding may, in fact, be load-increasing, especially if the duration of the interaction is not extensively long. Extending the simulation run time may thus produce results that bring out the load-reducing effect of the grounded rubble.

To further verify the simulation results, more replicate simulations would be needed. Furthermore, the author believes that increasing the friction coefficient on the seabed would yield results that are in better agreement with the field data. In addition, a higher friction coefficient is likely to keep the rubble pile more firmly grounded and prevent the whole pile being pushed along the seabed and up the structure wall, as was seen in the ride-up events.

A natural follow-up to this project would be to run more simulations with the suggested modifications and possibly with a more complex seabed geometry and a higher friction coefficient. It would also be beneficial to conduct model scale experiments to verify the simulations results. A thorough dimensional analysis on the results could also reveal new trends regarding the phenomena studied in this thesis.

References

Atkins, A. 1975. *Icebreaking Modeling.* Journal of Ship Research, vol. 18, pp. 40-43. ISSN 0022-4502.

Barker, A. and Croasdale, K. 2004. *Numerical Modelling of Ice Interaction with Rubble Mound Berms in the Caspian Sea.* Proceedings of the 17th International Symposium on Ice, IAHR 04, vol. 2, pp 257-264. St. Petersburg, Russia [Electronic publication].

Barker, A. and Timco, G. 2007. *Modelling Rubble Field Development at Isserk I-15 and Its Implications for Engineering Ice Rubble.* Proceedings of the 19th International Conference on Port and Ocean Engineering under Arctic Conditions, POAC 07, vol. 2. pp. 485-496. Dalian, China. ISBN 978-7-5611-3631-7. ISSN 2077-7841 [Electronic publication].

Croasdale, K., Cammaert, A. and Metge, M. 1994. *A method for the calculation of sheet ice loads on sloping structures.* Proceedings of the 12th International Symposium on Ice, IAHR 94, vol. 2, pp 874-885. Trondheim, Norway. ISBN 82-7482-011-8.

Croasdale, K. 2011. *Platform shape and ice interaction: a review.* Proceedings of the 21st International Conference on Port and Ocean Engineering under Arctic Conditions, POAC 11, vol. 1. p. 10. Montréal, Canada. ISSN 2077-7841 [Electronic publication].

Croasdale, K., Jordaan, I. and Verlaan, P. 2011. *Offshore platforms and deterministic ice actions: Kashagan phase 2 development: North Caspian Sea.* Proceedings of the 21st International Conference on Port and Ocean Engineering under Arctic Conditions, POAC 11, vol. 2. p. 10. Montréal, Canada. ISSN 2077-7841 [Electronic publication].

Croasdale, K. 2012. *Ice rubbling and ice interaction with offshore facilities.* Cold regions science and technology, vol. 76-77, pp. 37-43. ISSN 0165-232X. doi 10.1016/j.coldregions.2011.06.005.

Cundall, P. and Strack, O. 1979. *A discrete numerical model for granular assemblies.* Géotechnique, vol. 29(1), pp. 47-65. ISSN 0016-8505. doi 10.1680/geot.1979.29.1.47.

Dempsey, J., Adamson, R. and Mulmule, S. 1999. *Scale effects on the in-situ tensile strength and fracture of ice. Part II: first-year sea ice at Resolute, N.W.T.* International Journal of Fracture, vol. 95(1-4), pp. 347-366. ISSN 1573-2673. doi 10.1023/A:1018650303385.

Dempsey, J. 2000. *Research trends in ice mechanics.* International Journal of Solids and Structures, vol. 37(1-2), pp. 131-153. ISSN 0020-7683. doi 10.1016/S0020-7683(99)00084-0.

Evers, K.-U. and Weihrauch, A. 2004. *Design and model testing of ice barriers for protection of offshore structures in shallow waters during winter*. Proceedings of the 17th International Symposium on Ice, IAHR 04, vol. 2, pp. 124-131. St. Petersburg, Russia [Electronic publication].

Felippa, C., 2001. *Nonlinear Finite Element Methods*. University of Colorado, Boulder, CO. Material assembled from lecture notes for the course Nonlinear Finite Element Methods. [Online] Available at: http://www.colorado.edu/engineering/cas/courses.d/NFEM.d/ [Accessed 23 April 2015].

Gálvez, J., Červenka, J, Cendón, D. and Saouma, V. 2002. *A discrete crack approach to normal/shear cracking of concrete*. Cement and Concrete Research, vol. 32(10), pp. 1567-1585. ISSN 0008-8846. doi 10.1016/S0008-8846(02)00825-6.

Goldstein, R., Onishchenko, D., Osipenko, N., Shushpannikov, P. and Naumov, M. 2013. *Grounded ice pile-up. 2D DEM simulation*. Proceedings of the 22nd International Conference on Port and Ocean Engineering under Arctic Conditions, POAC 13, p. 12. Espoo, Finland. ISSN 2077-7841 [Electronic publication].

Gürtner, A. 2009. *Experimental and Numerical Investigations of Ice-Structure Interaction*. Thesis for degree of philosophiae doctor, p.182. Norwegian University of Science and Technology, Trondheim, Norway. ISBN 978-82-471-1420-9. ISSN 1503-8181.

Heinonen, J. 2004. *Constitutive Modeling of Ice Rubble in First-Year Ridge Keel*. VTT Publications 536. Espoo, Finland: Otamedia Oy, p. 142. ISBN 951-38-6390-5. ISSN 1235-0621.

Hillerborg, A., Modéer, M. and Petersson, P.-E. 1976. *Analysis of crack formation and crack growth in concrete by means of fracture mechanics and finite elements*. Cement and Concrete Research, vol. 6(6), pp. 773-781. ISSN 0008-8846. doi 10.1016/0008-8846(76)90007-7.

Hopkins, M. and Hibler, W. 1991. *On the shear strength of geophysical scale ice rubble*. Cold Regions Science and Technology, vol. 19(2), pp. 201-212. ISSN 0165-232X. doi 10.1016/0165-232X(91)90009-6.

Hopkins, M., Hibler, W., and Flato, G. 1991. *On the numerical simulation of sea ice ridging process*. Journal of Geophysical Research, vol. 96(C3), pp. 4809-4820. ISSN 2156-2202. doi 10.1029/90JC02375.

Hopkins, M. 1992. *Numerical Simulation of Systems of Multitudinous Polygonal Blocks*. CRREL Report 92-22. US Army Corps of Engineers Cold Regions Research & Engineering Laboratory, Hanover, NH, USA, p. 69.

Hopkins, M. 1994. *On the ridging of intact lead ice*. Journal of Geophysical Research, vol. 99(C8), pp. 16351-16360. ISSN 2156-2202. doi 10.1029/94JC00996.

Hopkins, M. 1997. *Onshore ice pile-up: a comparison between experiments and simulations*. Cold Regions Science and Technology, vol. 26(3), pp. 205-214. ISSN 0165-232X. doi 10.1016/S0165-232X(97)00015-3.

Hopkins, M., Tuhkuri, J. and Lensu, M. 1999. *Rafting and ridging of thin ice sheets*. Journal of Geophysical Research, vol. 104(C6), pp. 13605-13613. ISSN 2156-2202. doi 10.1029/1999JC900031.

Ibrahimbegovic, A. and Delaplace, A. 2003. *Microscale and mesoscale discrete models for dynamic fracture of structures built of brittle material*. Computers and Structures, vol. 81(12), pp. 1255-1265. ISSN 0045-7949. doi 10.1016/S0045-7949(03)00040-3.

International Organization for Standardization. 2008. *Petroleum and natural gas industries – Arctic offshore structures*. ISO 19906:2008.

Karulin, E., Karulina, M. and Blagovidov, L. 2007. *Ice model tests of caisson platform in shallow water*. International Journal of Offshore and Polar Engineers, vol. 17(4), pp. 270-275. ISSN 1053-5381.

Kolari, K. 2007. *Damge mechanics model for brittle failure of transversely isotropic solids*. VTT Publications 628. Helsinki, Finland: Edita Prima Oy, p. 195. ISBN 978-951-38-6995-3. ISSN 1235-0621.

Kolari, K., Kuutti, J. and Kurkela, J. 2009. *FE-simulation of continuous ice failure based on model update technique.* Proceedings of the 20th International Conference on Port and Ocean Engineering under Arctic Conditions, POAC 09, vol. 2. p. 10. Luleå, Sweden. ISSN 2077-7841 [Electronic publication].

Konuk, I., Gürtner, A. and Yu, S. 2009. *Study of Dynamic Ice and Cylindrical Structure Interaction by the Cohesive Element Method*. Proceedings of the 20th International Conference on Port and Ocean Engineering under Arctic Conditions, POAC 09, vol. 2. p. 12. Luleå, Sweden. ISSN 2077-7841 [Electronic publication].

Kulyathkin, S. and Høyland, K. 2015. *Ice rubble frictional resistance by critical state theories*. Cold Regions Science and Technology, In press - accepted manuscript, Available online 13 August 2015. p 23. ISSN 0165-232X. doi 10.1016/j.coldregions.2015.08.003.

Lau, M., Wang, J. and Lee, C. 2007. *Review of ice modeling methodology*. Proceedings of the 19th International Conference on Port and Ocean Engineering under Arctic Conditions, POAC 07, vol. 1. pp. 350-362. Dalian, China. ISBN 978-7-5611-3631-7. ISSN 2077-7841 [Electronic publication].

Li, G., Braun, K., Hudson, B. and Sayed, M. 2009. *When Will Ice Ride-Up or Pile-Up Occur?* Proceedings of the 20th International Conference on Port and Ocean Engineering under Arctic Conditions, POAC 09, vol. 1, p. 10. Luleå, Sweden. ISSN 2077-7841 [Electronic publication].

Liferov, P. 2005. *Ice rubble behaviour and strength Part II. Modelling* Cold regions science and technology, vol. 41(2), pp. 153-163. ISSN 0165-232X. doi 10.1016/j.coldregions.2004.10.002.

Liferov, P. and Bonnemaire, B. 2005. *Ice rubble behaviour and strength: Part I. Review of testing and interpretation of results.* Cold regions science and technology, vol. 41(2), pp. 135-151. ISSN 0165-232X. doi 10.1016/j.coldregions.2004.10.001.

Lu, W., Serre, N., Høyland, K. and Evers, K.-U. 2013. *Rubble Ice Transport on Arctic Offshore Structures (RITAS), part IV: Tactile sensor measurement of the level ice load on inclined plate.* Proceedings of the 22nd International Conference on Port and Ocean Engineering under Arctic Conditions, POAC 13, p. 14. Espoo, Finland. ISSN 2077-7841 [Electronic publication].

Lu, W. 2014. *Floe Ice - Sloping Structure Interactions.* Thesis for degree of philosophiae doctor, p.116. Norwegian University of Science and Technology, Trondheim, Norway. ISBN 978-82-326-0560-6. ISSN 1503-8181.

Lu, W., Lubbad, R., Høyland, K. and Løset, S. 2014. *Physical model and theoretical model study of level ice and wide sloping structure interactions.* Cold regions science and technology, vol. 101, pp. 40-72. ISSN 0165-232X. doi 10.1016/j.coldregions.2014.01.007.

Määttänen, M., Marjavaara, M. and Saarinen, S. 2011. *Ice crushing pressure distribution against a compliant stiffened panel.* Proceedings of the 21st International Conference on Port and Ocean Engineering under Arctic Conditions, POAC 11, vol. 1. p. 11. Montréal, Canada. ISSN 2077-7841 [Electronic publication].

Määttänen, M., Løset, S., Metrikine, A., Evers, K.-U., Hendrikse, H., Lønøy, C., Metrikin, I., Nord, T. and Sukhorukov, S. 2012. *Novel Ice Induced Vibration Testing in a Large-scale Facility: Deciphering Ice Induced Vibrations, Part 1.* Proceedings of the 21st International Symposium on Ice, IAHR 12, pp. 946-958. Dalian, China [Electronic publication].

Malvern, L. 1969. *Introduction to the Mechanics of a Continuous Medium.* Englewood Cliffs, NJ, USA: Prentice-Hall, p. 713. ISBN 0-13-487603-2.

Marshall, A., Frederking, R., Sayed, M., Nadreau, J., Croasdale, K. and Jordaan, I. 1989. *Measurements of load transmission through grounded ice rubble.* Proceedings of the 10th International Conference on Port and Ocean Engineering under Arctic Conditions, POAC 89, vol. 1, pp. 575-585. Luleå, Sweden. ISSN 0376-6756.

Marshall, A., Jordaan, I. and McKenna, R. 1991. *A two dimensional model of grounded ice rubble.* Proceedings of the 11th International Conference on Port and Ocean Engineering under Arctic Conditions, POAC 91, vol. 1, pp. 428-444. St. John's, Canada. ISSN 0376-6756.

Morris, J., Rubin, M., Block, G. and Bonner, M. 2006. *Simulations of fracture and fragmentation of geologic materials using combined FEM/DEM analysis*. International Journal of Impact Engineering, vol. 33(1-12), pp. 463-473. ISSN 0734-743X. doi 10.1016/j.ijimpeng.2006.09.006.

Munjiza, A. and Andrews K. 1998. *NBS contact detection algorithm for bodies of similar size*. International Journal for Numerical Methods in Engineering, vol. 43(1), pp. 131-149. ISSN 1097-0207. doi 10.1002/(SICI)1097-0207(19980915)43:1<131::AID-NME447>3.0.CO;2-S.

Munjiza, A. 2004. *The Combined Finite-Discrete Element Method*. Chichester, UK: John Wiley & Sons Ltd, p. 352. ISBN 0-470-84199-0.

Nevel, D. 1992. *Ice forces on cones from floes*. Proceedings of the 11th International Symposium on Ice, IAHR 92, vol. 3, pp. 1391-1404. Banff, Canada.

Oñate, E. and Rojek, J. 2004. *Combination of discrete element and finite element methods for dynamic analysis of geomechanics problems*. Computer Methods in Applied Mechanics and Engineering, vol. 193(27-29), pp. 3087-3128. ISSN 0045-7825. doi 10.1016/j.cma.2003.12.056.

Owen, D., Feng, Y., de Souza Neto, E., Cottrell, M., Wang, F., Andrade Pires, F. and Yu, J. 2004. *The modelling of multi-fracturing solids and particulate media*. International Journal for Numerical Methods in Engineering, vol. 60(1), pp. 317-339. ISSN 1097-0207. doi 10.1002/nme.964.

Paavilainen, J., Tuhkuri, J. and Polojärvi, A. 2009. *2D combined finite-discrete element method to model multi-fracture of beam structures*. Engineering Computations, vol. 26(6), pp. 578-598. ISSN 0264-4401. doi 10.1108/02644400910975397.

Paavilainen, J., Tuhkuri, J. and Polojärvi, A. 2010.*Rubble pile formation against an inclined structure – analysis of simulation results*. Proceedings of the 20th International Symposium on Ice, IAHR 10, p. 11. Lahti, Finland [Electronic publication].

Paavilainen, J., Tuhkuri, J. and Polojärvi, A. 2011. *2D numerical simulations of ice rubble formation process against an inclined structure*. Cold regions science and technology, vol. 68(1-2), pp. 20-34. ISSN 0165-232X. doi 10.1016/j.coldregions.2011.05.003.

Paavilainen, J. and Tuhkuri, J. 2012. *Parameter effects on simulated ice rubbling forces on a wide sloping structure*. Cold regions science and technology, vol. 81, pp. 1-10. ISSN 0165-232X. doi 10.1016/j.coldregions.2012.04.005.

Paavilainen, J. 2013. *Factors affecting ice loads during the rubbling process using a 2D FE-DE approach*. Aalto University publication series, Doctoral Dissertations 31/2013. Helsinki, Finland: Unigrafia Oy: p. 144. ISBN 978-952-60-5031-7. ISSN 1799-4934.

Paavilainen, J. and Tuhkuri, J. 2013. *Pressure distributions and force chains during simulated ice rubbling against sloped structures*. Cold regions science and technology, vol. 85, pp. 157-174. ISSN 0165-232X. doi 10.1016/j.coldregions.2012.09.005.

Palmer, A. and Croasdale, K. 2012. *Arctic Offshore Engineering*. Singapore: World Scientific, p. 357. ISBN 978-981-4368-77-3.

Palmer, A. and Dempsey, J. 2009. *Model tests in ice*. Proceedings of the 20th International Conference on Port and Ocean Engineering under Arctic Conditions, POAC 09, vol. 1, p. 10. Luleå, Sweden. ISSN 2077-7841 [Electronic publication].

Peters, J., Muthuswamy, M., Wibowo, J. and Tordesillas, A. 2005. *Characterization of force chains in granular material*. Physical review E: Statistical, nonlinear, and soft matter physics, vol. 72(4), 041307, p. 8. ISSN 1550-2376. doi 10.1103/PhysRevE.72.041307.

Polojärvi, A. and Tuhkuri, J. 2009. *3D discrete numerical modelling of ridge keel punch through tests*. Cold Regions Science and Technology, vol. 56(1), pp. 18-29. ISSN 0165-232X. doi 10.1016/j.coldregions.2008.09.008.

Polojärvi, A. and Tuhkuri, J. 2013. *On modeling cohesive ridge keel punch through tests with a combined finite-discrete element method*. Cold Regions Science and Technology, vol. 85, pp. 191-205. ISSN 0165-232X. doi 10.1016/j.coldregions.2012.09.013.

Polojärvi, A., Tuhkuri, J. and Pustogvar, A. 2015. *DEM simulations of direct shear box experiments of ice rubble: Force chains and peak loads*. Cold Regions Science and Technology, vol. 116, pp. 12-23. ISSN 0165-232X. doi 10.1016/j.coldregions.2015.03.011.

Ralston, T. 1977. *Ice force design considerations for conical offshore structures*. Proceedings of the 4th International Conference on Port and Ocean Engineering under Arctic Conditions, POAC 77, vol. 2, pp. 741-751. St. John's, Canada. ISBN 0-920568-01-7.

Ranta, J., Santaoja, K. and Tuhkuri, J. 2010. *Simulation of Ice Rubble Failure against a Conical Structure with Arbitrary Lagrangian-Eulerian Finite Element Method*. Proceedings of the 20th International Symposium on Ice, IAHR 10, p. 12. Lahti, Finland [Electronic publication].

Ranta, J., Tuhkuri, J. Polojärvi, A. and Paavilainen, J. 2014. *Statistical reconstruction of peak ice load data based on 2D combined finite-discrete element method simulations of ice interactions against inclined wall*. Proceedings of the 22nd International Symposium on Ice, IAHR 14, p. 18. Singapore. ISBN 978-981-09-0750-1 [Electronic publication].

Reddy, J. 2004. *An Introduction to Nonlinear Finite Element Analysis*. New York, NY, USA: Oxford University Press, p. 463. ISBN 0-19-852529-X.

Saarinen, S. 2000. *Description of the pile-up process of an ice sheet against an inclined plate*. Master's thesis. Helsinki University of technology, Department of Mechanical Engineering. p. 78. (In Finnish).

Sanderson, T. J. O. 1988. *Ice Mechanics, Risks to Offshore Structures*. London, UK: Graham &Trotman Limited, p. 253. ISBN 0-86010-785-X.

Sayed, M. 1989. *Transmission of loads through grounded ice rubble*. 4th IAHR State-of-the-Art Report on Ice Forces on Structures, CRREL Special Report 89-5, pp. 259-275. U.S. Army CRREL, Hanover, NH, USA.

Schreyer, H., Sulsky, D., Munday, L., Coon, N. and Kwok, R. 2006. *Elastic-decohesive constitutive model for sea ice*. Journal of Geophysical Research, vol. 111(C11). ISSN 2156-2202. doi 10.1029/2005JC003334.

Schwarz, J. 1977. *New developments in modeling ice problems*. Proceedings of the 4th International Conference on Port and Ocean Engineering under Arctic Conditions, POAC 77, vol. 1, pp. 45-61. St. John's, Newfoundland, Canada. ISBN 0-920568-00-9.

Serré, N. 2011. *Numerical modelling of ice ridge keel action on subsea structures*. Cold Regions Science and Technology, vol 67(3), pp. 107-119. ISSN 0165-232X. doi 10.1016/j.coldregions.2011.02.011.

Sodhi, D. 2011. *Crushing failure during ice-structure interaction*. Engineering Fracture Mechanics, vol. 68(17-18), pp. 1889-1921. ISSN 0013-7944. doi 10.1016/S0013-7944(01)00038-8.

Sudom, D. and Timco, G. 2009. *Load reduction due to grounded ice rubble on the Molikpaq*. Proceedings of the 20th International Conference on Port and Ocean Engineering under Arctic Conditions, POAC 09, vol. 1, pp. 378-387. Luleå, Sweden. ISSN 2077-7841.

Timco, G. 1984. *Model tests of ice forces on a wide inclined structure*. Proceedings of the 7th International Symposium on Ice, IAHR 84, vol. 2, pp 87-96. Hamburg, Germany.

Timco, G. 1984. *Ice Forces on Structures: Physical Modelling Techniques*. 2nd IAHR State-of-the-Art Report on Ice Forces on Structures, vol. 4, pp. 117-150. Hamburg, Germany.

Timco, G., Sayed, M. and Frederking, R. 1989. *Model tests of load transmission through grounded ice rubble*. Proceedings Eighth International Conference on Offshore Mechanics and Arctic Engineering, vol IV, pp. 269-274. The Hague, The Netherlands.

Timco, G. and Wright, B. 1999. *Load attenuation through grounded ice rubble at Tarsiut Island*. Proceedings of the 15th International Conference on Port and Ocean

Engineering under Arctic Conditions, POAC 99, vol. 1, pp. 454-463. Helsinki, Finland. ISSN 2077-7841.

Timco, G. and Johnston, M. 2004. *Ice loads on the caisson structures in the Canadian Beaufort Sea*. Cold Regions Science and Technology, vol 38(2-3), pp. 185-209. ISSN 0165-232X. doi 10.1016/j.coldregions.2003.10.007.

Timco, G. and Wright, B. 2005. *Multi-Year Ice Loads on the Molikpaq: May 12, 1986 Event*. Proceedings of the 18th International Conference on Port and Ocean Engineering under Arctic Conditions, POAC 05, vol. 1, pp. 453-462. Potsdam, NY, USA. ISSN 2077-7841.

Timco, G. and Weeks, W. 2009. *A review of the engineering properties of sea ice*. Cold Regions Science and Technology, vol. 60(2), pp. 107-129. ISSN 0165-232X. doi 10.1016/j.coldregions.2009.10.003.

Weeks, W. 2010. *On sea ice* Fairbanks, AK, USA: University of Alaska Press, p. 664. ISBN 978-1-60223-079-8.

Zhou, L., Riska, K., von Bock und Polach, R., Moan, T. and Biao, S. 2013. *Experiments on level ice loading on an icebreaking tanker with different ice drift angles*. Cold Regions Science and Technology, vol. 85, pp. 79-93. ISSN 0165-232X. doi 10.1016/j.coldregions.2012.08.006.